

An Enhanced Latent Heat Thermal
Storage System Using
Electrohydrodynamics (EHD)

An Enhanced Latent Heat Thermal Storage System Using Electrohydrodynamics (EHD)

By
David Nakhla, B.Sc.

A THESIS
Submitted to the School of Graduate Studies
in Partial Fulfillment of the Requirements
for the Degree
Master of Applied Science
McMaster University
© Copyright by David Nakhla, October 2013, all rights reserved.

PERMISSION TO USE

In presenting this thesis in partial fulfillment of the requirements for a Postgraduate degree from McMaster University, I agree that the Libraries of this University may make it freely available for inspection. I further agree that the permission for copying this thesis in any manner, in whole or in part for scholarly purposes, may be granted by the professors who supervised my thesis work or, in their absence, by the Head of the Department or the Faculty Dean in which my thesis work was conducted. It is understood that any copying or publication or use of this thesis or parts thereof for financial gain shall not be allowed without my written permission. It is also understood that due recognition shall be given to me and McMaster University in any scholarly use which may be made of any material in my thesis. Requests for permission to copy or to make other use of material in this thesis, in whole or part, should be addressed to:

Head of the Department of Mechanical Engineering
McMaster University
Faculty of Engineering
1280 Main Street West
Hamilton, Ontario L8S 4L6
Canada

MASTER OF APPLIED SCIENCE (2013)
(Department of Mechanical Engineering)

McMaster University
Hamilton, Ontario, Canada

TITLE: An Enhanced Latent Heat Thermal Storage System
Using Electrohydrodynamics (EHD)

AUTHOR: David Nakhla, B.Sc

SUPERVISOR: Dr. J.S.Cotton

NUMBER OF PAGES: 168,xx

“To my parents and my brother “

ABSTRACT

Electrohydrodynamics (EHD) was used to enhance the thermal performance of a latent heat thermal storage cell by reducing the charging time for a given amount of latent heat stored. Paraffin wax, which is an organic dielectric commercially available material was selected as the phase change material (PCM).

Electric field was applied into the cell by using 9 electrodes kept at -8 kV in an effort to establish EHD forces inside the PCM. The EHD effect was studied in an originally conduction dominated melting environment. That was achieved by the cell design which promoted unidirectional melting downwards to prevent natural convection from occurring by assuring a thermally stratified molten phase. The target was to study the EHD mechanisms of enhancement with less interfering physics.

Melting was studied under constant heat flux boundary condition. The temporal thermal profile of the surface heater and the melt front location were used to assess the EHD effect by comparing it to a 0 kV (no EHD) case.

It was found that by using EHD (-8 kV), the time required to melt 7 mm thickness of the PCM can be reduced by 40 % when compared to 0 kV case. Through a four hour experiment time, the amount of molten PCM can be increased by 29 % by using EHD compared to 0 kV. The EHD power consumption was less than 0.17 W which is equivalent to 2.4 % of the thermal energy stored in the PCM.

A new phenomena was discovered when applying EHD in the tested cell, which is Solid Extraction, where the solid dendrites within the mushy zone were extracted from the mushy zone into the liquid bulk towards regions of higher electric field.

A new criteria was developed to quantify the EHD enhancement level and was called EHD enhancement factor. An enhancement factor up to 13 could be reached by using EHD. The effect of changing the heat flux on the enhancement factor was investigated, and it was found that the enhancement factor decreased by increasing the heat flux.

Numerical simulations were performed in an effort to understand the EHD mechanisms of enhancement. The static electric field distribution, the interfacial extraction forces and the body forces acting on suspended dendrites were evaluated. The results of numerical simulations were supported by the high speed imaging and the experimental data to explain the EHD mechanisms of enhancement and the regions where solid dendrites extraction happened.

Finally an analytical model was developed to estimate the energy stored in the different components of the tested latent heat storage cell and to estimate the amount of energy lost to the surroundings in order to quantify the accuracy of the experiment and a maximum of 18 % heat loss was estimated.

ACKNOWLEDGMENT

First, I would like to express my sincere gratitude to my supervisor Dr. Cotton for his support, guidance, and motivation through the past two years. It was an honor working with you.

I would like to thank Dr. Ching for his unique ability for motivation and for his valuable advices. I would like to thank Dr.Hossam Sadek for his help through the project.

I would like to extend my thanks to the mechanical engineering technicians; Ron Lodewyks, Joe Verhaeghe, J.P. Talon, Mark MacKenzie, Jim McLaren and Michael Lee and to the mechanical engineering staff; Vania Loyzer, Lily Sazz-Fayter and Florence Rosato for their help.

I would like to thank all my friends at McMaster University and TMRL group, it was a pleasure meeting you all.

Finally I would like to thank my parents, thanks for everything. Thanks for your support and encouragement throughout the past two years. Thanks for my best friend and Brother Daniel. Thanks MarMora for being in my life now.

TABLE OF CONTENTS

PERMISSION TO USE	III
TABLE OF CONTENTS	IX
LIST OF FIGURES.....	XI
1. INTRODUCTION	3
1.1. THERMAL ENERGY STORAGE	3
1.2. EHD HEAT TRANSFER ENHANCEMENT TECHNIQUE	13
1.3. RESEARCH OBJECTIVE	14
2. LATENT HEAT THERMAL STORAGE (LHTS)	15
2.1. SOLID – LIQUID PHASE CHANGE MATERIALS	16
2.1.1. Organic PCMs	17
2.1.2. Inorganic PCMs.....	18
2.2. HEAT TRANSFER ENHANCEMENT OF LHTS SYSTEMS.....	21
2.2.1. Passive Enhancement Techniques	21
2.2.2. Active enhancement techniques.....	38
3. ELECTROHYDRODYNAMIC (EHD) HEAT TRANSFER ENHANCEMENT.....	44
3.1. INTRODUCTION	44
3.2. GOVERNING EQUATIONS.....	44
3.2.1. EHD Body Forces.....	47
3.3. SINGLE PHASE EHD HEAT TRANSFER ENHANCEMENT.....	50
3.4. MULTIPHASE EHD HEAT TRANSFER ENHANCEMENT	57
3.4.1. EHD Interfacial Forces.....	57
3.4.2. Boiling and Condensation under EHD forces.....	58
3.4.3. Melting and Solidification under EHD forces	60
4. EXPERIMENTAL FACILITY	68
4.1. TEST FACILITY	68
4.2. EXPERIMENTAL PROCEDURES.....	74
4.2.1. Preparation.....	75
4.2.2. Starting the experiment.....	76
4.2.3. Solidification	77
4.3. EXPERIMENTALLY MEASURED PARAMETERS	78
5. THERMAL CHARACTERIZATION OF STORAGE SYSTEM.....	79
5.1. ENERGY BALANCE ANALYTICAL MODEL	79
5.1.1. Sensible Heat Stored in the Molten PCM	81
5.1.2. Latent Heat Stored in the Molten PCM	83
5.1.3. Energy Stored in Solid PCM and Mushy Zone	83
5.1.4. Sensible Energy Stored in the Acrylic and the Copper Sheet.....	85
5.1.5. Sensible Energy Stored in the Thermal Insulation.....	86
5.1.6. Analytical Model Results	86
5.2. TWO DIMENSIONAL NUMERICAL STORAGE CELL MODEL	89
5.2.1. Validation of the Numerical Model.....	95
5.2.2. Energy Stored in the System.....	95
5.3. PERFORMANCE CHARACTERIZATION AND UNCERTAINTY ANALYSIS.....	105
5.4. SUMMARY.....	108
6. EXPERIMENTAL RESULTS AND NUMERICAL METHODOLOGY	109
6.1. DC ELECTROHYDRODYNAMIC EXPERIMENTAL RESULTS	109
6.2. SOLID EXTRACTION PHENOMENA	118

6.3.	HEAT FLUX EFFECT AND EHD ENHANCEMENT FACTOR.....	124
6.4.	NUMERICAL METHODOLOGY	130
6.4.1.	Electric Field Distribution	133
6.4.2.	Interfacial and Particle Attraction Forces Evaluation	135
7.	CONCLUSIONS AND RECOMMENDATIONS	152
7.1.	CONCLUSIONS	152
7.2.	RECOMMENDATIONS FOR FUTURE WORK	156
	APPENDIX A	158
	APPENDIX B	159
	APPENDIX C	160
•	UNCERTAINTY IN TEMPERATURE MEASUREMENTS USING THERMOCOUPLES	160
•	UNCERTAINTY IN VOLTAGE AND CURRENT MEASUREMENT FOR ELECTRIC HEATER	161
•	UNCERTAINTY IN MELT THICKNESS MEASUREMENT δS	161
•	UNCERTAINTY IN CALCULATED PARAMETERS	162
•	Uncertainty in electric heater power input.....	162
	BIBLIOGRAPHY	163
	163

LIST OF FIGURES

FIGURE 1.1 SCHEMATIC DIAGRAM FOR THERMAL STORAGE APPLICATION IN SOLAR ENERGY.....	5
FIGURE 1.2 SCHEMATIC DIAGRAM FOR THERMAL STORAGE APPLICATION IN WASTE HEAT RECOVERY.....	5
FIGURE 1.3 SCHEMATIC DIAGRAM FOR THERMAL STORAGE APPLICATION IN PEAKING POWER PLANTS.....	7
FIGURE 2.1 CLASSIFICATION OF THERMAL STORAGE MATERIALS. (ZALBA ET AL, 2003)	16
FIGURE 2.2 PHYSICAL PROPERTIES OF SOME PARAFFINS (ABHAT 1983)	17
FIGURE 2.3 COOLING CURVES FOR DIFFERENT PCM, (A) COMMERCIAL PARAFFINS, (B) FATTY ACIDS AND (C) INORGANIC SALT HYDRATES. (ABHAT 1983)	19
FIGURE 2.4 COMPARISON OF ORGANIC AND INORGANIC PCM FOR HEAT STORAGE SYSTEMS. (ZALBA ET AL., 2003) ..	19
FIGURE 2.5 SCHEMATIC REPRESENTATION FOR THE PCM GEOMETRY. (LACROIX AND BENMADDA 1997).....	23
FIGURE 2.6 MELT VOLUME FRACTION VARIATION WITH TIME. (LACROIX AND BENMADDA 1997)	23
FIGURE 2.7 FIN EFFECTIVENESS AT MELTING WITH DIMENSIONLESS TIME. (STRITIH 2004)	25
FIGURE 2.8 MELT FRACTION VS. (A) FO.STE (B) FO.STE/ (RA ^{0.25}) (SHATIKIAN, ET AL., 2005)	26
FIGURE 2.9 THERMAL CONDUCTIVITY OF PARAFFIN/xGNP COMPOSITE. (KIM AND DRZAL 2009)	30
FIGURE 2.10 LATENT HEAT STORAGE OF PARAFFIN/xGNP COMPOSITE WITH THE LOADING CONTENT. (KIM AND DRZAL 2009)	30
FIGURE 2.11 (A) CARBON FIBER CLOTH (B) CARBON FIBER BRUSH (C) NO CARBON FIBER. (NAKASO ET AL. 2008) .	32
FIGURE 2.12 SURFACE DEGREE OF SUPERHEAT VARIATION WITH TIME FOR EG/PCM AND METAL FOAM/PCM COMPOSITE SUBJECTED TO CONSTANT HEAT FLUX. (ZHOU AND ZHAO 2011).....	34
FIGURE 2.13 STORED HEAT FOR SENSIBLE AND LATENT STORAGE SYSTEMS USING SINGLE AND CASCADED PCMS. (MEHLING AND CABEZA, 2008)	36
FIGURE 2.14 HEATER SURFACE TEMPERATURE VARIATION WITH TIME. (OH ET AL. 2002).....	40
FIGURE 2.15 TEMPERATURE HISTORY AGAINST NORMALIZED TIME. (OH ET AL. 2002)	40
FIGURE 3.1 SCHEMATIC EHD FORCES AND ELECTRIC FIELD LINES. (A)ELECTROPHORETIC FORCE (B) DIELECTROPHORETIC (POLARIZATION) IN SINGLE PHASE (C) EHD FORCES ON INTERFACE (D) EHD FORCES ACTING ON A SUSPENDED DROPLET OR BUBBLE. (BRYAN, ET AL., 2001)	49
FIGURE 3.2 (A) STREAK FLOW VISUALIZATION. (B) SCHEMATIC REPRESENTATION FOR THE LEAF PATTERN INDUCED BY ELECTROCONVECTION IN AN ANNULAR CROSS SECTION. (FERNÁNDEZ, ET AL., 1987)	51
FIGURE 3.3 (I) SHADOWGRAPH IMAGES WITH TIME INTERVAL 0.2 SEC. (II) SCHEMATIC ILLUSTRATION OF ELECTRICALLY INDUCED SECONDARY FLOW. (FUJINO, ET AL., 1989)	51
FIGURE 3.4 AVERAGE HEAT TRANSFER COEFFICIENT VS. HEAT FLUX AT THE SURFACE OF THE HEATING ELECTRODE. (FUJINO, ET AL., 1989).....	52
FIGURE 3.5 COMPARISON BETWEEN NUMERICAL AND EXPERIMENTAL HEAT ENHANCEMENT FOR V=7.5 TO 17.5 kV AND 5 ELECTRODES UNDER DIFFERENT RAYLEIGH NUMBERS. (KASAYAPANAND, 2008)	55
FIGURE 3.6 HEAT TRANSFER ENHANCEMENT WITH THE NUMBER OF ELECTRODES. (KASAYAPANAND, 2008).....	55
FIGURE 3.7 ELECTRICAL POWER VS. NUSSELT NUMBER. (PASCHKEWITZ, ET AL., 2000)	56
FIGURE 3.8 (A) VELOCITY VECTOR FIELD. (B) ISOTHERMS (C) NORMAL TEMPERATURE GRADIENTS AT THE TOP AND BOTTOM WALL/ 0kV AND FULL GRAVITY CASE. (DULIKRAVICH, ET AL., 1994)	62
FIGURE 3.9 CROSS SECTIONAL VIEW OF THE THERMAL STORAGE CELL AND A DETAILED SECTION VIEW FOR INTERNAL FIN DIMENSIONS. (DELLORUSSO, 1997)	64

FIGURE 3.10 ELECTRICAL CONFIGURATIONS FOR EHD ENHANCEMENT. (DELLORUSSO, 1997).....	65
FIGURE 3.11 NORMALIZED AVERAGE HEAT TRANSFER COEFFICIENT FOR SOLIDIFICATION CYCLES UNDER DIFFERENT REYNOLDS NUMBER OF THE AIR SIDE. (DELLORUSSO, 1997)	65
FIGURE 3.12 AVERAGE HEAT ABSORPTION RATE FOR MELTING CYCLES UNDER DIFFERENT REYNOLD'S NUMBER OF THE AIR SIDE. (DELLORUSSO, 1997).....	67
FIGURE 4.1 SCHEMATIC OF EXPERIMENTAL TEST FACILITY	69
FIGURE 4.2 FRONT VIEW FOR THE EXPERIMENTAL TEST SECTION.....	70
FIGURE 4.3 TOP VIEW FOR THE EXPERIMENTAL TEST SECTION.....	70
FIGURE 4.4 THERMOCOUPLE LOCATIONS ON THE COPPER SHEET.....	71
FIGURE 4.5 DETAILS OF ELECTRODES CONFIGURATION	73
FIGURE 4.6 MELT FRONT LOCATION IMAGES	74
FIGURE 5.1 SCHEMATIC OF ENERGY BALANCE MODEL	82
FIGURE 5.2 SCHEMATIC FOR THE TEMPERATURE DISTRIBUTIONS INSIDE THE PCM	85
FIGURE 5.3 ANALYTICAL MODEL ENERGY BALANCE RESULTS.....	88
FIGURE 5.4 SCHEMATIC OF THE TWO DIMENSIONAL CFD MODEL.....	90
FIGURE 5.5 CFD GRID INDEPENDENCE STUDY RESULT- 14.2 W AND 0 kV CASE.....	93
FIGURE 5.6 CFD TIME STEP INDEPENDENCE STUDY RESULT-14.2 W AND 0 kV CASE	93
FIGURE 5.7 LONGITUDINAL TEMPERATURE DISTRIBUTION FOR THE NUMERICAL AND ANALYTICAL MODEL.....	94
FIGURE 5.8 MELT FRONT LOCATION (MEASURED FROM THE HEATING SURFACE) AGAINST TIME FOR Q = 14.2 WATTS	96
FIGURE 5.9 HEATING SURFACE AVERAGE TEMPERATURE VARIATION WITH TIME FOR Q=14.2 WATTS.....	96
FIGURE 5.10 CFD STORED ENERGY ANALYSIS WITH TIME	98
FIGURE 5.11 CFD HEAT LOSS ANALYSIS WITH TIME (14.2 WATTS-0 kV)	100
FIGURE 5.12 CFD HEAT LOSS ANALYSIS AGAINST COPPER AVERAGE SURFACE TEMPERATURE (14.2 WATTS)	102
FIGURE 5.13 CFD HEAL LOSS ANALYSIS WITH TIME (14.2WATTS-NEG 8kV CASE)	102
FIGURE 5.14 CFD HEAT LOSS ANALYSIS WITH TIME FOR 10.3 WATTS (A- 0 kV, B- NEG 8 kV)	103
FIGURE 5.15 CFD HEAT LOSS ANALYSIS WITH TIME FOR 7.1 WATTS (A- 0 kV, B-NEG 8 kV)	104
FIGURE 6.1 A SCHEMATIC DIAGRAM FOR THE THERMAL CIRCUIT.	111
FIGURE 6.2 HEATING SURFACE AVERAGE TEMPERATURE VARIATION WITH TIME FOR Q = 7.1 W, WITH AND WITHOUT AN APPLIED VOLTAGE (-8 kV)	113
FIGURE 6.3 MELT FRONT LOCATION (MEASURED FROM THE HEATING SURFACE) WITH TIME FOR Q = 7.1 W, WITH AND WITHOUT APPLIED VOLTAGE (-8 kV).....	113
FIGURE 6.4 HEATING SURFACE AVERAGE TEMPERATURE VARIATION WITH TIME FOR Q = 10.4 W, WITH AND WITHOUT AN APPLIED VOLTAGE (-8 kV)	115
FIGURE 6.5 MELT FRONT LOCATION (MEASURED FROM THE HEATING SURFACE) WITH TIME FOR Q = 10.4 W, WITH AND WITHOUT AN APPLIED VOLTAGE (-8 kV).....	115
FIGURE 6.6 HEATING SURFACE AVERAGE TEMPERATURE VARIATION WITH TIME FOR Q = 14.2 W, WITH AND WITHOUT AN APPLIED VOLTAGE (-8 kV)	116
FIGURE 6.7 MELT FRONT LOCATION (MEASURED FROM THE HEATING SURFACE) WITH TIME FOR Q = 14.2 W. WITH AND WITHOUT AN APPLIED VOLTAGE (-8 kV).....	116
FIGURE 6.8 SCHEMATIC DIAGRAM FOR HIGH SPEED IMAGING MATRIX	119
FIGURE 6.9 SOLID - LIQUID INTERFACE BEHAVIOUR UNDER AN APPLIED VOLTAGE OF (-8 kV) AT LOCATION (A1)-TIME BETWEEN FRAMES 0.4 SEC.....	121
FIGURE 6.10 SOLID - LIQUID INTERFACE BEHAVIOUR UNDER AN APPLIED VOLTAGE OF (-8 kV) AT LOCATION (B2)- TIME BETWEEN FRAMES 0.08 SEC	123

FIGURE 6.11 CURVE FITTING FOR MELT FRONT LOCATION (MEASURED FROM THE HEATING SURFACE) WITH TIME FOR Q = 7.1 W.....	126
FIGURE 6.12 MELT FRONT VELOCITY AT A GIVEN MELT THICKNESS FOR Q=7.1 W.....	126
FIGURE 6.13 EHD ENHANCEMENT FACTOR (EF) AT A GIVEN MELT THICKNESS FOR Q=7.1 W	126
FIGURE 6.14 CURVE FITTING FOR MELT FRONT LOCATION (MEASURED FROM THE HEATING SURFACE) WITH TIME FOR Q = 10.4 W	127
FIGURE 6.15 MELT FRONT VELOCITY AT A GIVEN MELT THICKNESS FOR Q=10.4 W	127
FIGURE 6.16 EHD ENHANCEMENT FACTOR (EF) AT A GIVEN MELT THICKNESS FOR Q=10.4 W	127
FIGURE 6.17 CURVE FITTING FOR MELT FRONT LOCATION (MEASURED FROM THE HEATING SURFACE) WITH TIME FOR Q = 14.2 W	128
FIGURE 6.18 MELT FRONT VELOCITY AT A GIVEN MELT THICKNESS FOR Q=14.2 W	128
FIGURE 6.19 EHD ENHANCEMENT FACTOR (EF) AT A GIVEN MELT THICKNESS FOR Q=14.2 W	128
FIGURE 6.20 VARIATION OF EF WITH MELT THICKNESS FOR DIFFERENT HEAT INPUT VALUES.....	130
FIGURE 6.21 ELECTRODE GEOMETRY AND THE SOLID AND LIQUID DOMAIN FOR THE NUMERICAL SIMULATION	132
FIGURE 6.22 TWO DIMENSIONAL ELECTRIC FIELD DISTRIBUTION AT (A) S=4 MM AND (B) S=7 MM (C) S=9.5 MM (D) S=12 MM (E) S=14 MM	134
FIGURE 6.23 SECTION OF A TRANSITION LAYER SEPARATING TWO DIELECTRIC MEDIA, (STRATTON, 1941).....	137
FIGURE 6.24 EXTRACTION FORCE DISTRIBUTION ACROSS THE SOLID -LIQUID INTERFACE FROM X=40 TO X=60 MM AT DIFFERENT LEVELS MEASURED FROM THE HEATER (S=2 MM TO S=6 MM)	138
FIGURE 6.25 EXTRACTION FORCE DISTRIBUTION ACROSS THE SOLID -LIQUID INTERFACE FROM X=40 TO X=60 MM AT DIFFERENT LEVELS MEASURED FROM THE HEATER (S=7 MM TO S=14 MM)	138
FIGURE 6.26 SUMMARY OF EXTRACTION FORCES PER UNIT AREA AT DIFFERENT MELT FRONT LOCATIONS FOR TWO AXIAL LOCATIONS, X=40 MM (CENTRE LINE OF UPPER ELECTRODE) AND X=50 MM (CENTRE LINE OF LOWER ELECTRODE).....	140
FIGURE 6.27 TWO DIMENSIONAL NUMERICAL REPRESENTATION OF ∇E^2 VECTOR FIELD AT (A) S=4 MM (B) S=7 MM (C) S=10 MM (D) S=12 MM (E) S=14 MM	146
FIGURE 6.28 PARTICLE ATTRACTION FORCE DISTRIBUTION ACROSS THE SOLID -LIQUID INTERFACE FROM X=40 TO X=60 MM AT DIFFERENT MELT FRONT LOCATIONS. (S=2 MM TO S=7MM).....	149
FIGURE 6.29 PARTICLE ATTRACTION FORCE DISTRIBUTION ACROSS THE SOLID -LIQUID INTERFACE FROM X=40 TO X=60 MM AT DIFFERENT MELT FRONT LOCATIONS (S=7 MM TO S=14MM)	149
FIGURE 6.30 SUMMARY FOR THE INTERFACIAL AND PARTICLE ATTRACTION FORCES (DEP) AT DIFFERENT MELT FRONT LOCATIONS.....	150

NOMENCLATURE

Symbols		Subscripts	
A	Area [m^2]	l	Liquid Phase
Cp	Heat Capacity [J/kgK]	s	Solid Phase
d	Derivative (i.e. dx/dt)	mushy	Mushy zone
D	Diameter [m]	b	bottom
\bar{E}	Electric field strength [V/m]	R	Riser
i	Electric current [A]	heater	Electric heater
q	Heat Flux Density [W/m^2]	I/P	Input
h	Heat Transfer Coefficient [W/m^2K]	i	Initial
ΔH_f	Latent Heat of Fusion [J/kg]	s	Heating surface
Nu	Nusselt number	f	final
Re	Reynolds number	m	Melt
Ra	Rayleigh number	PCM	Phase Change Material
[J]	Joules	R	Recovery
k	Thermal Conductivity, [W/mK]	SC	Sub cooling
[K]	Kelvin	SH	Superheat
[kg]	Kilograms	sl	Solid/Liquid
L	Length [m]		
m	Mass [kg]		
\dot{m}	Mass Flow Rate [kg/s]		
[m]	Meters		
Q	Power [W]		
q''	Heat Flux Density [W/m^2]		
S(t)	Position of the Solid-Liquid Interface [m]		
[s]	Seconds		
t	Times [s]		
T	Temperature [K]		
[W]	Watts [J/s]		
x	Position [m]		
α	Thermal Diffusivity [m^2/sK]		
δ	Partial Derivative (i.e. $\delta x / \delta t$)		
κ	Thermal Diffusivity [m^2/sK]		
μ	Kinematic Viscosity [kg/ms]		
Π	Pi (3.14159...)		
ρ	Density [kg/m^3]		
ν	Dynamic Viscosity [m^2/s]		
Fo	Fourier number		
Ste	Stefan number		
U	Velocity [m/s]		
V	Voltage [V]		
\bar{j}	Electric current density [A/m^2]		

ε	Dielectric constant
ρ_e	Free charge density [C/m^3]
EF	Enhancement factor
t	Extraction force [N/m^2]
δ	Mushy zone thickness[mm]

1. Introduction

1.1. Thermal Energy Storage

Thermal energy storage is a technology which allows storing excess thermal energy in thermal energy reservoirs for being collected later when needed. Thermal energy storage technologies have been studied extensively in the last two decades due to its economic and environmental promises in the future. The use of thermal storage technologies have been associated with solar energy applications, waste heat recovery systems, peak shaving strategies and peaking power plants.

Thermal energy storage technologies have been used in solar energy applications. Solar energy is one of the energy renewable sources which is always varying whether from day to night and/or due to seasonal climate changes. Due to this uncontrollable variation and intermittency in the energy supply, the instantaneous consumer thermal demand can be hardly met with the instantaneous energy supply. An example for the mismatch between the consumer demand and energy supply, is the lack of energy supply during night time in solar energy applications.

The advantage of using thermal energy storage in solar energy applications is to store thermal energy during off-peak demand periods (energy supplied more than energy needed) for being used later during night time or peak periods (energy supplied less than

energy needed). A schematic diagram for the usage of thermal storage technology in solar energy application is shown in Figure 1.1. The figure is showing a typical consumer thermal demand during day and the corresponding solar energy available. Introducing a thermal storage unit into the system will allow for storing excess energy during noon time for being used later during night time.

Another usage for thermal energy storage is in waste heat recovery applications. Waste heat is the thermal energy outcome from any process inefficiencies which can't be avoided according to the 2nd law of thermodynamics. Recovery of the waste heat with thermal storage technology is collecting this thermal energy and storing it for being used later when needed instead of dumping it. The reason for using thermal storage in waste heat recovery instead of using the waste heat directly is the mismatch between the supply and demand in the energy. A schematic diagram for the capability of using thermal storage in waste heat recovery is presented in Figure 1.2. The figure is showing a constant power input from a waste heat energy source which is used to cover the consumer peak load from thermal demand by recovering the energy needed from the thermal storage system.

Thermal energy storages can be used in peak shaving, an example is reducing the capacity of an absorption chiller. Instead of designing an absorption chiller that is capable of meeting the maximum expected cooling load during the year, its capacity can be reduced when connected to a thermal storage system. The idea is similar to that of the waste energy recovery presented in Figure 1.2. Instead of the supply from the waste

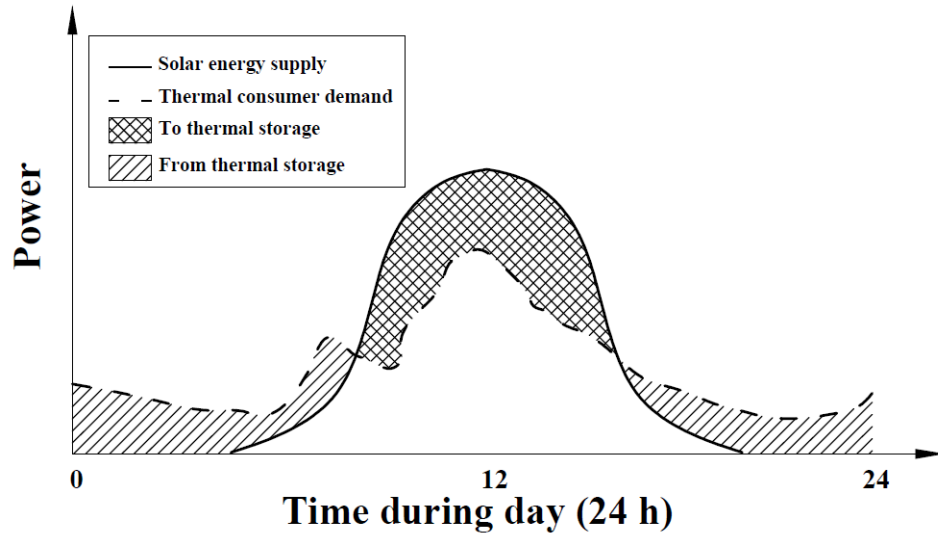


Figure 1.1 Schematic diagram for thermal storage application in solar energy

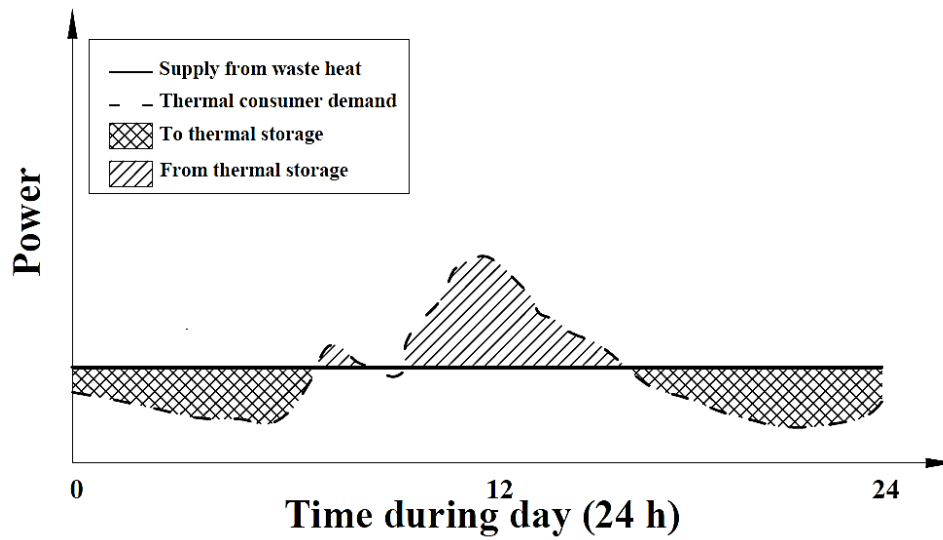


Figure 1.2 Schematic diagram for thermal storage application in waste heat recovery

energy, it is replaced by an absorption chiller operating continuously on a certain base load lower than that of the maximum cooling load. During peak hours both the absorption chiller and the thermal storage will work simultaneously to provide with the needed cooling load. This will decrease the capital cost of the absorption chiller and will allow the chiller to run continuously on its highest efficiency.

Finally, thermal storage systems can be used in combined heat and power plants (CHP). CHP power plants uses the advantage of producing heat and power at the same time to serve one certain location. Electric energy is usually produced using a gas turbine that is connected to electric generator and the exhaust gases are the source for heat. Using the CHP can reduce the fuel consumption by 20 to 30 % while producing the same amount of electricity and heat (Lund, et al., 2005). Usually it is used as a peaking power plant for providing electric generation during peak hours where the market price for electricity is high, at the same time producing excess heat coming from the exhaust gases which can then be stored in thermal storage systems. The gas turbine can be shut down at night where the electric energy needed by the district can be drawn directly from the grid where the market price is low during night times and the heat load required can be recovered from thermal storage cell. A schematic diagram representing the role of thermal storage in peaking power plants is presented in Figure 1.3.

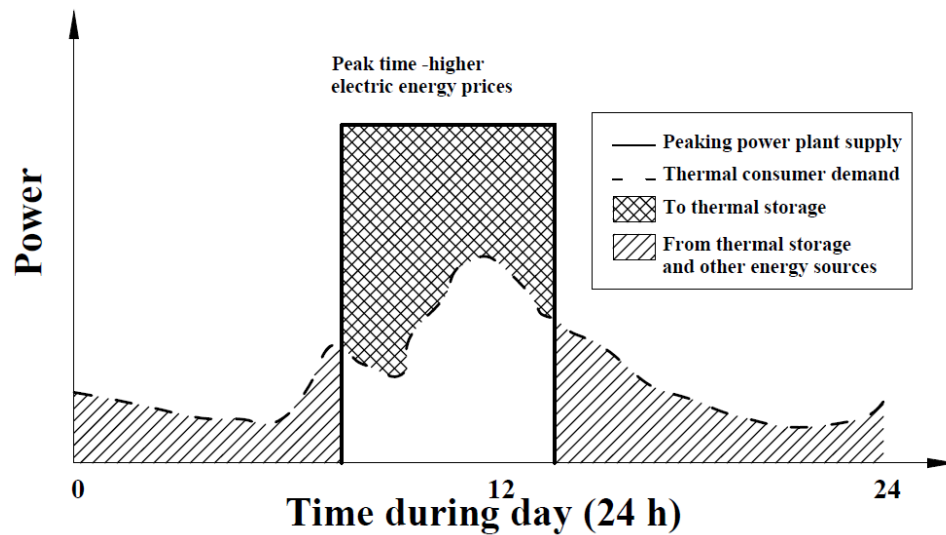


Figure 1.3 Schematic diagram for thermal storage application in peaking power plants.

The overall energy efficiency of the system will be dependent on the performance of the thermal storage system. There are different methods used in storing thermal energy, which can be classified to:

- 1) Sensible heat storage
- 2) Latent heat storage
- 3) Thermochemical heat storage

These methods differ in the heat storage density which is heat stored per unit weight or volume, in which form the heat is stored, the temperature behaviour of the medium during heat storage and the application of the storage technology.

A. Sensible heat storage:

In sensible heat storage systems, the energy is stored in the form of sensible energy by changing the temperature of the storage medium. The amount of heat stored depends on:

the mass of the storage medium, the heat capacity of the medium and the temperature change in the medium during energy storage or energy recovery. The sensible energy storage equation is

$$Q_{sensible} = m_{medium}C_{medium}\Delta T \quad (1.1.)$$

Sensible energy can be stored in solids or liquids, such as stone or bricks and water or oil. Water is the most common used as a medium for sensible storage, where hot water is being used in domestic heating and residential heating applications.

Sensible energy storage offers some advantages:

- Most of the time the storage medium and the working fluid are the same as in the case of domestic and residential heating.
- Storage medium such as water and mineral oil are available, cheap and easy to use and they are chemically stable and easy to use.
- Minor volume variations accompany the thermal storage process.

The main disadvantages of using sensible storage systems:

- Sensible energy storage systems are low storage density systems. For achieving a certain energy storage capacity, sensible storage systems will need more volume than the other two energy storage methods.
- It is less efficient from the thermodynamic point of view because energy is stored in the form of temperature difference. This increases the temperature gap between the working fluid and the thermal storage fluid.

B. Latent heat storage:

In latent heat storage systems, storing energy is by phase change. The phase of transformation energy could be between solid and liquid phase as in melting and solidification or between liquid and vapour as in evaporation and condensation. A part of the energy can also be stored in a sensible energy form too as a sensible energy required to raise the temperature of the medium to the melting or evaporation temperature and/or energy stored in superheating the molten medium or the evaporated medium. The latent energy storage equation is

$$Q_{latent} = m_{medium}\Delta H_f \quad (1.2.)$$

And in case of the existence of preheating and super heating for the phase change medium, the total energy stored equation is

$$Q_{stored} = mC(T_m - T_i) + m\Delta H_f + mC(T_f - T_m) \quad (1.3.)$$

The main advantages of using latent heat storage systems are:

- Latent heat storage systems are characterized by having high thermal storage density, due to the higher values of latent heat of fusion or evaporation when compared to the specific heat capacity of the medium.
- Latent heat storage systems are characterized by a higher efficiency in storing energy, this is because any phase transformation occurs at mostly constant temperature, and this decreases the temperature gap between the working fluid and the thermal storage fluid.

The main disadvantages of using latent heat storage systems are:

- Most phase change materials (PCMs) are characterized by a very low thermal conductivity which slows the heat transfer process during charging and discharging.
- Some PCMs are quite expensive, others are chemically unstable and degrades over time.
- Low specific heat capacities which limits the benefit only at the melting temperature range.

C. **Thermochemical heat storage:**

In thermochemical heat storage systems, the energy storage and recovery process is based on a reversible chemical reaction. This reaction goes as an endothermic reaction during heat storage and as an exothermic reaction during energy recovery.

A reversible chemical reaction can be illustrated as



where (A) is the thermochemical material, this material absorbs energy and then being decomposed chemical into two materials (B) and(C) where each is stored separately. During the energy recovery, materials (B) and (C) are recalled from their reservoirs and combine together releasing an amount of heat and forming back material (A).

The main advantage of using thermochemical heat storage systems is:

- The thermochemical heat storage systems have the highest energy storage density which this will result in a compact system

The main disadvantages of using thermochemical heat storage are:

- Implementation of such systems is complicated and may not be applicable for domestic applications
- The chemical reactions must not have a corrosive effect to the materials of construction and all chemicals must be safe and environmentally friendly
- These systems mainly depend on the chemical reactions and some of these reactions may require high pressure which will lead to a pressurized system.

A comparison between the heat storage densities for each of the three storage methods is reported in Table 1.1. The energy storage density for the sensible storage type was based upon a temperature difference of 20 °C across the thermal storage medium where bigger temperature differences will result in higher storage density but a less energy efficient storage system. From Table 1.1, thermochemical storage systems have the highest storage density and have one of the highest working temperature ranges. Also it is the most complex system to apply. This makes thermochemical systems good solution for high temperature thermal storage used in high temperature power generation such as solar power tower.

Table 1.1 Heat storage energy density comparison between different heat storage methods.
(Mehling, et al., 2008) (Felderhoff, et al., 2013)

	Storage density (kJ/kg)	Temperature
<u>Sensible storage</u>		
Granite	17	$\Delta T=20\text{ }^{\circ}\text{C}$
Water	84	$\Delta T=20\text{ }^{\circ}\text{C}$
<u>Latent heat storage</u>		
Water	330	Melting temperature $0\text{ }^{\circ}\text{C}$
Water	2450	Boiling temperature $100\text{ }^{\circ}\text{C}$
Paraffins	200	Melting temperatures $5\text{-}130\text{ }^{\circ}\text{C}$
<u>Thermochemical heat storage</u>		
H ₂ gas (oxidation)	120000	
$\text{Mg}+\text{H}_2\rightleftharpoons\text{MgH}_2$	2808	Temperature range $350\text{-}450\text{ }^{\circ}\text{C}$
$2\text{Mg}+\text{Fe}+3\text{H}_2\rightleftharpoons\text{Mg}_2\text{FeH}_6$	1980	Temperature range $450\text{-}550\text{ }^{\circ}\text{C}$

In the scope of this project, the main concern is the thermal storage for waste heat recovery applications operating at low temperature ranges (below $120\text{ }^{\circ}\text{C}$) that can be used in domestic and residential heating or automotive industry. At this range, latent heat thermal storage is the best option due to the high storage density which allows for a more compact thermal storage system. In case of residential and automotive application the overall size of the system and the efficiency are very important.

The performance of the latent heat storage system will depend upon the phase change material (PCM) chosen and its thermal and physical properties.

In this range of temperature all the PCMs are characterized by a low thermal conductivity ranging from 0.1 to 0.6 W/mK, this slows down the heat transfer process and limits the system storage capacity for a given charging period. Active and passive heat transfer enhancement techniques used in this field will be discussed in the next chapter. In general passive techniques increases the cost of the storage system and it occupies volume in the system which sometimes reaches 20 % of the system itself. The active heat enhancement techniques previously studied in this field was the use of ultrasonic vibrations, however the power consumption from this technique was very high. EHD is considered one of the least power consumption active techniques, details of EHD will be discussed in next section and chapter 3. In the scope of this project, organic PCM (paraffin wax) was chosen for its dielectric properties which allows for EHD usage and its commercial availability in latent heat thermal storage systems.

1.2. EHD Heat Transfer Enhancement Technique

EHD is the study of dielectric fluid motion induced by the application of high electric fields. EHD is considered one of the least power consumption active heat enhancement techniques. Previous research in single phase flow and multi-phase (liquid-vapor) flows showed that EHD can increase the heat transfer enhancements by several folds. The mechanisms of EHD enhancement are: induced secondary motion, turbulence or phase redistribution. The magnitude of the enhancement can be controlled by the varying the applied voltage into the system. The design is simple and non-mechanical and can be used in single and multi-phase systems. In two-phase systems, it was used in the

redistribution of flow patterns which considerably change the heat transfer characteristics of the system (Norris, et al., 1999) and (Cotton, et al., 2005), (Sadek, et al., 2010), (Ng, et al., 2011) and (Nangle Smith, 2012).

1.3. Research Objective

This study focuses on latent heat thermal storage systems specially those using organic PCMs. Organic PCMs are characterized by being a chemically stable and non-corrosive option for heat storage systems operating at low temperature ranges (below 120 °C). However the main drawback is the low thermal conductivity of these materials which slows down the heat transfer process and limits the capacity of the system.

In this study, a heat transfer enhancement method was identified by using electrohydrodynamic (EHD) techniques and the research objectives are:

- Develop a criteria to quantify the EHD effect on enhancing the heat transfer in the melting process of an organic PCM latent heat thermal storage system.
- Enhance the thermal performance of LHTS by reducing the charging time for a given amount of latent heat.
- Investigate any interfacial phenomena caused by the applied high voltage.
- Understanding the EHD mechanisms of enhancement involved in the project by numerical simulation
- Characterize the thermal performance of the system by estimating the value of different energy components in the storage cell

2. Latent Heat Thermal Storage (LHTS)

In latent thermal storage systems, the energy is stored in the form of phase transformation energy, i.e. the energy required to be absorbed or liberated by the material in changing from one phase to another.

Latent heat storage systems can be subdivided into different types according to the nature of the phase involved and the materials used. The classification of types of latent heat thermal storage systems and the phase change materials (PCMs) used in these systems are presented in Figure 2.1 (Zalba, et al., 2003). Latent heat storage systems are subdivided into gas-liquid, solid-gas, solid-liquid and solid-solid. Gas-liquid and solid-gas systems are accompanied by a large change in volume and an additional power will be required for compressing the gas phase to accommodate this change in volume. This will require an additional preparation for pressure vessels and compressors which will increase the complexity of the system and may reduce the overall energy efficiency of the system.

In solid-solid storage systems, phase transformation occurs in both solid phases where the material only changes its crystalline configuration from a certain lattice configuration to another such as Trimethylolthane (Pentaglycine). The change in enthalpy due to the phase

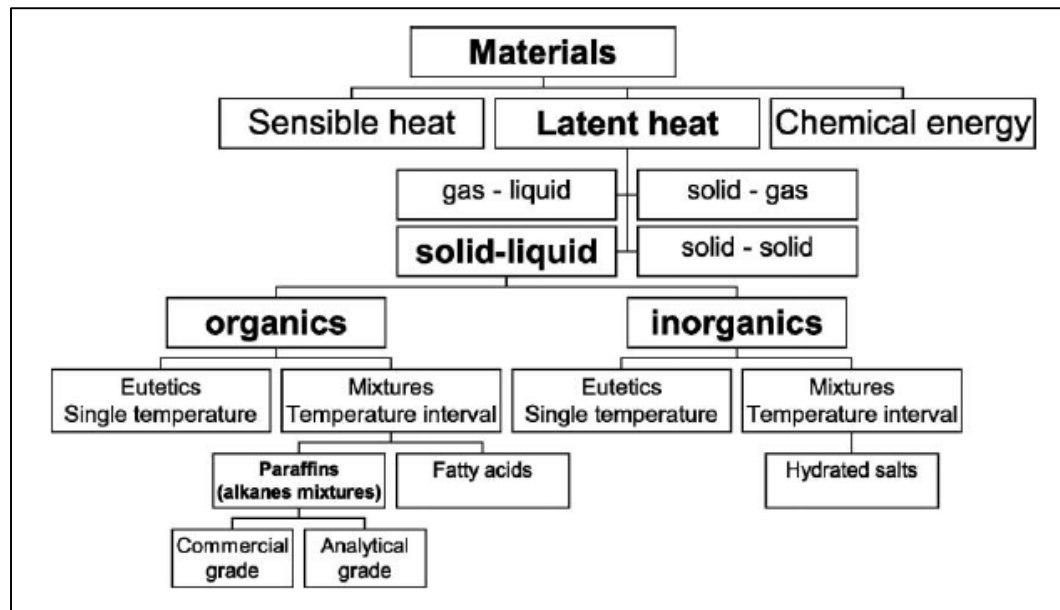


Figure 2.1 Classification of thermal storage materials. (Zalba et al, 2003)

transformations in solid-solid PCMs is in a lower range than that for solid-liquid phase change materials with phase transformation at the same temperature. Therefore, solid-liquid PCMs are a typically better solution for latent thermal storage techniques and the scope of this project is limited to these types of PCMs.

2.1. Solid – Liquid Phase Change Materials

The scope of this project is limited to PCMs with a relatively low melting temperature [0-120°C] as these can be used in low temperature waste heat recovery and solar energy applications. Within this range the PCMs, which can be further subdivided mainly into two main groups: Organic and Inorganic PCMs, which can be further subdivided into their compounds or eutectics (Abhat, 1983) and (Zalba, et al., 2003). In some reviews for

the PCMs the eutectics are separated and classified as a separate group where you can have a eutectic material with an organic-inorganic compound (Sharma, et al., 2009).

2.1.1. Organic PCMs

Organic PCMs can be mainly divided into Paraffin and non-Paraffin (fatty acids) compounds. Paraffins are the widely commercially available PCMs due to the availability of melting temperature range which depends on the length of the carbon chain as represented in Figure 2.2. Non Paraffins usually have a higher latent heat of fusion than the Paraffin PCMs, their main disadvantage over the Paraffins is their higher cost compared to the Paraffins and their flammability which limit them from being exposed to higher temperatures.

PARAFFIN	DISTRIBUTION OF C-ATOMS	OIL CONTENT %	FREEZING POINT/RANGE °C	HEAT OF FUSION		DENSITY AT		SPECIFIC HEAT AT 100 °C KJ/KG.K	THERMAL CONDUCTIVITY (SOLID PHASE) W/M.K	COST (1979) DM/KG	REF.
				KJ/KG	KJ/DM ³	20 °C	70 °C				
- 1)	C14	-	4,5	165	-	-	-	-	-	1.20 ²⁾	20
-	C15 - C16	-	8	153	-	-	-	-	-	0.50 ²⁾	20
5913 ³⁾	C13 - C24	20	22 - 24	189	144	0.900	0.760	2.1	0.21	0.50	4
OCTADECANE	C18	0	28	244	189	0.814	0.774	2.16	0.15	150.0	4
6106 ³⁾	C16 - C28	5	42 - 44	189	145	0.910	0.765	2.1	0.21	0.70	4
P116 ⁴⁾	-	-	45 - 48	210	165	0.817	0.786	2.5	-	0.44 ²⁾	20
5838 ³⁾	C20 - C33	<0.5	48 - 50	189	145	0.912	0.769	2.1	0.21	1.00	4
6035 ³⁾	C22 - C46	4	58 - 60	189	150	0.920	0.795	2.1	0.21	0.60	4
6403	C23 - C46	<0.5	62 - 64	189	150	0.915	0.790	2.1	0.21	1.00	4
6499 ³⁾	C21 - C50	3	66 - 68	189	157	0.930	0.830	2.1	0.21	0.80	4

Figure 2.2 Physical properties of some Paraffins (Abhat 1983)

The organic PCMs can be generally characterized as having good chemical and thermal stability, no phase segregation, almost no or limited supercooling and non-corrosive properties for the metals. However, the organic PCMs also have some draw backs which

include a low thermal conductivity, low latent heat of fusion compared to inorganic PCMs and flammability that is commonly associated with the fatty acids.

2.1.2. Inorganic PCMs

For the inorganic PCMs salt hydrates are the most common of these type of materials. One of the advantages of inorganic salt hydrates is that they are cheap and commercially available, they have a good thermal conductivity relative to that of the organic PCMs, a relatively high latent heat of fusion and an almost defined melting temperature rather than having a melting temperature range which makes them often a better solution from a thermal point of view. However, most of the inorganic PCMs are highly metals corrosive. Also they are characterized by phase segregation and have some problems with thermal stability where their latent heat of fusion degrades with thermal cycles. Another disadvantage of inorganic PCMs is undercooling (supercooling), which is the capability of the liquid phase of the material to go below its freezing temperature without being transformed to solid phase, thus leading to problems in defining the setting temperature and energy storage inefficiency in case of larger supercooling values.

The typical cooling curves for the different PCMs which includes the effect of supercooling is presented in Figure 2.3. It can be seen that, for paraffins, melting occurs over a wider range of temperature than that for the fatty acids while for inorganic salt hydrates, melting occurs at a single temperature. Figure 2.4 summarizes the advantages and disadvantage for both the organic and inorganic PCMs.

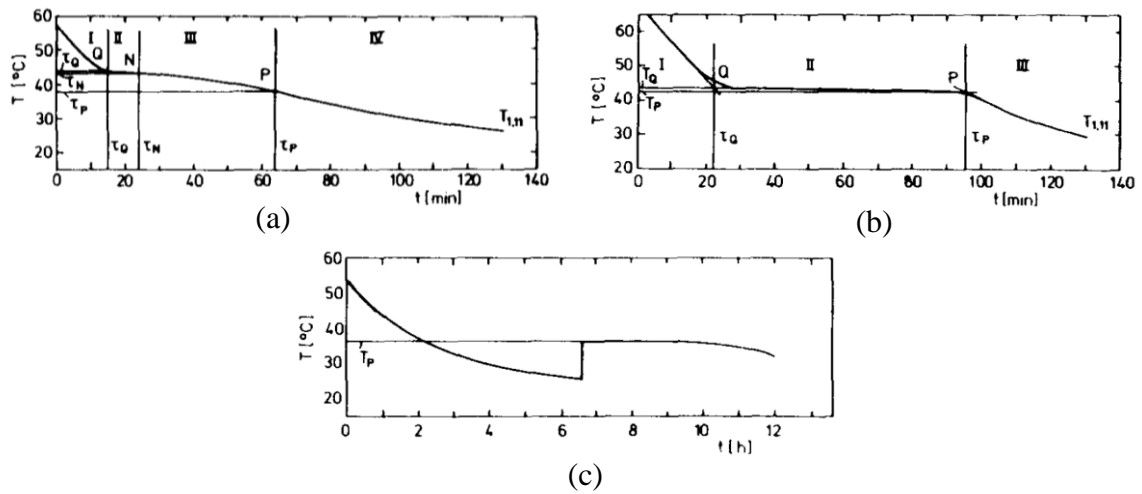


Figure 2.3 Cooling curves for different PCM, (a) Commercial paraffins, (b) Fatty acids and (c) inorganic salt hydrates. (Abhat 1983)

Organics	Inorganics
Advantages No corrosives Low or none undercooling Chemical and thermal stability	Advantages Greater phase change enthalpy
Disadvantages Lower phase change enthalpy Low thermal conductivity Inflammability	Disadvantages Undercooling Corrosion Phase separation Phase segregation, lack of thermal stability

Figure 2.4 Comparison of organic and inorganic PCM for heat storage systems. (Zalba et al., 2003)

Selecting the right PCM for the latent thermal storage system is one of the most important criteria in designing an energy efficient thermal storage system. The basic guidelines for selecting a suitable PCM are summarized by (Kenisarin, et al., 2007) as follows:

- 1- High latent heat of fusion
- 2- Melting temperature range as close to the operating temperature of the application
- 3- A low vapor pressure at the operating temperature
- 4- Chemically stable and non-corrosive for the containing material

- 5- The PCM shouldn't be flammable or hazardous
- 6- The PCM should have a small degree of undercooling
- 7- Low volume variation during solidification and melting phase change
- 8- A high thermal conductivity
- 9- The PCM should be cheap and commercially available

A summary of thermo physical properties, chemical stability and cost for the different PCMs can be found in several reviews as (Sharma, et al., 2009), (Kenisarin, et al., 2007) and (Zalba, et al., 2003).

In the scope of this thesis paraffin wax was used as a PCM due to its low melting temperature of 63 °C range that can be used in low temperature waste heat recovery systems and solar energy applications.

Although organic PCMs appears to be a good solution for thermal energy storage systems, the issue of low thermal conductivity of the organic PCMs used in low temperature ranges must be addressed. The thermal conductivity range for the organic and inorganic PCMs is around 0.1 and 0.6 [W/m.K] (Zhao, et al., 2010) and (Jegadheeswaran, et al., 2009). This decreases the heat addition and heat extraction rates resulting in a longer charging and discharging periods for a given amount of energy when compared to sensible storage systems. By enhancing the heat transfer process in these systems, the amount of energy stored in the PCM during a given time can be increased, resulting in increasing the overall energy efficiency of the system.

2.2. Heat Transfer Enhancement of LHTS Systems

Extensive research has been carried out to investigate heat transfer enhancement in latent heat thermal storage systems both numerically and experimentally. Heat transfer enhancement techniques can be divided into active and passive heat augmentation techniques as mentioned by (Webb, L. and Kim 1994) and (Bergles, 2011). Active heat transfer enhancement techniques involves power being additionally added to the system to enhance the heat transfer process, while the passive techniques do not involve an external power source. Within the scope of this project, the techniques concerned with the heat transfer enhancement in LHTS systems using PCMs will be discussed.

2.2.1. Passive Enhancement Techniques

Most of the research done on heat transfer enhancements in LHTS systems using PCMs was on passive heat enhancement techniques. There are various passive techniques that have been studied in order to increase the heat transfer rate during melting and solidification process to reduce the charging and discharging time or increase the storage capacity of the system. These techniques can be mainly divided into 4 categories as reported by (Jegadheeswaran, et al., 2009) and (Agyenim, et al., 2010) :

- I. Using extended surfaces
- II. Thermal conductivity enhancement
- III. Employing multiple PCMs method
- IV. Micro-encapsulation of PCM

I. Extended Surfaces

Extended surfaces techniques such as fins are based on increasing the heat transfer area in the thermal system to increase the total rate of heat transfer. Fins offer an increased surface area advantage, while they have an adverse effect on the weight and the volume of the thermal storage system for a given storage energy required. (Sanusi, et al., 2011)

Extensive research has been carried out by (Henze, et al., 1981), (Velraj, et al., 1999), (Stritih, 2004) and (Nayak, et al., 2006) to investigate the effect of adding fins to the latent heat storage system on the melting and solidification behavior of the PCM. Fin thickness, fin height, number of fins, spacing between the fins and the orientation of the fins has been studied in order to optimize the performance of the system with the minimum number of fins to minimize the decrease in the storage capacity for a given volume due to the addition of the fins.

A numerical investigation was carried out by Lacroix & Benmadda (1997), which studied the melting behavior of a PCM from a finned vertical wall. The numerical model was validated by experimental data. The effect of the fin length, the spacing between the fins and the heating wall temperature was investigated. The geometry investigated is presented in Figure 2.5, where the number of fins can be changed and their length, L , can be changed. In Figure 2.6 the temporal profile for the melt volume fraction (MVF) is plotted for different melting cases including short and long fins and comparing it with a no fins case. In short fins systems ($L/W=0.25$), it was found that the melting rates was

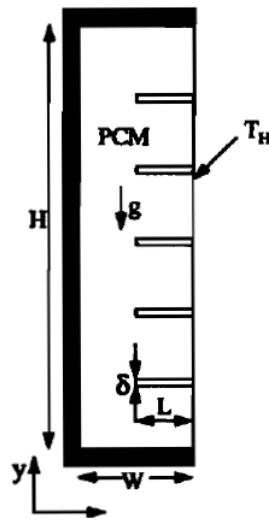


Figure 2.5 Schematic representation for the PCM geometry. (Lacroix and Benmadda 1997)

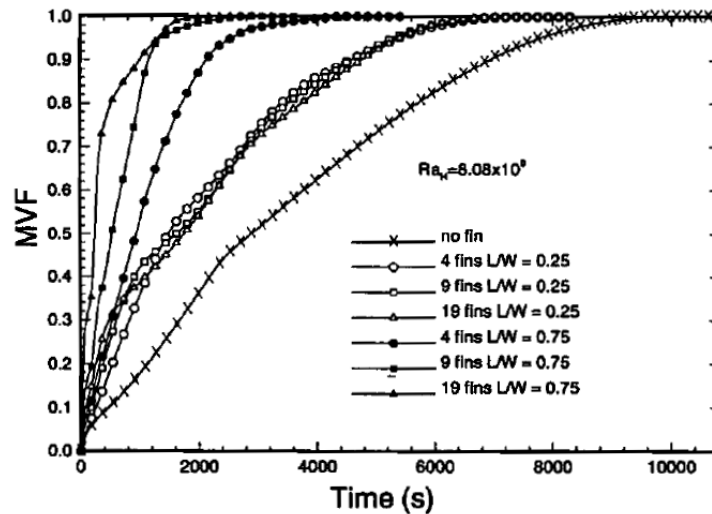


Figure 2.6 Melt volume fraction variation with time. (Lacroix and Benmadda 1997)

it proceeds with almost the same rate as the no fins case. Longer fins ($L/W=0.75$) showed a better enhancement rate than the shorter fins. Increasing the number of fins from 4 to 9 fins improved the performance in the melt front progress, however increasing the fins from 9 to 19 fins showed a better enhancement only for the early stages of melting and a

decreasing performance after that due to the effect of the fins on hampering the buoyancy driven flows. In case of using longer fins, when using 9 fins the melting time was reduced by 70 % over the no fins case and when using 19 fins the melting time was reduced by 73 %. By using 19 long fins with $L/W=0.75$, the fins occupied $\approx 7\%$ of the volume of the storage cell. It was concluded that using a few longer fins is more effective than using many short fins.

An experimental investigation was carried out by (Stritih, 2004) for a vertical heated wall with horizontal fins array and was compared with a no fins case. The fins occupied $\approx 5\%$ of the volume of the storage cell. The heat was transferred into the system by a water heat exchanger on the side of the wall. The quantity of the heat input to the system was analyzed using volume flow of the water together with the measured inlet and outlet temperatures. A fin effectiveness (η_f) was defined as the ratio between the heat flux into the PCM with and without fins. The dimensionless numbers; Fourier number (Fo) and Stefan number (Ste) were used in the results. The Fourier number ($Fo = \alpha t^2 / l$) is a dimensionless parameter that is used to characterize transient heat conduction problems. The Stefan number ($Ste = c_p \Delta T / \Delta H_f$) is a dimensionless parameter used in characterizing phase change problems, it is defined as the ratio between the sensible energy stored and the latent heat. These two terms combined can be used in characterizing a conduction dominated phase change problem. A relation between the fin effectiveness and the dimensionless number $Fo \times Ste$ is presented in Figure 2.7. The results showed that the fin effectiveness during melting was less than 1 at low Fourier number. This was due to the reduction of the natural convection in the presence of the

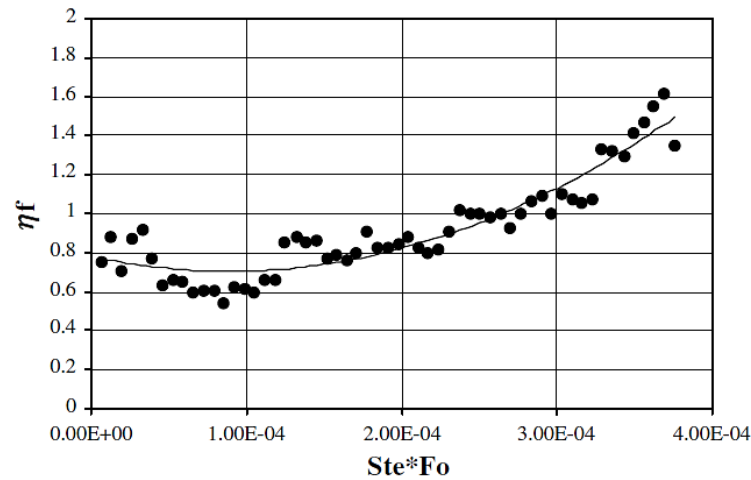


Figure 2.7 Fin effectiveness at melting with dimensionless time. (Stritih 2004)

fins where natural convection dominated melting was occurring in case of no fins. At high Fourier numbers the fin effectiveness number reached 1.6. It was concluded that fins were not effective in case of melting but rather had a negative effect due to reducing natural convection, while in case of solidification the solidification time was reduced by 40 %.

A vertical fins emerging from a horizontal heated wall configuration was studied numerically by Shatikian, et al. (2005). In order to keep the percentage volume occupied by the fins inside the storage cell constant, the ratio of the PCM layer to the fin thickness was kept constant. This means that increasing the spacing between the fins must be accompanied by increasing the fin thickness. The volume ratio of the fins with respect to the size of the storage cell was kept at 23 %. The effect of fin height, fins spacing and the temperature of the heating wall on the rate of melting under a constant temperature wall boundary condition were also investigated. It was found that as the temperature of the heating wall increases the initial heat flux increases and the melting time decreases. It was

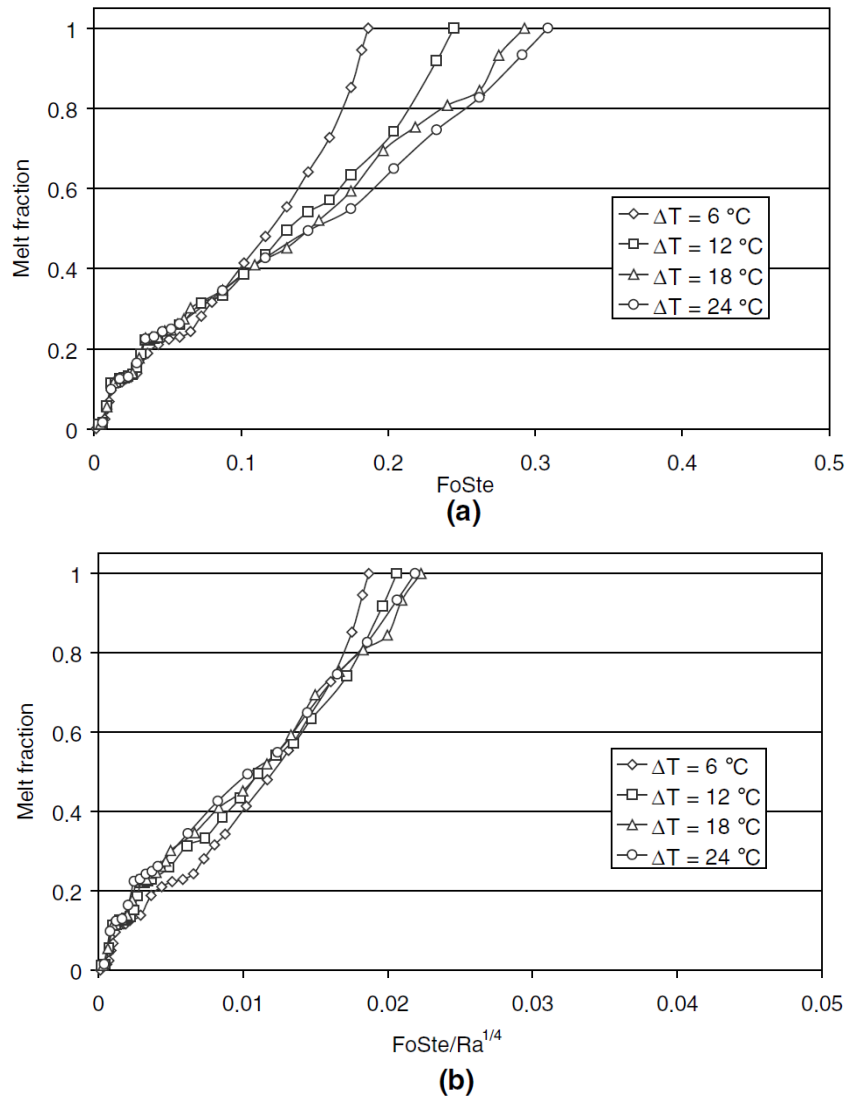


Figure 2.8 Melt Fraction vs. (a) $Fo \times Ste$ (b) $Fo \times Ste / (Ra^{0.25})$ (Shatikian, et al., 2005)

observed that as the spacing between the vertical fins decrease (i.e. increase number of fins) the heat flux increases and the melting time decreases.

In Figure 2.8a, the melt fraction versus the dimensionless time parameter ($Fo \times Ste$) is plotted for a 4 mm fin spacing configuration and different degrees of superheating. It is observed that the data collapses at the early stages of the melt fraction where natural

convection is not yet dominant and deviates as the melt fraction increases where natural convection becomes significant for higher degrees of superheating. To account for natural convection effect, the Rayleigh number was introduced into the dimensionless time and the melt fraction is then plotted against $Fo \times Ste/Ra^{0.25}$. The exponent of Rayleigh number was chosen based on laminar natural convection from an isothermal vertical surface correlation. In Figure 2.8b, by introducing the Rayleigh number the data collapses together for different degrees of superheating. The authors did not perform the numerical simulation on different phase change materials to test for different physical properties.

I. Thermal Conductivity Enhancement

As mentioned previously the main problem associated with the PCMs operating in low temperature is their low thermal conductivity ranging from 0.1 to 0.6 [W/m.K]. A selection of PCMs and their thermal properties are presented in Table 2.1.

Introducing high thermal conductive materials inside the PCMs has a similar effect of increasing the thermal conductivity of the system. Depending on the volume fraction of the added material to the PCM, the effective thermal conductivity of the system will change. Increasing the effective thermal conductivity of the PCM was studied extensively by several researchers and the techniques used to achieve that can be summarized into 3 main categories which are:

- 1- Using high conductivity porous materials implemented inside the PCM.
- 2- Addition of highly thermal conductive particles in the PCM.
- 3- Adding metal structures in the PCM.

Table 2.1 Thermal conductivity and latent heat of fusion of selected PCMs. (Jegadheeswaran 2009)

Name of the PCM	Thermal Conductivity [W/m.K]	Latent Heat of Fusion [kJ/kg]
Organics		
n-Octadecane	0.35(solid) and 0.149 (liquid)	245
n-Docosane	0.22	194.6
Paraffin wax	0.514(solid) and 0.224(liquid)	251
Caprylic acid	0.149	149
Capric acid	0.153	153
Inorganics		
KNO ₃	0.5	266
NaNO ₃	0.5	172
MgCl ₂ .6H ₂ O	0.694(solid) and 0.57(liquid)	168.6
CaCl ₂ .6H ₂ O	1.008(solid) and 0.54(liquid)	190.8
Inorganic eutectics		
58.7%Mg(NO ₃).6H ₂ O-	0.678(solid) and 0.51 (liquid)	132
41.3%MgCl ₂ .6H ₂ O		
66.6%Urea-33.4%NH ₄ Br	0.682 (solid) and 0.331 (liquid)	161

Porous structures implemented could be either metal matrices made from highly thermal conductive materials like aluminum or copper, or a naturally available porous material such as graphite. A numerical study was carried by Mesalhy, et al. (2005) for a horizontal annulus geometry with the PCM impregnated into a porous matrix. The effect of using different conductive materials for the porous matrix and the porosity of the matrix on the thermal performance of the LHTS was examined. It was concluded that using higher

thermal conductivity for the porous matrix increases the rate of heat transfer to the PCM. Results showed that decreasing the porosity of the matrix leads to an increase in the melting rates due to the increase in the surface area. However, this dampens the natural convection inside the PCM, yet still higher than pure PCM without a porous matrix.

Graphite can be used as a naturally porous material. It is characterized by its high thermal conductivity which varies from 24 to 470 W/m.K. The porous graphite matrices can be either in the form of natural graphite flakes or expanded graphite (EG).

Due to the high thermal conductivity of graphite, its inclusion in PCM systems has the effect of increasing the effective thermal conductivity of the system by 5 to 100 times depending on the density of the graphite added into the system (Haillot, et al., 2008). Sari & Karaipekli (2007) used expanded graphite (EG) with different mass fractions embedded in a paraffin based LHTS. The results indicate that by increasing the mass fraction of EG, the thermal conductivity can be increased however this will lead to a decrease in the storage capacity. The optimum mass fraction was taken to be 10% of EG and the thermal conductivity increased by almost three times. It was observed that using a 10% mass fraction of EG to form a composite PCM decreased the melting time by 32 %, and using a 4% mass fraction the melting time decreased by 16 %.

Further attempts to increase the effective thermal conductivity without decreasing the storage capacity of the system were performed by Kim & Drzal (2009). Kim & Drzal tried to improve the effective thermal conductivity of paraffin by stirring exfoliated

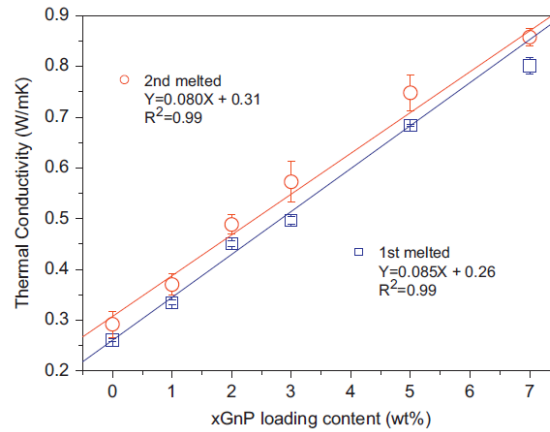


Figure 2.9 Thermal conductivity of paraffin/xGnP composite. (Kim and Drzal 2009)

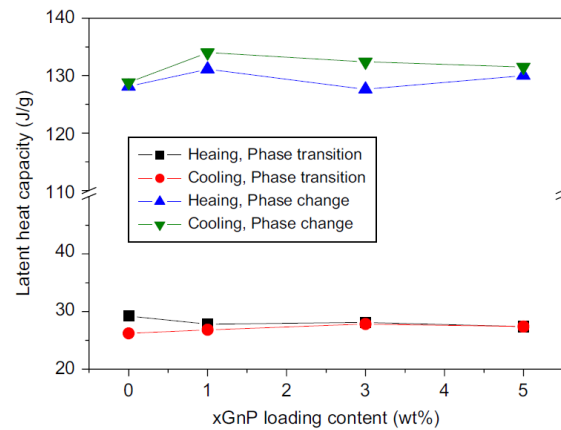


Figure 2.10 Latent heat storage of paraffin/xGnP composite with the loading content. (Kim and Drzal 2009)

graphite nano platelets (xGnP) in liquid paraffin. The effective thermal conductivity enhancement against the loading content of xGnP is presented in Figure 2.9. It is observed that the effective thermal conductivity increased by three times at 7% loading content with xGnP over the pure PCM. The storage capacity of the system was found to be almost the same as that of pure PCM regardless of the loading content of the xGnP as shown in Figure 2.10.

Other forms of carbon materials such as carbon fibers and carbon nano tubes showed a similar effect to the graphite while being added to the PCM. The carbon nano tubes are characterized by their unusual high thermal conductivity reaching 6600 W/m.K (Berber, et al., 2000).

The carbon fibres were tested by Nakaso, et al. (2008) to investigate the heat transfer enhancement in thermal storage tanks. Two configurations of the carbon fibres were tested: carbon cloth and carbon brushes, they are both represented in Figure 2.11. The use of carbon fibres doubled the effective thermal conductivity of the system. It was reported that the use of a fiber cloth showed an improved enhancement over the carbon brush due to being more continuous than the carbon brush. As previously shown, increasing the loading content percentage of the additive material usually enhances the effective thermal conductivity of the system, however in case of using the carbon fibres by Nakaso, et al. (2008) a volume percentage of 1 % could only be reached due to the low packing density of the carbon fibres used.

A higher packing density can be achieved by compressing the carbon materials. By using CENG (compressed expanded natural graphite), the percentage can be increased up to a 5 %. The CENG matrix cubes are soaked into the melted paraffin wax, and the paraffin wax is impregnated by the aid of capillary forces into the porous graphite matrix forming a stable composite material.

These types of composites were studied and characterized by Py, et al. (2001) and proved that high thermal conductivities can be achieved. It was stated that these materials present a

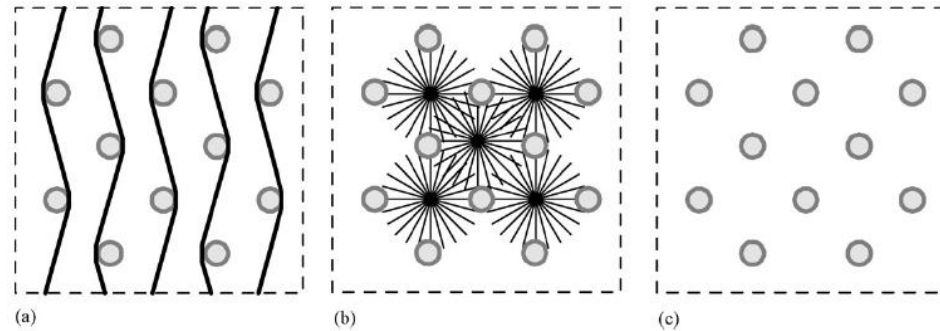


Figure 2.11 (a) Carbon fiber cloth (b) Carbon fiber brush (c) No carbon fiber. (Nakaso et al. 2008)

strong anisotropy issue in the axial and radial directions due to how it is mechanically compressed. Although Graphite/PCM composites exhibit a high enhancement and increase the effective thermal conductivity, these graphite composites must be prepared through chemical and mechanical processes such as heat treatment, drying, grinding and compression which are energy intensive and time consuming.

Another technique of enhancing the effective thermal conductivity is the dispersion of metal pieces, metal powders, metal balls and beads. Copper pieces as additives into the PCM were tested by Mazman, et al. (2008) and was found that the heat transfer rate was increased by up to 70 %. Additionally aluminum powder dispersed into the PCM and its effect on the melting behavior was studied by Mettawee & Assassa (2007), they found that the charging time was reduced by 60% over the pure PCM case without addition of the aluminum powder.

Adding metal structures into the PCM was shown to improve the effective thermal conductivity. Velraj, et al. (1999) studied the effect of adding a hollow cylindrical steel structures into a LHTS using paraffin as the PCM, such structure is called lesser rings. A

considerable reduction in the solidification time was achieved by using the lesser rings, it was reported that the solidification time was reduced to 1/9th of that of pure PCM with no lesser rings. However this enhancement rate was only achieved when the lesser rings occupied 20 % of the volume of the storage cell.

A less discontinued structures such as metal foams were also investigated. Metal foams offer a high porosity ranges from 85 % to 97 % and a high thermal conductivity. Phase change heat transfer in metal foams/PCM composites has been investigated by Tian and Zhao (2009 and 2011) experimentally and numerically. Metal foams were embedded in PCM subjected to a constant heat flux boundary condition. The melting behavior was investigated for different porosities and pore sizes of the metal foams. It was observed that the overall heat transfer rate can be increased by 3 to 10 times by using metal foams inside the PCM. A comparative study between the heat transfer enhancement caused by using Metal foam/PCM composite and that of using EG/PCM composite was performed by Zhou & Zhao (2011). Experiments for different configurations were performed under a constant heat flux, this implies lower degree of superheat for the heating element means a better heat transfer. Figure 2.12 shows that metal foams has a higher heat transfer enhancement effect over that of EG/PCM composites, due to the fact that metal foams provide a more continuous structures into the PCM rather than the sparse structures formed by using EG. It was concluded that better heat transfer can be achieved by using metal foams with lower porosity and a higher pore density.

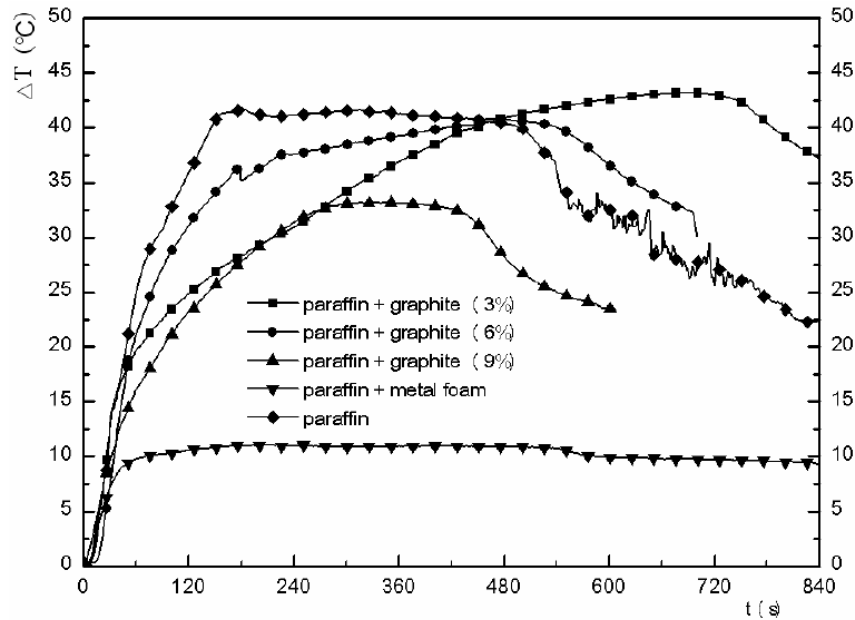


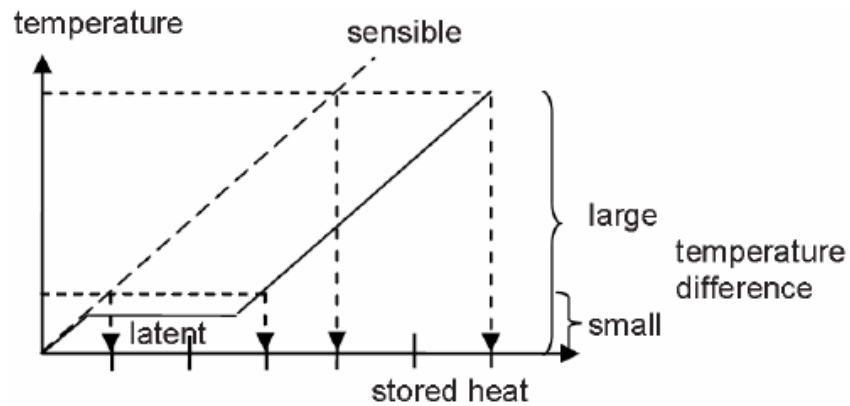
Figure 2.12 Surface degree of superheat variation with time for EG/PCM and metal foam/PCM composite subjected to constant heat flux. (Zhou and Zhao 2011)

II. Employing Multiple PCMs Method

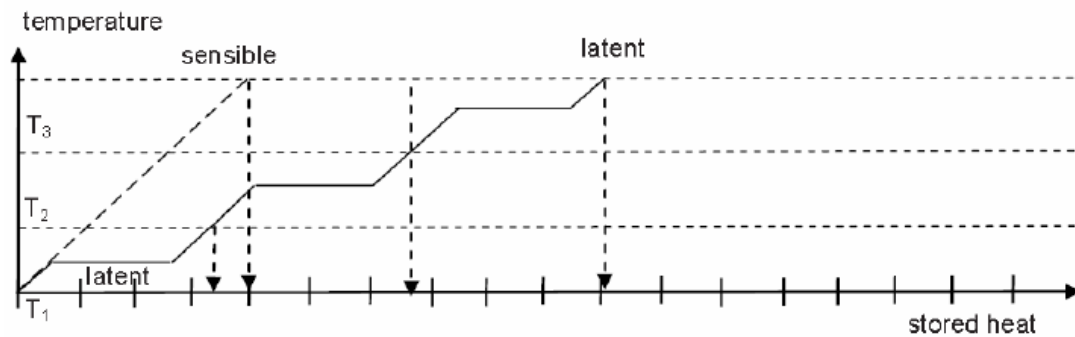
Another technique that can be used to enhance the performance of a LHTS by increasing the storage capacity is employing different PCMs with different melting temperatures in one system. The main idea behind this technique stems from the idea that the heat transfer process from the heat transfer fluid (HTF) to the PCM is dependent on the temperature difference between the two sides. This implies that this temperature difference would decrease in the direction of the flow of the HTF leading to a decrease in the heat transfer rate and resulting in a poor storage system performance. Using multiple PCMs with decreasing melting points in the direction of flow such that the temperature difference between the HTF and the melting point of the PCM is always kept within a suitable range, will ensure that each PCM will be provided with almost the same heat

flux. This result in an increase of the storage system performance. The use of latent heat storage systems is advantageous over sensible systems due to higher energy storage density over a small temperature difference range. As the temperature difference increases the advantage of using latent heat over sensible heat storage decreases. A schematic diagram for the sensible and latent energy stored in a single PCM storage unit is presented in Figure 2.13a. In case of small temperature difference across the HTF side, the ratio between the heat stored as latent energy in a given mass of the PCM to that as sensible energy for the same mass is equal to 3. As the temperature difference across the HTF increases, this advantage decreases and the ratio decreases down to 1.5.

Using cascaded PCMs is to overcome this decrease in advantage in case of large temperature difference across the HTF side. Figure 2.13b shows a three-stage cascaded latent heat storage system using three different PCMs, each with a different melting point. The low melting temperature PCM stores energy through temperature range of T_1 and T_2 across the HTF side, the medium melting PCM temperature stores energy through temperature range T_2 and T_3 and the high melting temperature PCM stores energy through temperature range between T_3 and T_4 . As reported by Mehling & Cabeza (2008) due to using such cascaded systems the ratio between the energy stored in the three cascaded stage latent heat systems is 2.5 times that of using a single sensible heat storage.



(a) With a single PCM



(b) With cascaded latent heat storage

Figure 2.13 Stored heat for Sensible and Latent storage systems using single and cascaded PCMs. (Mehling and Cabeza, 2008)

III. Microencapsulation of PCMs

Microencapsulated PCMs are used to increase the heat transfer rate between the heat source/sink and the PCM. They are PCMs in micro size which forms the core whether solid or liquid and enclosed by a shell. The idea behind using microencapsulated PCM is that they provide a very large heat transfer area per unit volume, thus increasing the heat transfer rate to the PCM. Another advantage is that they are less chemically reactive with the container material and more able to withstand volume change during the phase change

process. One of the major drawbacks of the microencapsulation of PCMS is a greater chance of supercooling which eventually will lead to decrease in the performance of the energy storage system. Designing a successful LHTS using microencapsulation requires careful consideration of the shell (PCM container material). The main issues that should be taken into account are: (Castellon, et al., 2005) :

- 1- Compatibility of the container material with the PCM, in terms of any chemical unexpected behavior such as softening of types of plastics by some organic materials.
- 2- Container must be able to adapt to volumetric changes occurring during the phase change process.
- 3- Mechanical stability and easy handling.
- 4- The cost and availability of the container material.

Extensive research has been done on the container material and different methods of encapsulation. Different encapsulation strategies have been investigated, Stark (1990) studied the encapsulation of PCMs into the micropores of an ordered polymer film and the product exhibited an excellent mechanical stability under cyclic melting-solidification phase change processes.

The thermal performance of microencapsulated PCMs was investigated by Felix Regin, et al. (2005) and a comparison between cylindrical and spherical capsules was performed. Results showed that the temperature of the heat transfer fluid around the capsule and the radius of the capsule have a strong effect on the heat transfer rate. The solidification time was increased by increasing the radius of the capsule and was decreased by decreasing the

temperature of the HTF. Additionally, it was found that the solidification time for cylindrical capsules was almost 50 % less than that of spherical capsules with the same volume and heat transfer area. It was concluded that using cylindrical capsules for microencapsulating the PCM is the most preferable.

2.2.2. Active enhancement techniques

There are few published studies concerning the use of active enhancement techniques in solid-liquid LHTS phase change heat transfer processes. The main advantage of active heat transfer enhancement techniques compared to passive techniques is their ability to control the level of heat transfer enhancement. This control is achieved by varying the applied voltage level in case of electrohydrodynamic (EHD) or by varying the power level of the ultrasonic vibrators in case of ultrasonic enhancement.

Using active heat transfer enhancement techniques in thermal storage systems is only practical if the power consumed is very small compared to the heat input to the thermal storage system.

The only active enhancement techniques that was previously studied for solid-liquid heat transfer phase change processes are the use of ultrasonic vibrations and EHD.

IV. Ultrasonic vibrations

The effect of ultrasonic vibrations on the melting process of a PCM was investigated by Oh, et al. (2002). A comparative study was done for the melting behavior of a Paraffin (n-octadecane) subjected to a constant heat flux boundary condition using ultrasonic

vibrations and no active enhancement. It was found that the melting time can be reduced by ≈ 3 times using ultrasonic vibrations. Figure 2.14 represents the heater surface temperature variation with time under two different heat flux values and for ultrasonic vibrations and melting without ultrasonic vibrations. It is observed that the early stages of melting for all cases there is a steep increase in temperature which represents conduction dominated heat transfer, following this, melting by convection dominated heat transfer occurs. The sudden temperature increase at the end of experiment when melting with ultrasonic vibrations was explained by the bubbles covering the heater surface formed by the ultrasonic vibrations. Using ultrasonic vibrations introduced acoustic waves inside the molten PCM which is a series of compression and expansion waves. The expansion waves caused the formation of microscopic bubbles.

Figure 2.15 shows the temperature history at a position corresponding to the ultrasonic vibrators against normalized time (time divided by the time to completely melt the PCM). It can be observed that for melting with ultrasonic vibrations the temperature always falls below that of unaided melting, for a case of constant heat flux boundary condition this indicates a better heat transfer coefficient. The heat transfer enhancement was reported to be due to the following effects: acoustic streaming, cavitation and thermally oscillating flow.

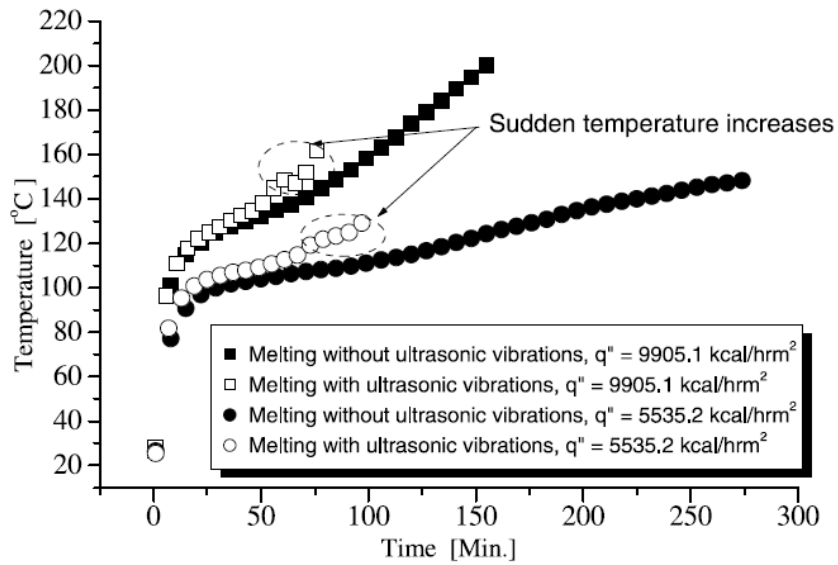


Figure 2.14 Heater surface temperature variation with time. (Oh et al. 2002)

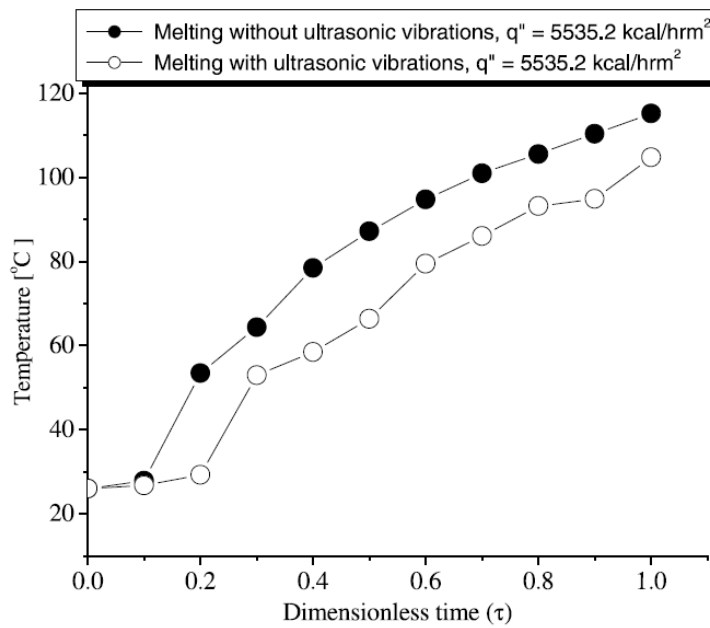


Figure 2.15 Temperature history against normalized time. (Oh et al. 2002)

The electric energy (Wh) consumed by the electric heater and the total electric energy consumed by both the electric heater and the ultrasonic vibrators were calculated and are presented in Table 2.2. As the power level of the ultrasonic vibrator increase the melting time decreases, however, at the end the total electric consumption is almost the same for all different cases. It was reported by the author that the electric consumption of the ultrasonic vibrators could decrease by applying it directly to the PCM instead of transmitting the vibration through water to the PCM.

It can be concluded that ultrasonic vibrations can serve as an active heat enhancement technique for phase change heat transfer in melting and solidification, however the power consumption by this technique is significant. For the 5535.2 kcal/h m² heat flux case, the melting time was reduced by ≈ 3 times by using ultrasonic vibrators compared to the unaided melting, however the energy consumption from the ultrasonic vibration generator was almost 2 times that of the heater.

An active enhancement technique with lowest power consumption will be the ideal active technique. One of these techniques is electrohydrodynamics (EHD), it has been studied extensively and proven to be one of the less power consumption active techniques for single phase and multi-phase (liquid-vapor) systems.

It will be discussed in details in the next section with the previous related work in heat transfer in phase change melting and solidification.

Table 2.2 Comparison of the total consumed electricity for a melting process. (Oh et al.2002)

Heat flux (kcal/h m ²)	Melting time (min)	Heater (Wh)	Ultrasonic vibration generator (Wh)	Total consumed electricity (Wh)
9905.1	161	448.1	–	448.1 ^a
	76	211.5	–	445.9 ^b
5535.2	275	444.6	–	444.6 ^a
	94	152.0	–	441.8 ^b

^a Melting with a heater.

^b Melting with a heater and ultrasonic vibrations.

A review for the previous work on the heat transfer enhancements for latent heat thermal storage systems including the results of the present work investigated in this thesis is shown in Table 2.3.

Table 2.3 Review of previous work on heat transfer enhancements in latent heat thermal storage systems

Authors	Method of Enhancement	% Volume	Level of enhancement	Notes
(Velraj, et al., 1999)	<ul style="list-style-type: none"> • Aluminum Fins • Lessing rings 	<ul style="list-style-type: none"> • 7 % • 20 % 	<ul style="list-style-type: none"> • Solidification time decreased by 4 times • Solidification time decreased by 9 times 	Comparative study between effect of adding fins and lessing rings
(Lacroix, et al., 1997)	Horizontal Fins	7	Melting time reduced by 70 %	Numerical- Melting
(Stritih, 2004)	Horizontal fins	5	<ul style="list-style-type: none"> • Maximum fin effectiveness ≈ 1.6 during melting • Maximum fin effectiveness ≈ 2.7 during solidification 	Experimental study. It was found that fins damped natural convection and the total melting time was increased
(Sarı, et al., 2007)	Expanded graphite matrix	Mass fraction $\approx 10\%$	Melting time was reduced by 32 %	
(Mettawee, et al., 2007)	Aluminium powder dispersion	Mass fraction $\approx 0.5\%$	The melting time was reduced by 60 %	
(Tian, et al., 2009)	Porous metal foams	95 % porosity	The overall heat transfer rate can be increased by 3 to 10 times	
(Oh, et al., 2002)	Ultrasonic vibrations	N/A	Melting time reduced by ≈ 3 times	The vibrator power consumption was equal to $\approx 65\%$ of the energy stored in the PCM. However the author reported that this value can be decreased significantly
Present Study- Nakhla, 2013	Electrohydrodynamics (EHD)	$\approx 1.5\%$	Melting time was reduced by 40 %	EHD power consumption was equal to $\approx 2.5\%$ of the energy stored in the PCM

3. Electrohydrodynamic (EHD) Heat Transfer Enhancement

3.1. Introduction

Electrohydrodynamic (EHD) is the study of dielectric fluid motion due to the application of electric fields. The governing equations of (EHD) and the effect of applying high voltage electric fields on dielectric fluids and enhancing the heat transfer process will be discussed.

3.2. Governing Equations

The mass conservation, momentum conservation and energy conservation equations for a laminar fluid motion under the effect of applying electric fields with Boussinesq approximation are:

- Mass Conservation

$$\frac{\partial \rho}{\partial t} + \rho \nabla \cdot (\bar{u}) = 0 \quad (3.1.)$$

- Momentum Conservation

$$\rho \frac{\partial \bar{u}}{\partial t} + \rho (\bar{u} \cdot \nabla) \bar{u} = -\rho \bar{g} \beta (T - T_0) - \nabla P + \bar{f}_{eB} + \mu \nabla^2 \bar{u} \quad (3.2.)$$

- Energy Conservation

$$\rho c_p \frac{\partial T}{\partial t} + \rho c_p \bar{u} \cdot \nabla T = k \nabla^2 T + q_{eB}''' \quad (3.3.)$$

Due to presence of electric field, an additional terms arise in the momentum and energy conservation equations. In the momentum conservation equation an additional electric body force, \bar{f}_{eB} , is added which influences the flow. In the energy conservation equation an energy generation term, q_{eB}''' , is added.

The derivation of these additional terms were first developed by Chu (1959) as

$$\begin{aligned} \bar{f}_{eB} = & \rho_e \bar{E} + J_x \bar{B} - \frac{1}{2} E^2 \nabla \epsilon - \frac{1}{2} H^2 \nabla \mu \\ & + \nabla \left[\frac{1}{2} \rho E^2 \left(\frac{\partial \epsilon}{\partial \rho} \right)_T + \frac{1}{2} \rho H^2 \left(\frac{\partial \mu}{\partial \rho} \right)_T \right] \end{aligned} \quad (3.4.)$$

The different terms at the right hand side of equation (3.4.) from left to right are: Coulomb force /electrophoretic force, electromagnetic force acting on moving charges, dielectrophoretic force due to a change in permittivity in the system, magnetic forces due to change in permeability, the electrostriction and magnetostriction forces.

$$\begin{aligned} q_{eB}''' = & (\bar{J} - \rho_e \bar{u})(\bar{E} + \bar{u} \times \bar{B}) + \nabla \\ & \cdot [(\bar{E} + \bar{u} \times \bar{B}) \times (\bar{H} - \bar{u} \times \bar{D})] \\ & + \left[\bar{E} \frac{d}{dt} \left(\frac{\bar{D}}{\rho} \right) + \bar{H} \frac{d}{dt} \left(\frac{\bar{B}}{\rho} \right) \right] \end{aligned} \quad (3.5.)$$

The heat generation term due to the effect of applied electric fields can be also divided to different components (Chang, et al., 1994). These components on the right hand side of the equation from left to right are: heat generation due to flow of charged particles,

energy due to fluid polarization, and energy due to time varying electric and magnetic fields which are energy stored in electromagnetic fields as that in coils and capacitors.

In case of dielectric fluid flows, the magnetic field components arising from charges motion in the fluid may be neglected due to the low conductivity of dielectric materials which is between 10^{-10} to 10^{-16} S/m resulting in negligible electric currents. The energy and electric body force equation can then be simplified to

$$\bar{f}_{eB} = \rho_c \bar{E} - \frac{1}{2} E^2 \nabla \varepsilon + \frac{1}{2} \nabla \left[E^2 \left(\frac{\partial \varepsilon}{\partial \rho} \right)_T \right] \quad (3.6.)$$

$$q'''_{eB} = \sigma_e E^2 \quad (3.7.)$$

The energy generation term is often called ohmic heating or Joule heating which is basically heat generation due to current flowing across a conductor. For the present study the maximum energy generation in the fluid was determined to be 0.32 W, which is approximately 4.4 % of the lowest heat input to the system.

Maxwell equations are applied to evaluate the electric and magnetic field distribution in the fluid domain. Maxwell equations represent the fundamental governing laws for electrostatic and electromagnetic phenomena, which are four main equations: Gauss's law, Faraday's law, Ampere's law and the conservation of charges law.

- Gauss's law

$$\nabla \cdot \bar{D} = \rho_e \quad (3.8.)$$

$$\nabla \cdot \bar{B} = 0 \quad (3.9.)$$

- Faraday's law

$$\nabla \times \bar{E} = -\frac{\partial \bar{B}}{\partial t} \quad (3.10.)$$

- Ampere's law

$$\nabla \times \bar{B} = \mu_0 \bar{J} + \mu_0 \epsilon_0 \frac{\partial \bar{E}}{\partial t} \quad (3.11.)$$

- Conservation of charges law

$$\nabla \cdot \bar{J} + \frac{\partial \rho_e}{\partial t} = 0 \quad (3.12.)$$

3.2.1. EHD Body Forces

The three terms on the right hand side of equation (3.11) represent the electrophoretic, dielectrophoretic and electrostrictive components respectively of the EHD body force acting on a dielectric fluid.

The electrophoretic force acts on the free charges in the fluid causing charge migrations due to the applied electric field. The free charges in the fluid could be an existing charges or charges being injected from the electrodes into the fluid. Charges might build up in a medium when subjected to an electric field due to non-homogeneity in the electrical conductivity of the medium which could be due to temperature gradients inside the fluid domain or an inhomogeneous fluid. Figure 3.1a shows the motion of the free charges along the stream lines of the electric field towards the opposite charged electrode. The induced motion in the fluid by the cause of the electrophoretic force will be strongly

dependent on the nature of existence of charges whether being injected from the electrode or charge induction inside the fluid.

The last two terms on the right hand side of equation (3.6.) are usually called the Polarization forces, as these two terms are related to the electric permittivity of the material and arise as an effect of material polarization due to applied electric field. The electric permittivity of the material is a measure of how easily a dielectric material polarizes in response to an electric field.

The second term in equation (3.6.) is called dielectrophoretic component which arises due to spatial change in permittivity of the fluid. This spatial change in permittivity can be due to the presence of multi-phases in the system or due to non –uniform electric field.

The third term in equation (3.6.) is called the electrostrictive force, this force is a gradient force which arises due to the change in permittivity with density.

The polarization forces are usually of significant importance in multiphase systems, as the term $\nabla\epsilon$ becomes significantly large at the two phase interface (surface of discontinuity).

The dielectrophoretic force becomes an interfacial force in two phase systems, in case of liquid vapor multiphase systems it causes the extraction of the liquid phase (higher permittivity fluid) towards regions of higher electric fields in a phenomena known as liquid extraction as in Figure 3.1 part(c) (Melcher, 1963), (Yabe et al 1987a) and (Singh et al 1995).

These interfacial forces cause instabilities at the interface that can allow the fluid to overcome the gravitational and surface tension forces, resulting in changes in the flow patterns that accordingly may change the heat transfer coefficient for these systems.

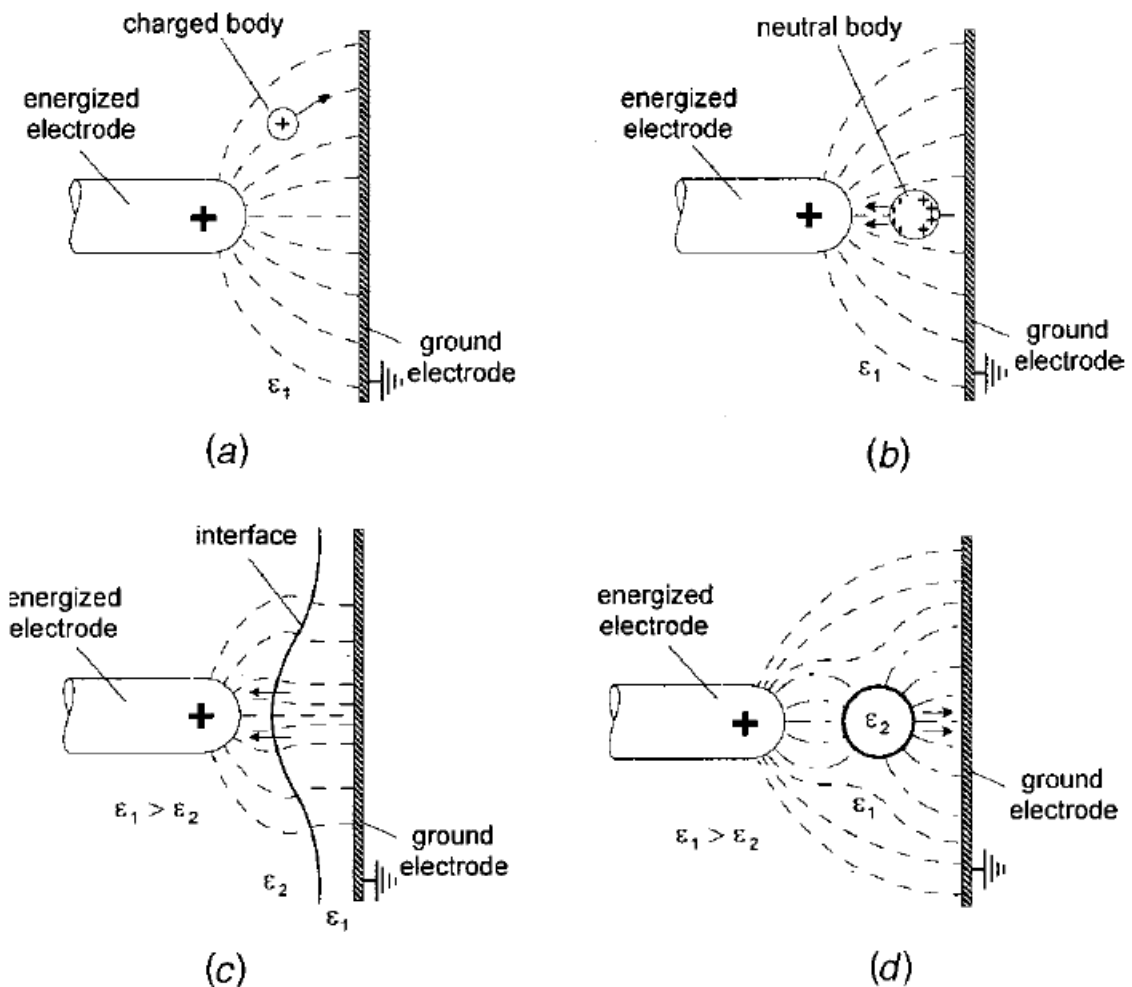


Figure 3.1 Schematic EHD forces and electric field lines. (a)Electrophoretic force (b) dielectrophoretic (polarization) in single phase (c) EHD forces on interface (d) EHD forces acting on a suspended droplet or bubble. (Bryan, et al., 2001)

Polarization forces have a role also for forces on suspends (droplets, bubbles or solid particles in a fluid). In Figure 3.1 part (d) a bubble with a lower permittivity than that of the surrounding medium will be pushed towards regions of lower electric field strength.

3.3. Single Phase EHD Heat Transfer Enhancement

In single phase applications, EHD forces are mostly simplified to only electrophoretic force. The polarization forces are strongly dependent on spatial change of permittivity which is not typically significant for single phase systems. The electrophoretic force acts on charged particles in the fluid. The effect of this force on a fluid was first described by Avsec, et al. (1937) as electroconvective eddies, also known as electroconvection. Fernández, et al. (1987) studied electroconvection on an enhanced oil heater of annular cross section. High voltage was applied at the center electrode while grounding the outer cylinder. In case of no axial flow (stagnant fluid), by applying high voltage, a radial motion of the fluid (oil) was observed forming a well-defined leaf pattern circulation zones (Figure 3.2). The intensity of the circulations was higher at higher temperature due to the decrease of the viscosity of the fluid. Negative applied voltage induced higher intensity circulations compared to positive ones which was attributed to higher electric currents. Fujino et al. (1989), investigated the electroconvection phenomena in parallel plate heat exchanger. The effect of heat flux magnitude and voltage polarity on heat transfer enhancement was studied using R-113 as working fluid. The heat flux was applied at the high voltage side always and the polarity effect was also studied. In Figure 3.3 part (i) it is shown that, longitudinal rolls developed from the positive side electrode and proceeding with time to the other electrode. It was found that changing the heat flux magnitude, i.e. changing temperature gradient did not have an effect on the heat transfer coefficient (Figure 3.4) which means that the nature of charges in this case was not based on the change in conductivity due to the applied temperature gradient.

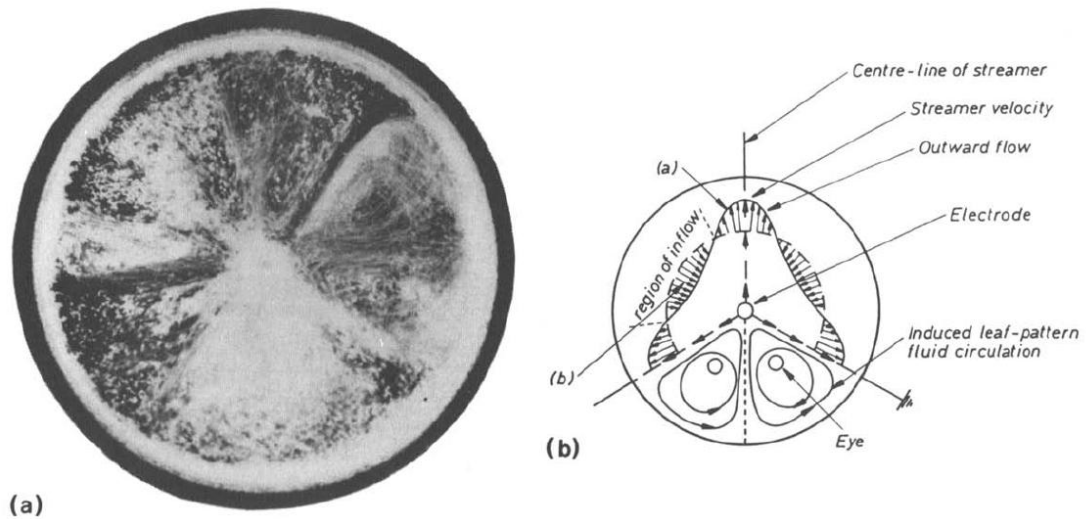


Figure 3.2 (a) Streak flow visualization. (b) Schematic representation for the leaf pattern induced by electroconvection in an annular cross section. (Fernández, et al., 1987)

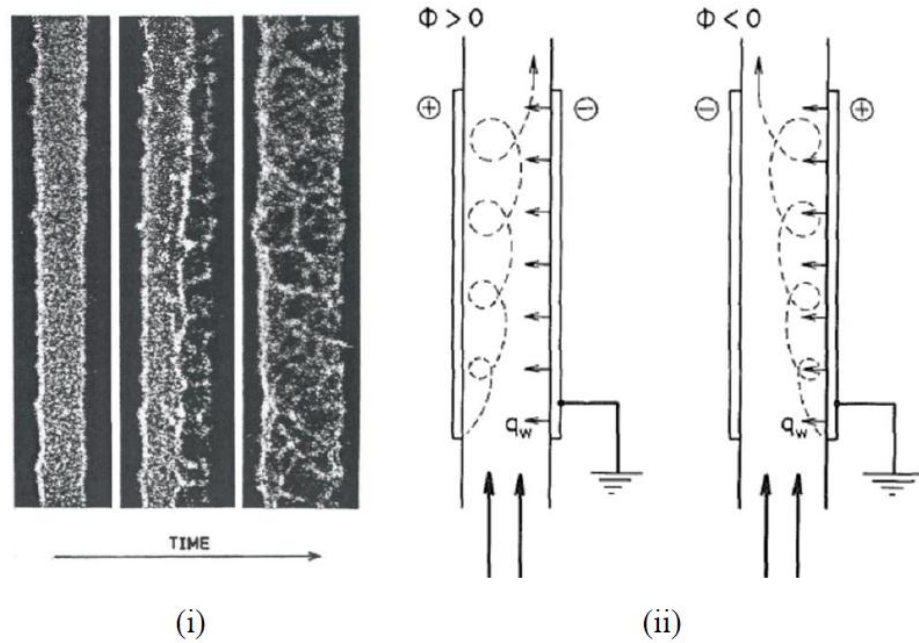


Figure 3.3 (i) Shadowgraph images with time interval 0.2 sec. (ii) Schematic illustration of electrically induced secondary flow. (Fujino, et al., 1989)

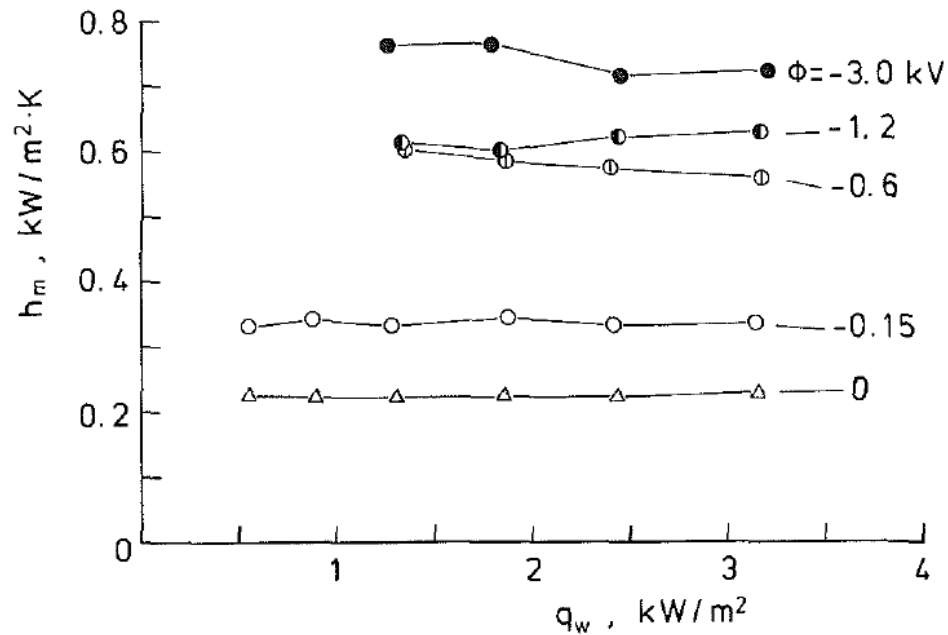


Figure 3.4 Average heat transfer coefficient vs. heat flux at the surface of the heating electrode. (Fujino, et al., 1989)

The nature of charges was explained to be due to charge injection of negative ions from the negative electrode. The authors explained that the longitudinal rolls were developed at the side opposite to the injecting electrode due to the shear caused by the migration of the charges from the negative electrode to the positive one. They found that the negative polarity electrodes cause a higher heat enhancement than using a high voltage positive polarity electrodes which agrees with (Fernández, et al., 1987).

The effect of EHD on natural convection in open vertical channels heated from one side was investigated numerically by Kasayapanand (2008). High voltage was supplied through small diameter wire electrodes placed across the symmetry line of the vertical channel while both vertical walls of the channel are electrically grounded. The characteristics of the flow and heat transfer were studied under the effect of Rayleigh

number, supplied voltage, number of electrodes, channel aspect ratio and the electrode arrangement. The numerical results were compared with the experimental results for a configuration of 5 electrodes and showed a good agreement within range of 10% (Figure 3.5).

It was found that the heat transfer enhancement caused by EHD decreases by the increase of the Rayleigh number and the decrease of the applied voltage (see Figure 3.5). The number of electrodes was varied from 1 to 33 electrode and it was found that the maximum heat transfer enhancement happened within range of 5 to 9 electrodes (Figure 3.6). Increasing the number of electrodes more than 9, decreased the heat transfer enhancement due to combination of the small vortices to form a larger vortices. In the range of 25 to 33 electrodes, heat transfer enhancement started to increase again due to the increased electric field intensity caused by the increase of the number of electrodes.

Paschkewitz, et al. (2000) investigated the effect of fluid properties on the heat transfer enhancement caused by EHD. Three cooling oils were examined with widely varying physical properties. The cooling oils that were used are: Polyalphaolefin (PAO), ECO-C which is a bio-degradable transformer oil and Beta fluid which is used as an electrical cable oil, their physical properties are presented in Table 3.1. Paschkewitz, et al. (2000) found that fluids with lower viscosity and electrical conductivity gave the greatest heat enhancement corresponding to a certain electrical power. In Figure 3.7, the required electrical power is presented versus Nusselt number for the three different fluids for a low range of Reynolds number. The results showed a negligible heat transfer enhancement for electrical power less than 10^{-6} W for the three different fluids, indicating that fluid

properties has almost no effect at this stage. A heat transfer enhancement up to 2 times was achieved with electric power of $5 \cdot 10^{-5}$ W for ECO-C fluid and $8 \cdot 10^{-4}$ W for PAO fluid. This was attributed to the higher viscosity of PAO which dissipates the EHD motion requiring higher charge injection to reach the same enhancement as the ECO-C fluid.

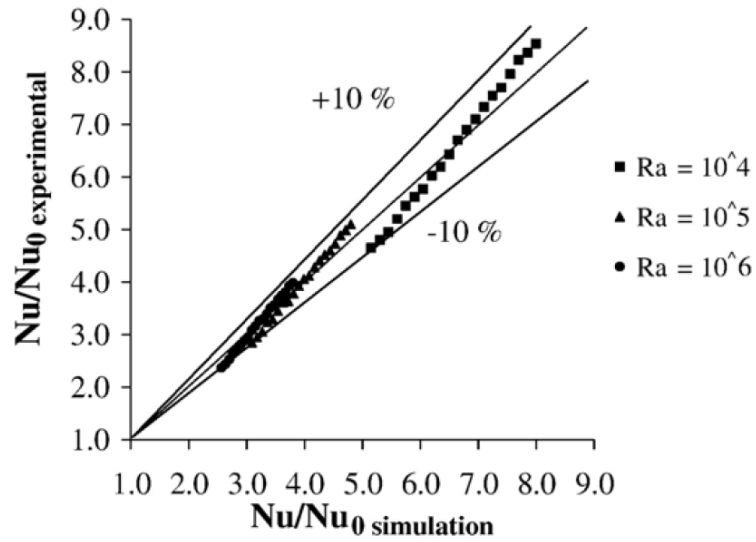


Figure 3.5 Comparison between numerical and experimental heat enhancement for $V=7.5$ to 17.5 kV and 5 electrodes under different Rayleigh numbers. (Kasayapanand, 2008)

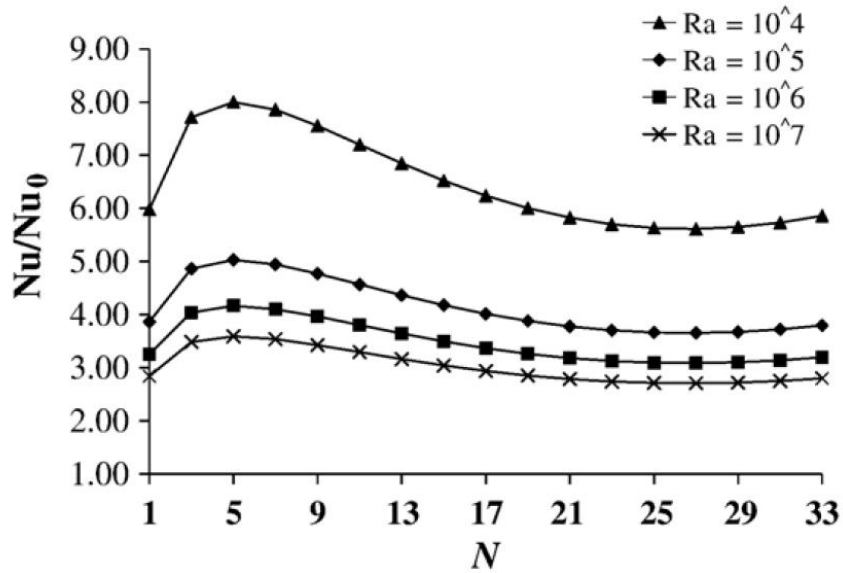


Figure 3.6 Heat transfer enhancement with the number of electrodes. (Kasayapanand, 2008)

Table 3.1 Working fluid physical properties. (Paschkewitz, et al., 2000)

Working fluid	PAO	ECO-C	Beta
<i>Composition (% wt)</i>			
Paraffinic hydrocarbon	99.5	>90	>99
Hindered phenol antioxidants	0.5	< 10	<1
<i>Physical Properties</i>			
Density at 20 °C, g/cc	0.79	0.85	0.86
Viscosity at 40 °C, mm ² /s	6.6	3.5	108
Electrical conductivity, S/m	2.7×10^{-10}	4.76×10^{-13}	6.25×10^{-13}
Thermal conductivity, W/m °C	0.147	0.134	0.125
Dielectric constant	2.1	2.2	2.3
Ion mobility, m ² /Vs	3.33×10^{-9}	6.72×10^{-9}	2.15×10^{-10}
Heat capacity, J/kg °C	2050	547	670
Charge relaxation time ε/σ , s	6.9	4090	3256
Prandtl number	72	12.1	830

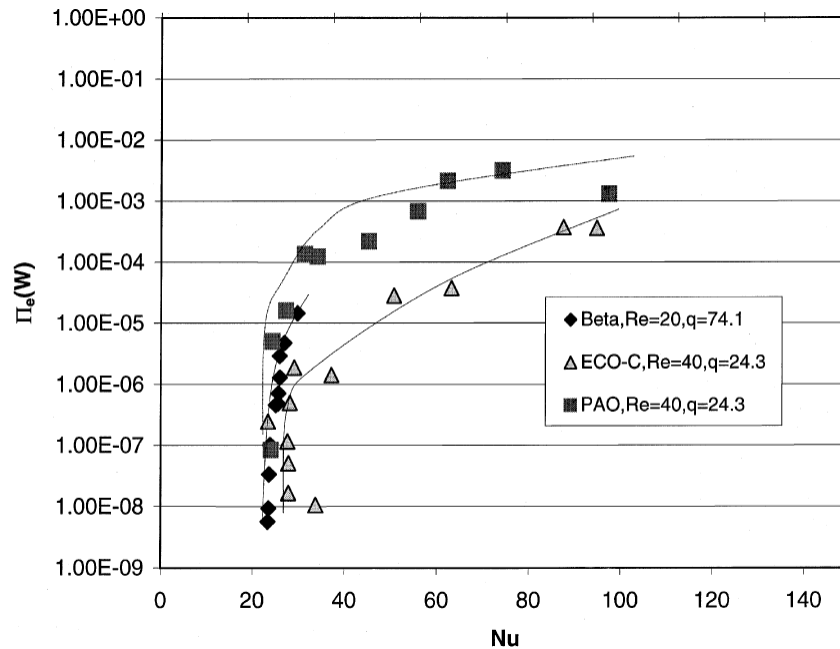


Figure 3.7 Electrical power vs. Nusselt number. (Paschkewitz, et al., 2000)

3.4. Multiphase EHD Heat Transfer Enhancement

The EHD effect on heat transfer enhancement for multiphase systems has been studied extensively for liquid-vapor systems in boiling and condensation heat transfer. It was found that polarization forces play an important role in redistribution of the flow patterns which considerably change the heat transfer characteristics of such systems.

In the scope of this thesis, the EHD effect on solid-liquid multiphase systems is the primary concern. However, the previous work done in this area was very limited and mainly focused on controlling or reducing natural convection during material solidification or enhancing the melting process using Electro Magneto hydrodynamics in low gravity environments. The closest study to the scope of this thesis is (Dellorusso, 1997) which was designing an EHD heat exchanger for a thermal storage systems using paraffin as the PCM.

The EHD effect on the instability of the interface for liquid-vapor systems and heat transfer enhancements caused by these interfacial forces will be discussed in this section. Previous work done for EHD effect on solid-liquid multiphase systems and the EHD forces on suspends in a dielectric fluid will be discussed in this section to serve as a review for EHD effect in multiphase systems.

3.4.1. EHD Interfacial Forces

Applying high voltage on two phase systems can cause two types of forces: interfacial forces at the interface separating the two phases and bulk body forces at each phase separately. In case of two phase systems the second and third of the EHD body forces

term which are the dielectrophoretic and electrostrictive component becomes significant because of the $\nabla \varepsilon$ term at the interface. In order to quantify the value of this force analytically, an infinitesimal volume of the interface was assumed by Stratton (1941) and the limit of this volume as it approaches zero was formulated to convert this force from a body force to an interfacial force, the formula as derived by (Stratton, 1941) and (Scaife, 1989) is

$$t = \frac{\epsilon_0}{6} \left\{ \frac{1}{\epsilon_2} [\epsilon_1^2 \epsilon_2^2 + 4\epsilon_1^2 \epsilon_2 - 6\epsilon_1 \epsilon_2^2 - 3\epsilon_1^2 + 2\epsilon_1 + 2] E_{n1}^2 + [\epsilon_2(\epsilon_2 - 2) - \epsilon_1(\epsilon_1 - 2)] E_{t1}^2 \right\} n_2 \quad (3.13.)$$

This interfacial force cause interface instabilities, and can cause the phase of higher permittivity to move to region of high electric field. This phenomena was observed in liquid-vapor systems and known “Liquid Extraction “and was reported by several researcher as (Melcher, 1963), (Yabe, 1987a), (Singh, 1995), (Cotton, et al., 2005), (Sadek, et al., 2010), (Ng, et al., 2011) and (Nangle Smith, 2012)

3.4.2. Boiling and Condensation under EHD forces

An extensive research was conducted on the EHD effect on heat transfer enhancement of in tube convective boiling for different refrigerants (Yabe, et al., 1992), (Singh, et al., 1994), (Salehi, et al., 1997) and (Cotton, 2000). It was generally found that increasing the voltage will increase the level of EHD enhancement and the induced mixing. In general increasing the voltage, increased pressure drop due to the EHD induced mixing. The heat transfer enhancement and pressure drop are attributed to the two phase redistribution

caused by the interfacial forces. In some cases, EHD forces caused degradation in heat transfer during boiling due to the possible dry out caused by the flow redistribution (Norris, et al., 1999). The studies on convective evaporation showed an increase of the heat transfer by two folds as (Yabe, et al., 1992), (Norris, et al., 1999), (Cotton 2000) and sometimes up to ten folds (Salehi, et al., 1997). Cotton, et al. (2005) found that the EHD level of enhancement increases with the decrease of the mass flux of refrigerant and developed an EHD flow pattern map. Nangle Smith (2012) investigated the effect of polarity for in tube convective boiling and it was found that negative polarities showed a better enhancement as it offers more wetted area over the heat transfer surface caused by repulsion of the liquid away of the electrode after being extracted.

Condensation over horizontal tubes under the effect of applied DC voltage was studied by (Cheung et al 1999) for external EHD condensation and by (Cotton 2009), (Sadek 2009) and (Ng 2010) for internal EHD condensation of R-134a refrigerant. Gidwani, et al. (2002) studied the EHD effect on condensation over complex heat transfer surfaces as corrugated tubes and investigated the effect of fluid properties. In general an increase of the applied voltage increased both, heat transfer and pressure drop. The EHD mechanism for condensation heat transfer enhancement was attributed to the removal of the condensate from the heat transfer surface by liquid extraction which decreased the thermal resistance at the heat transfer surface. Gidwani, et al. (2002), showed that a heat transfer enhancement up to 18.8 fold for in tube condensation of R-404a can be achieved, however the corresponding pressure drop penalty was 11.8 fold. He showed also that the heat flux value had a negligible effect for this type of configuration. The increase in

pressure drop is mainly caused by the destabilization of the hydrodynamic boundary layer and the momentum transfer between the two phase flow and the center electrode. (Sadek 2009) observed the formation of twisted liquid cones at the moment of applying high voltage which diminishes as the system gets to steady state. Ng, et al. (2011) studied the ability to sustain this EHD transient behavior and liquid cones by trying to apply different AC waveforms with different frequencies and duty cycle, however it was found that sustaining this flow regimes did not offer higher enhancement. The investigation was further proceeded by the effect of polarity and it was found that the positive polarity offered a higher enhancement over the negative due to the uptake of the fluid into the core regions.

3.4.3. Melting and Solidification under EHD forces

Very limited research on the application of EHD on melting and solidification was carried out by previous researchers. Most of the work in this field was carried numerically and was related to the contribution of EHD forces in reducing and controlling the natural convection during solidification or enhancing the natural convection in low gravity environments during the melting process. No previous work studied the interfacial effect of EHD forces on the solid-liquid interface.

Dulikravich, et al. (1994) studied numerically a solidification problem of Gallium Arsenide, where the solidification was initiated from the top wall. The EHD effect was studied in full and low gravity (1 %) environments and under parallel and perpendicular

electric field to the direction of solidification. In order to simplify the problem (Dulikravich, et al., 1994) solved the problem as a steady state. The problem was approached as a solidification problem with a given temperature difference between the top and bottom wall and the final amount of the solidified material at each case and the temperature gradients were evaluated and was used as a criteria to estimate the EHD effect. This makes the problem unrealistic as for solidification it is usually only one fixed temperature which resembles the cooling fluid which is always at a temperature less than the melting temperature of the PCM and there is no existence for a constant high temperature which provides heat input to the system. In the simulated problem as the amount of solidified material decreases, this means higher temperature gradients in the solid phase which indicates a higher heat transfer from the bottom wall towards the top cooling wall.

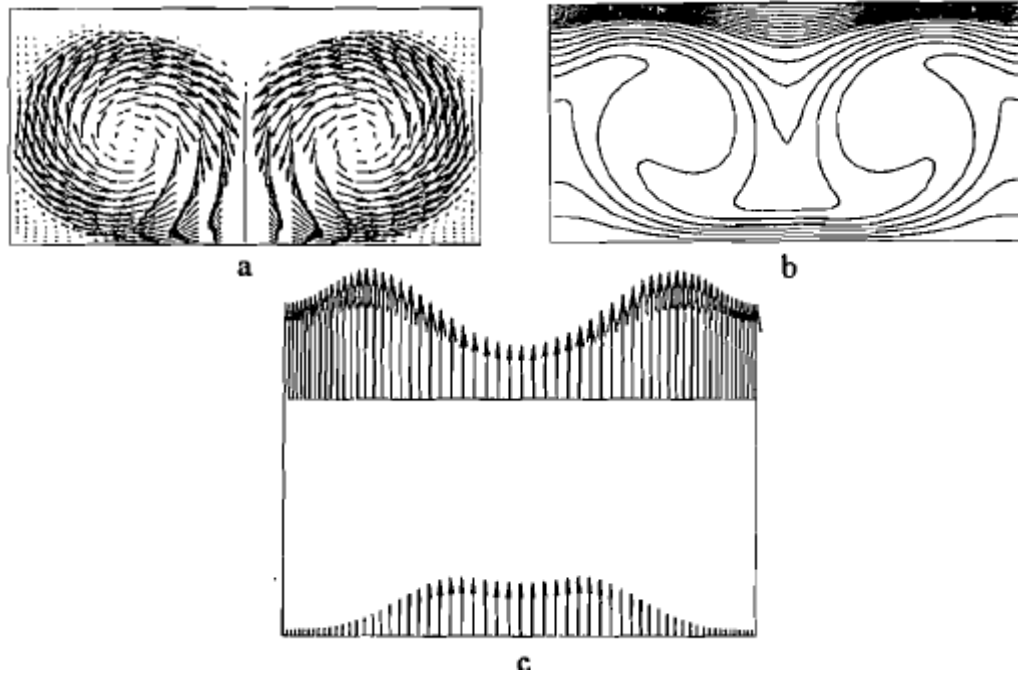


Figure 3.8 (a) Velocity vector field. (b) Isotherms (c) Normal temperature gradients at the top and bottom wall/ 0kV and full gravity case. (Dulikravich, et al., 1994)

Figure 3.8 shows the velocity vector field, isotherms contours and normal temperature gradient for the top and bottom wall for a 0 kV case under full gravity conditions. The formation of two strong counteracting thermoconvective vortices is observed due to natural convection. These vortices increased the convective heat transfer and caused non-uniform temperature gradients at the top and bottom wall. In case of 5 kV applied voltage, there was a negligible difference in the velocity field and the amount of solidified material suggested that the EHD forces did not affect the thermal buoyancy forces and a higher electric field is required.

In case of low gravity environment, the EHD effect was notable as the buoyancy forces decreased significantly and the system only needed to overcome the viscous forces. It was

concluded that EHD is more effective in enhancing the heat transfer process in reduced gravity environment under low Rayleigh number.

Colaço, et al. (2004) upgraded the steady state model developed by Dulikravich, et al. (1994) to a time accurate model. The effect of using side wall electrodes with time varying potentials in order to control and reduce natural convection during solidification of Gallium Arsenide was investigated.

The EHD effect was found to be more effective in low Rayleigh number cases, however it was found that when trying to change the potential across the electrode that produced a very unstable velocity contours which were not observed in case of constant potential electrode.

The closest study to the current investigation is (Dellorusso, 1997). Dellorusso studied the effect of EHD on heat transfer enhancement of a latent heat storage heat exchanger. The author investigated the EHD enhancement on the heat transfer fluid side (air) and the PCM side separately and simultaneously. A paraffin wax of melting temperature 55 °C was used as the PCM and was stored inside a fin array configuration made of aluminum. The details of the geometry of the thermal storage cell and the detailed section view of internal fin dimensions are presented in Figure 3.9. The heat transfer fluid flows through the side channels while the PCM in the central channel is being melted/solidified from both sides. Figure 3.10 represents the electrical configuration used for PCM, heat transfer fluid and simultaneous enhancement. Because the scope of this project is dealing with EHD role in enhancing the phase change process, only the EHD effect on the PCM side will be discussed.

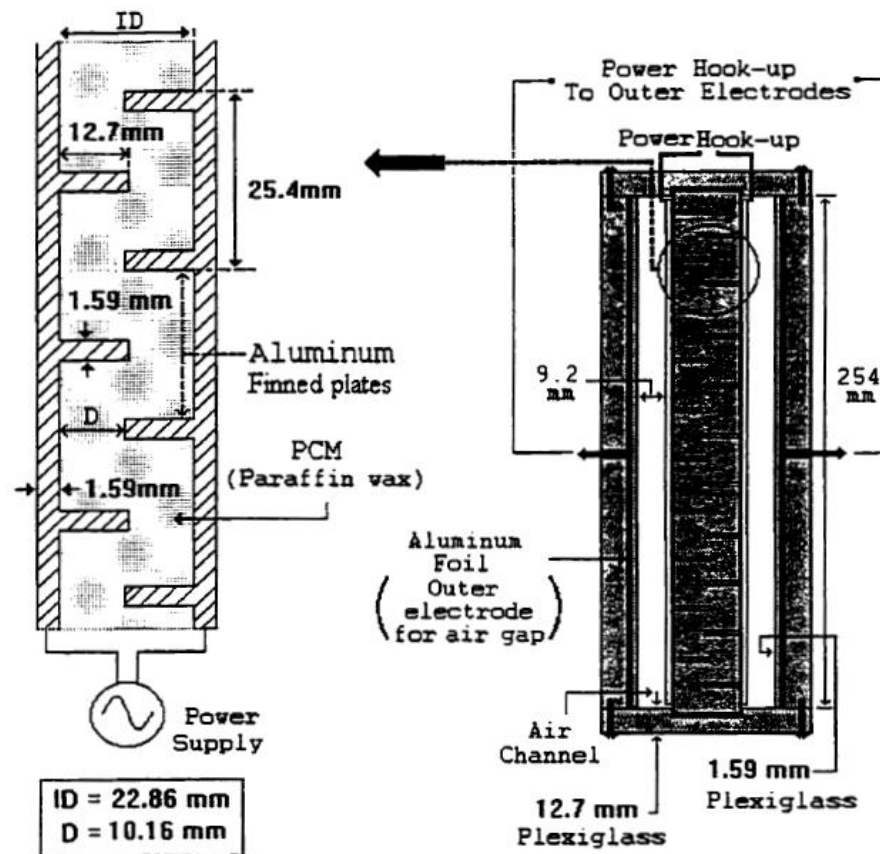


Figure 3.9 Cross sectional view of the thermal storage cell and a detailed section view for internal fin dimensions. (Dellorusso, 1997)

For the PCM side, an applied voltage of 15 kV (DC and AC) was used for EHD testing. It was stated that, for the solidification, EHD had a negative effect compared to no EHD experiments. The author suggested that this negative effect is because the main mode of heat transfer in solidification is conduction and EHD may have caused disturbance in the liquid PCM which decreased crystal growth and nucleation sites. The power consumed in solidification experiment for 15 kV AC case was within range of 3-5 W while for the DC case was from 0.5 to 1 W. The normalized average heat transfer coefficients for the solidification cycle under different Reynolds number for the heat transfer fluid side (air) are plotted in Figure 3.11.

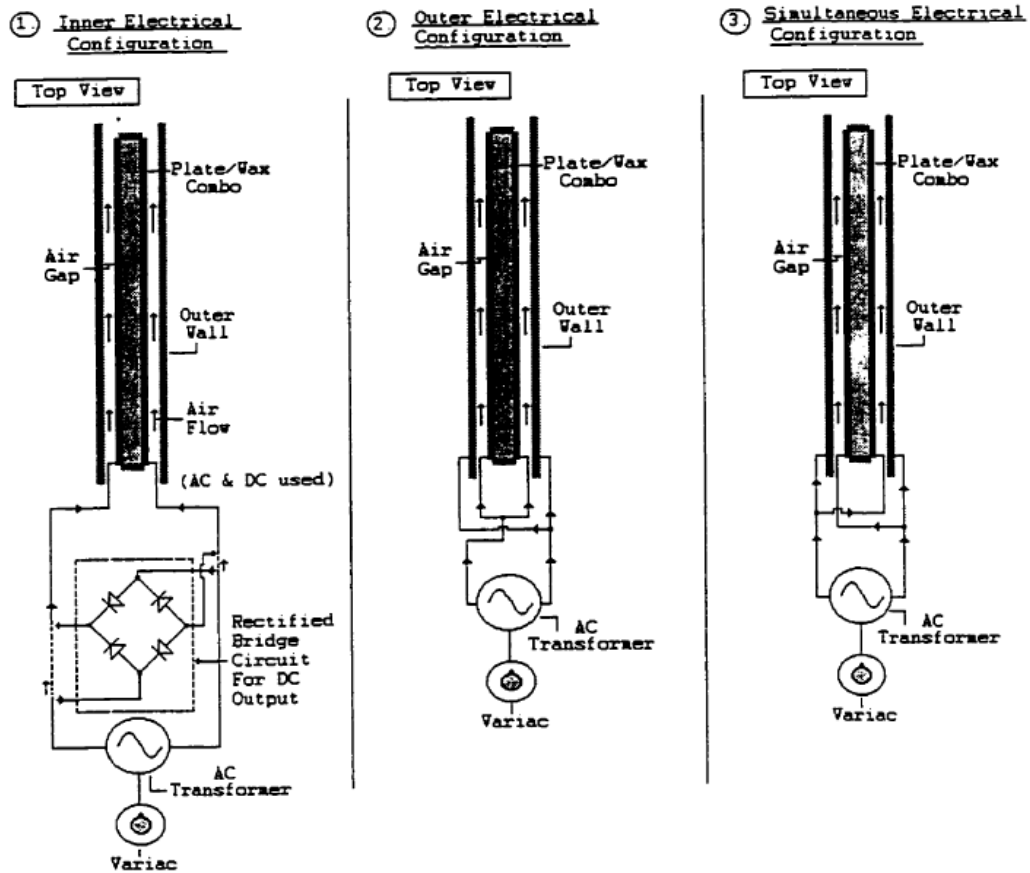


Figure 3.10 Electrical configurations for EHD enhancement. (Dellorusso, 1997)

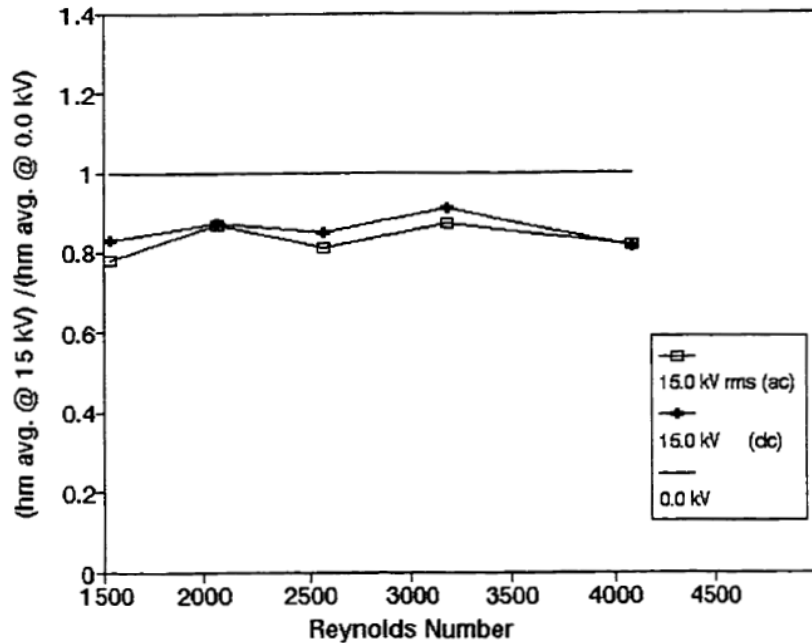


Figure 3.11 Normalized average heat transfer coefficient for solidification cycles under different Reynolds number of the air side. (Dellorusso, 1997)

It was clear that Reynolds number of the heat transfer fluid had almost no effect as the PCM was always the limiting heat transfer side due to its low thermal conductivity. A decrease of 20 % of the normalized average heat transfer due to using EHD was noticed in solidification cycles. It was observed that the normalized averaged heat transfer coefficients for the AC electric fields are $\approx 5\%$ less than that for DC electric fields. The author did not discuss the possible reasons for that.

In case of melting cycles there were no clear trends for EHD enhancement in the melting process, sometimes it appears that it enhances and other times a negative effect was observed. The power consumption for the AC and DC was the same as the solidification cycles were AC consumed more power, but there was no clear trend in the amount of enhancement. Figure 3.12 represents the average heat absorption rate for melting cycles under different Reynolds number for the heat transfer fluid. It was observed that almost all the cases are alike and there is no significant effect of using EHD in melting. The author attributed the non-effectiveness of EHD during melting to the cell design. The author suggested that the cell design did not promote melting by convection until late times of melting which was not sufficient for EHD to enhance the overall progress. The author also added that using such complex design was not a good choice, as a better electrode configuration and a simpler geometry could be more effective in designing a cell which could enhance the natural convection within the molten PCM. Using sharp edged fins leads to increasing the electric field strength significantly around the edges leading to a complicated EHD behavior due to the localized electric field strengths. A simpler geometry was suggested in order to study the effect of EHD on melting.

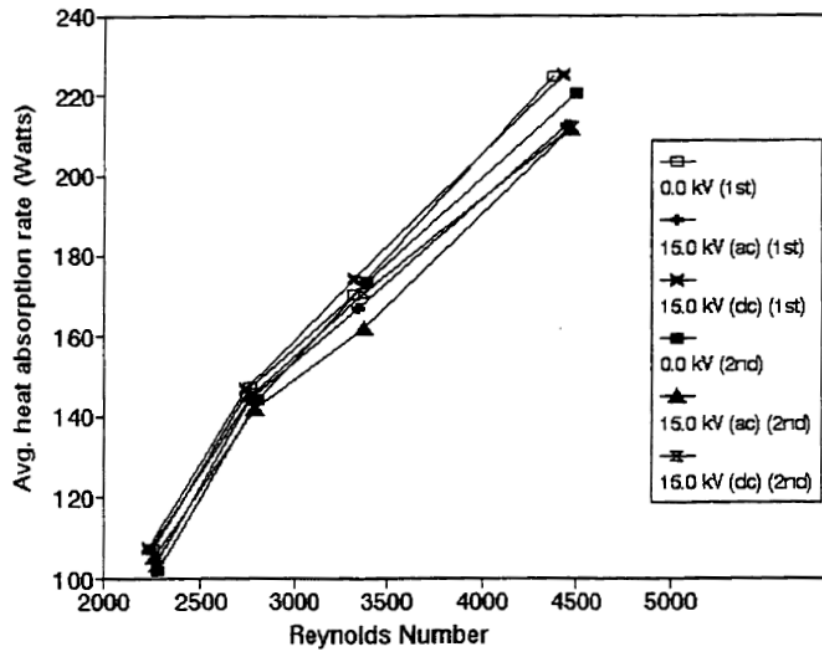


Figure 3.12 Average heat absorption rate for melting cycles under different Reynold's number of the air side. (Dellorusso, 1997)

4. Experimental Facility

An experimental facility was designed and fabricated to study the effect of EHD on the melting process of a paraffin wax latent heat thermal storage cell. The main objective was to characterize the thermal performance enhancement caused by EHD using a simple geometry capable of tracking the melt front visually without using thermocouples inside the cell which may disturb the electric field distribution. In this chapter the details of the experimental facility, the test section and the experimental procedures are discussed.

4.1. Test Facility

A schematic diagram for the experimental facility is shown in Figure 4.1. The PCM material used is fully refined paraffin wax- IGI 1245A (details of the thermo physical and electrical properties can be found in Appendix (A)). The PCM (paraffin wax) is enclosed in a test section made of transparent acrylic rectangular enclosure of 6 mm thickness to allow for optical visualization inside the cell. The details of the test section are shown in Figure 4.2 and Figure 4.3, where main inner dimensions enclosing the PCM are 126 mm length, 36 mm height and 50.8 mm depth. The PCM material fills only up to the 36 mm height where the rest of the section was designed to act as a riser to adapt for the paraffin

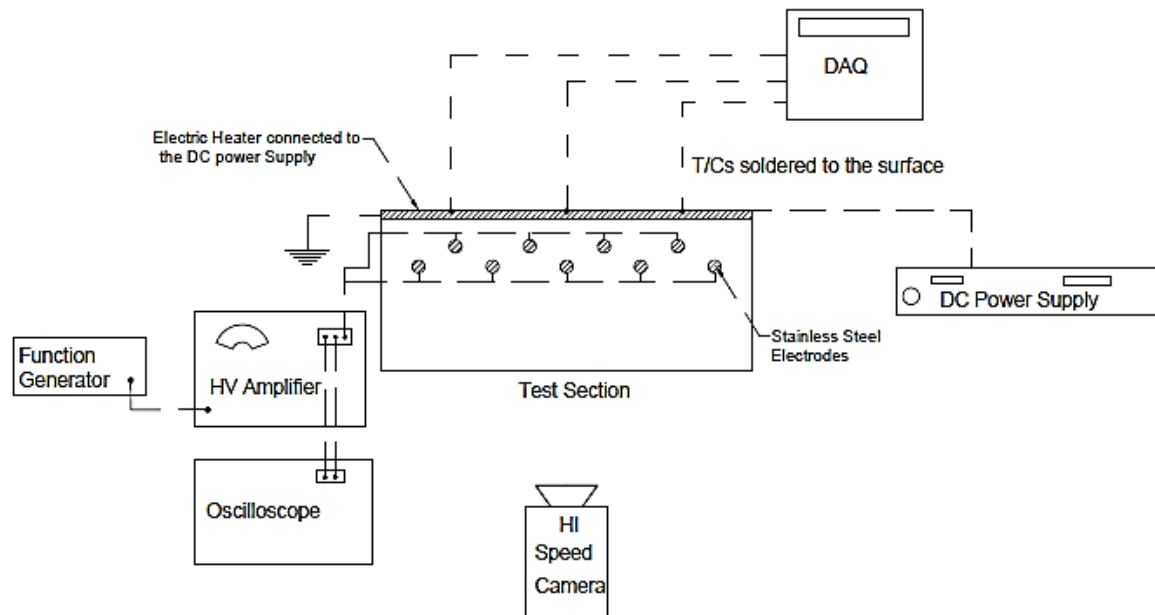


Figure 4.1 Schematic of experimental test facility

wax expansion during melting and as a continuous hot supply of PCM during solidification. An Omega Kapton insulated flexible electric heater (KH-204/5-P) of maximum power density $5W/in^2$ was attached to 0.8 mm thick copper sheet of dimensions 106 mm length and 62.8 mm width. The assembly was mounted on the top of the test section to serve as the heating surface during melting. The electric heater is connected to a DC power supply (Agilent 6655 A – maximum power 480 W).

The copper was chosen for its high thermal conductivity to assure uniform temperature and heat flux distribution across the entire surface area. It was chosen relatively thin to assure a fast thermal response of the copper by minimizing its thermal capacitance.

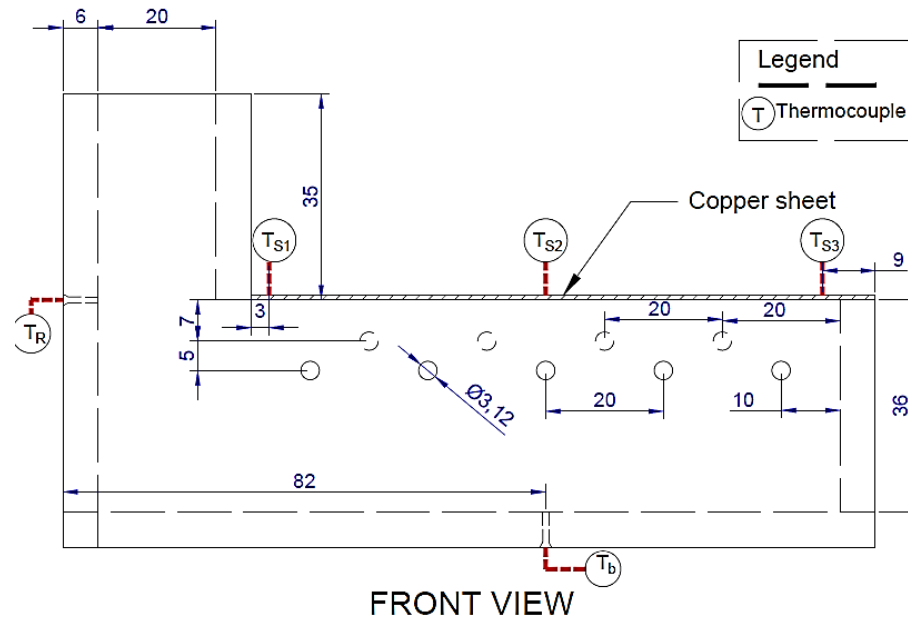


Figure 4.2 Front view for the experimental test section

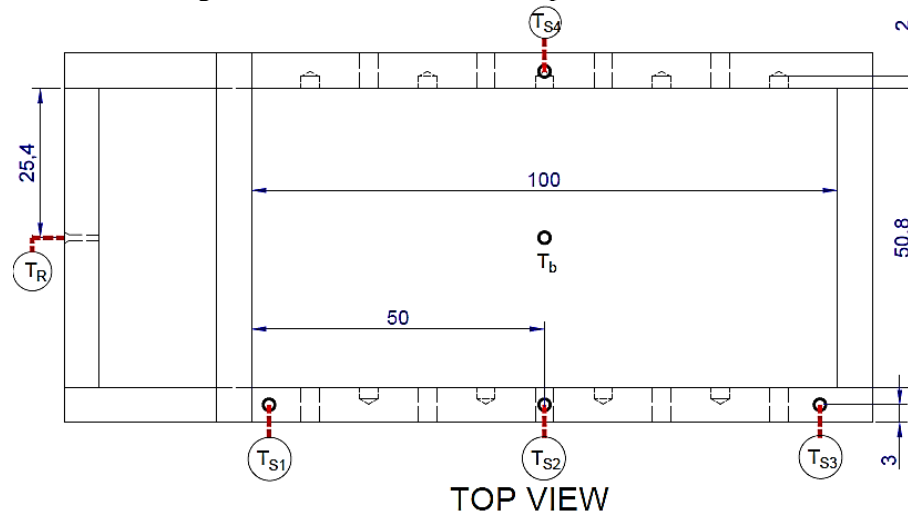


Figure 4.3 Top view for the experimental test section

The target is to establish a relatively fast responding system to capture temperature variations of the molten PCM inside the cell. The surface temperature was measured by type-T thermocouples (0.5 mm sheath diameter) soldered to the edges of the copper sheet as shown in Figure 4.3 and Figure 4.4. Three thermocouples (T_{S1} , T_{S2} and T_{S3}) were

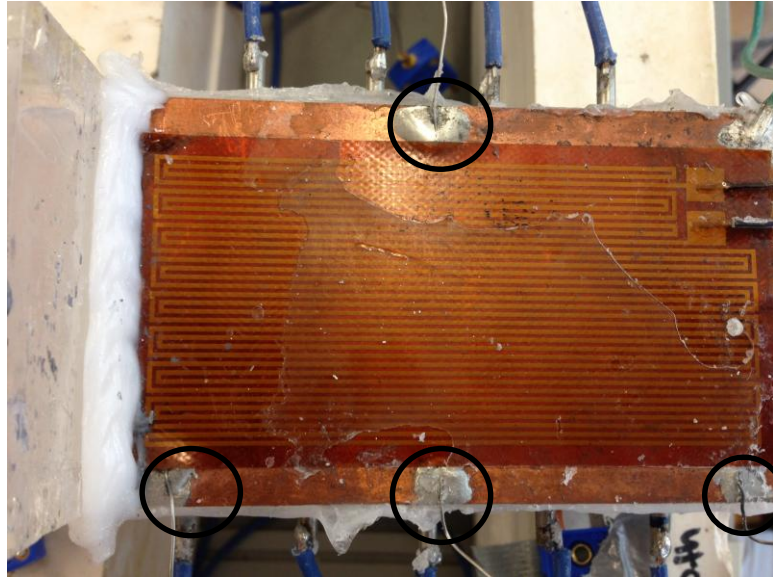


Figure 4.4 Thermocouple locations on the copper sheet

soldered on one side of the copper sheet to get the average temperature and one thermocouple (T_{S4}) at the other side to check for the symmetry of the experimental setup. Two type-T thermocouples of 1 mm sheath diameter were used for energy balance calculation (refer to Chapter 5), where one was fixed at the bottom of the cell (T_b) to estimate the rise in temperature of the solid PCM and the other at one side of the riser (T_R) to estimate the riser temperature (Figure 4.2). The thermocouples reading were obtained by a 16 channel data acquisition thermocouple module (NI 9213) mounted on a DAQ chassis (NI cDAQ-9174). The real time temperature readings were monitored by LabVIEW software and were recorded with 1 sec intervals. Directional downwards melting was selected to achieve a thermally stratified molten phase and prevents natural convection effects. The target was trying to simplify the phenomena involved in the melting process and to limit it to heat conduction only in order to understand the

mechanism of EHD alone. A 20 mm thick thermal insulation of type IIG Super Firetemp L with a thermal conductivity of $k= 0.078 W/m K$ was used to thermally insulate the cell from the bottom and the sides, only leaving a 20 mm section in one side of the acrylic for visualization. A unidirectional heat transfer to the paraffin wax was approximately achieved by insulating the top of the heater with a similar 70 mm thick insulation. The high voltage potential was applied to the system through 9 stainless steel rod electrodes of diameter 3.175 mm and length 70 mm. The 9 electrodes were divided into two horizontal rows, the upper level row located 7 mm from the copper sheet had 4 electrodes with a 20 mm spacing. The lower level row located 12 mm from the copper sheet had 5 electrodes with a 20 mm spacing. Each level of electrodes was penetrating from a different side of the cell than the other to be able to reach a higher voltage inside the cell breaking down between the electrodes. The end of each electrode was resting on a 2 mm groove on the internal side of the acrylic wall (Figure 4.5). The groove acted as a fixture for the electrode and prevented the end effects to interfere with the electric field distribution in the cell. The electrodes are connected together to a high voltage amplifier (Trek Model 20/20C) and the input voltage signal was supplied. Tektronix AFG3021B function generator is connected to the low voltage side of the amplifier. The ground side is the copper sheet and it is connected to the high voltage amplifier ground. Both the current and the voltage from the high voltage amplifier were monitored by an Agilent oscilloscope (Model 54621A).

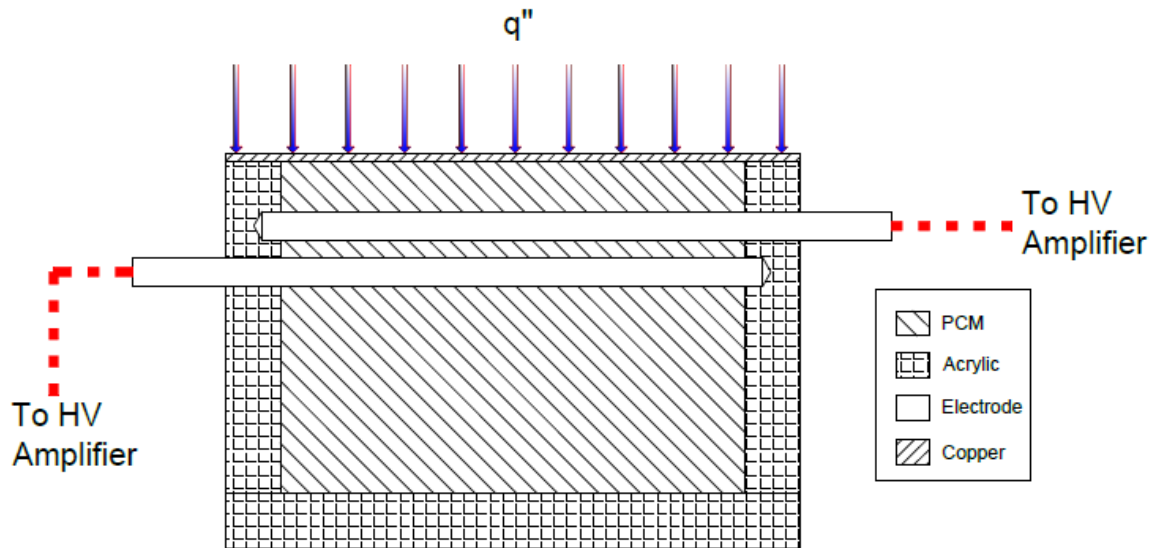


Figure 4.5 Details of electrodes configuration

Fastec Troubleshooter high speed camera that was used for estimating the melt front position and acquiring high speed images at the solid-liquid interface to help understanding the physics involved during melting when the high voltage was applied.

- **Melt Thickness Measurement**

The liquid paraffin wax is transparent while the solid paraffin wax had a white opaque color and the contrast was used in the melt front tracking, where the amount of molten paraffin can be visually identified. The melt front location was tracked visually by using a high speed camera. Images were processed using commercial Digimizer software for image processing to detect the interface location. The scale of each image was determined

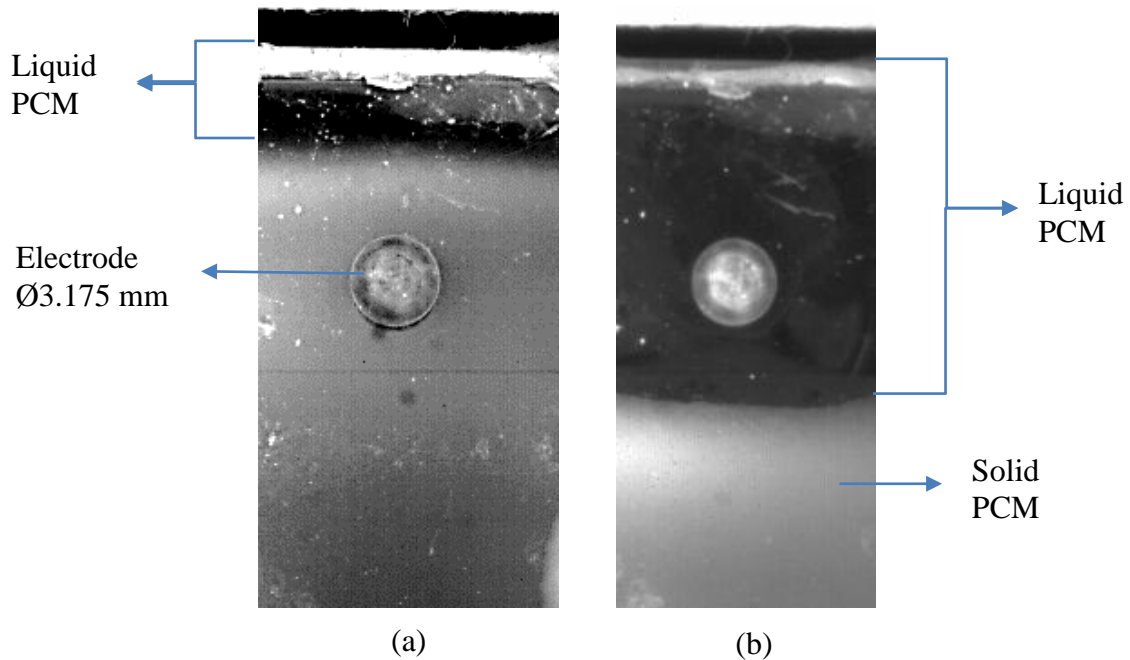


Figure 4.6 Melt front location images

by the size of the electrode (3.156 mm diameter) and the distance between the centre of the electrode and the bottom of the heater (7 mm). Figure 4.6 shows an example for the images used to calculate the melt front location at each time, with liquid levels above the first row of electrodes in Figure 4.6a and below the first row of electrodes as in Figure 4.6b.

4.2. Experimental Procedures

The experimental procedures are divided into 3 main sections. The first section is focused on the preparation of the PCM for testing. The second section is showing how to start the experiments and the initial conditions. The third section is describing the solidification process of the PCM for starting a new experiment.

4.2.1. Preparation

- 1- The PCM is allowed to go through at least 10 cycles of melting and solidification inside a furnace before being used in the experiments to assure chemical stability.
- 2- Place the experimental test section and 500 gm. of the PCM inside a Pyrex container with a pour spout in the furnace and set up the temperature to 70 ° C to assure that it is above the melting point of the PCM and leave until the PCM inside the Pyrex container completely melts.
- 3- Pour the molten PCM slowly to avoid formation of bubbles into the experimental test section through the riser until the experimental test section is half full with PCM and then place it inside the furnace and let it cool gradually until it completely solidifies.
- 4- After the PCM solidifies inside the experimental test section, connect the electric heater mounted on the copper sheet to the DC power supply and reheat the cell until the surface temperature reaches 80 ° C , at the same time an electric tape heater is wrapped around the riser to make sure it is warm enough above the melting point.
- 5- Pour the rest of the PCM into the experimental section through the riser while leaving both heaters operating.
- 6- Gradually decrease the power of both heaters allowing the PCM to solidify slowly and at the same time tilting the whole experimental section by 10 ° C to allow any bubbles to escape through the riser.

- 7- Leave the experimental test section for 2 days before using it for experiments to assure a uniform temperature inside the cell allowing for a uniform controlled directional solidification from bottom of the test section.

4.2.2. Starting the experiment

- 1- Install the thermal insulation around the cell, leaving only the 20 mm window for melt front tracking covered with a piece of fiber glass that can be easily removed during experiments for taking images.
- 2- Make sure that the ambient temperature range is between 22 to 24 ° C for consistency between different experiments.
- 3- Check the thermocouples readings to be almost the same as the ambient temperature to make sure that the PCM temperature is uniform.
- 4- For the EHD experiments, disconnect the thermocouples that are inside the PCM which are the bottom thermocouple and the riser one to reduce disturbing the electric field inside the cell., for a 0 KV (No EHD) they can be left connected to the DAQ.
- 5- For the EHD experiments set up the HV to the desired level through the function generator before starting the experiment.
- 6- Connect the electric heater to the DC power supply and set it to the voltage corresponding to the desired power.

- 7- Turn on the DC power supply and start recording the thermocouples reading through LabVIEW.
- 8- When the temperature of the copper sheet goes above 63 ° C (melting point) start taking images for the melt front location approximately each 10 minutes by removing the fiberglass insulation from the 20 mm section and re-installing between visualization readings.

4.2.3. Solidification

- 1- After finishing the experiment, the thermal insulation around the riser is taken off and an electric tape heater is wrapped around the riser.
- 2- The electric tape heater is connected to a 110 volt VARIAC and set up to 70 % of the full scale.
- 3- Remove the thermal insulation from the bottom and allow the test section to cool down naturally from the bottom surface of the acrylic.
- 4- Gradually decrease the power of both the main and riser heater over a 4 hours period to assure a slow uniform solidification and a hot riser all the time to compensate for the volumetric contraction during solidification.
- 5- Disconnect both heaters when the thermocouples at the copper sheet read 50 ° C (below the lower melting point) and leave the test section for at least 36 hours to cool down and assure a uniform temperature inside equals to the ambient temperature before starting a new experiment.

4.3. Experimentally Measured Parameters

The experimentally measured parameters were used to evaluate the thermal performance for a latent heat thermal storage cell. A list for the measured parameters are shown in Table 4.1.

Table 4.1 The measured parameters

Symbol	Measured Parameter
T_{S1}	Copper sheet surface temperature, location 1
T_{S2}	Copper sheet surface temperature, location 2
T_{S3}	Copper sheet surface temperature, location 3
T_{S4}	Copper sheet surface temperature, location 4
T_b	PCM temperature measured at the bottom of the test section
T_R	PCM temperature measured at the riser
S	Melt thickness
V_H	Electric heater voltage
I_H	Electric heater current
V_{EHD}	Voltage applied to the electrodes
I_{EHD}	Electric current passing through the electrodes

5. Thermal Characterization of Storage System

Thermal characterization for the tested latent heat storage cell including system energy balance, data reduction methods and the uncertainty in the measured and calculated parameters is discussed in this section. The cell energy balance was evaluated for the 0 kV, 14.2 W input power case to estimate the accuracy of the experimental results and to quantify the amount of heat losses to the surroundings in each experiment.

An analytical model was used to assess the cumulative energy stored in the latent heat thermal storage cell and comparing it with the heat input from the electrical heaters.

The results of the analytical model were compared with a CFD model calculated by the commercial software ANSYS FLUENT and then heat losses to surroundings for the different experimental cases were assessed.

5.1. Energy Balance Analytical Model

The thermal energy stored in the experimental test section can be divided into 7 different contributing components:

- a. Sensible heat stored in the molten PCM ($Q_{sensible-L}$)
- b. Latent heat absorbed by the molten PCM ($Q_{Latent-S}$)

- c. Sensible heat stored in the solid PCM ($Q_{sensible-s}$)
- d. Sensible and latent stored in the mushy zone (Q_{mushy})
- e. Sensible heat stored in the acrylic side walls ($Q_{acrylic\ walls}$)
- f. Sensible heat stored in the copper sheet (Q_{copper})
- g. Sensible heat stored in the thermal insulation ($Q_{insulation}$)

The seven different components will be estimated analytically by using the three temperature readings acquired by the thermocouples mounted in the cell and the melt front location at any given time and will be compared with the total energy input to the system at a given time. The total energy input to the system is equal to the power of the electric heater as given by equation (5.1.)

$$Q(t)_{I/P} = V \times I \times t \quad (5.1.)$$

and the energy balance equation is given by equation (5.2.)

$$Q_{Heater} = Q_{sensible-L} + Q_{latent-s} + Q_{sensible-s} + Q_{mushy} \quad (5.2.) \\ + Q_{acrylic\ walls} + Q_{copper} + Q_{insulation} + Q_{losses}$$

The transient thermal profiles for the average temperature of the copper sheet, temperature of the thermocouple mounted at the bottom of the PCM, temperature measured by the thermocouple mounted at the riser and the transient melt front location were curve fitted.

5.1.1. Sensible Heat Stored in the Molten PCM

The sensible energy stored in the molten PCM can be calculated by the following relations

$$Q_{sensible} = m_l c_l (T_{average} - T_{ambient}) \quad (5.3.)$$

Where $T_{average}$ is the average temperature of the molten PCM assuming a linear temperature distribution and $T_{ambient}$ is the temperature at the beginning of melting

$$T_{average} = \frac{T_s + T_m}{2} \quad (5.4.)$$

And the mass of molten PCM is calculated as follows

$$m_l = \rho AS(t) \quad (5.5.)$$

where $S(t)$ is the measured melt front location at any given time. By these measurements the amount of sensible energy stored inside the molten PCM can be calculated at any given time.

Melting starts at the top of the cell at the heater surface and progresses downwards. As a result, the dominant mode of heat transfer is heat conduction. In order to estimate the sensible energy stored in the liquid (molten) PCM, the temperature distribution in the liquid phase and the amount of melt at any given time must be known. A linear temperature distribution from the surface temperature of the heater (T_s) to the higher melting temperature of the PCM is assumed. This assumption is valid for the 0 kV case since a thermally stratified liquid phase is assured due to the nature of melting and due to the slow heat transfer process it is a quasi-steady process.

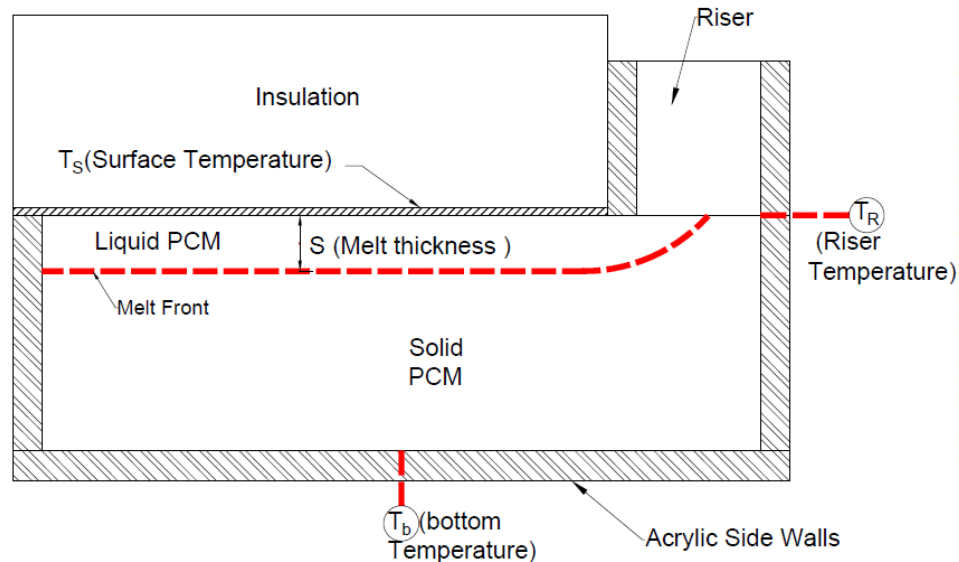


Figure 5.1 Schematic of energy balance model

The melt thickness $S(t)$ at any given time, is measured from the experimental data using high speed imaging. At the early stages of melting, the melt front progresses uniformly downward underneath the copper sheet. However at the riser area the melt front progress is not unidirectional, but it rather progresses downwards and towards the acrylic side walls forming a curved solid-liquid interface (Figure 5.1). This curved shape created by the melt front induces natural convection in the riser area which is stronger near the top at the free surface. The induced natural convection increases the melt front velocity at the top until the melt front becomes horizontal again and the melt thickness, $S(t)$, is almost uniform everywhere.

5.1.2. Latent Heat Stored in the Molten PCM

The amount of latent heat stored at any given time is equal to the latent heat of fusion multiplied by the mass of the molten PCM at this time and can be calculated as

$$Q_{latent} = m_l \Delta H_f \quad (5.6.)$$

where the quantity m_l is calculated based on equation (5.5.)

5.1.3. Energy Stored in Solid PCM and Mushy Zone

The thickness of the mushy zone and the temperature profiles inside the mushy zone and the solid PCM have to be estimated in order to calculate the energy stored in the solid PCM and the mushy zone. Heat transfer in any of these zones occurs by heat conduction only where heat diffuses from the interface (constant temperature) as a thermal penetration depth layer that is continuously growing till it reaches the bottom wall. An integral approximate method with a second order temperature distribution across these zones can be assumed with three boundary conditions needed to satisfy the equation (Faghri, et al., 2006). The three boundary conditions are the temperature at the bottom, T_b , measured by the bottom thermocouple and the temperature at the beginning of the mushy zone, which equals to the melting temperature which equals to 63 °C and the last one is assuming a zero gradient (zero heat loss) from the bottom due to the mounted insulation at the bottom. In Figure 5.2, the schematic for the temperature distributions inside the cell for the PCM is shown along with the mushy zone thickness (δ). Solving

the 2nd order polynomial equations using these three boundary conditions, the solution for the temperature distribution at a given distance x can be given by

$$T_x = T_b + \frac{(63 - T_b)}{(36 - S)^2} x^2 \quad (5.7.)$$

where the mushy zone is the region between the lower and higher melting temperatures (Refer Appendix B) and can be estimated from the previous relation by substituting $T_x = 53^\circ\text{C}$ (lower melting temperature), from which

$$\delta(t) = (36 - S) \left[1 - \sqrt{\frac{53 - T_b}{63 - T_b}} \right] \quad (5.8.)$$

For an experimental timeframe of one hour, the mushy zone thickness was equal to 4.5 mm and the thickness of the solid PCM was equal to 23 mm. The mushy zone thickness was relatively small compared to the solid PCM region. Therefore assuming linear temperature inside the mushy zone is a suitable approximation and the amount of latent heat energy stored in the mushy zone can be calculated by the following relation

$$Q_{latent-mushy} = 0.5 \times \rho A \delta(t) \Delta H_f \quad (5.9.)$$

and the sensible energy stored in the mushy zone can be calculated as follows

$$Q_{sensible-mushy} = \rho A \delta(t) C_m (58 - T_{ambient}) \quad (5.10.)$$

the average temperature for the solid PCM is calculated as

$$\bar{T}_{s-PCM} = T_b + \frac{1}{3} (53 - T_b) \quad (5.11.)$$

and then the sensible stored energy in the Solid PCM is calculated by

$$Q_{sensible-PCM_s} = \rho A(36 - S - \delta) C_s (\bar{T}_{s-PCM} - T_{ambient}) \quad (5.12.)$$

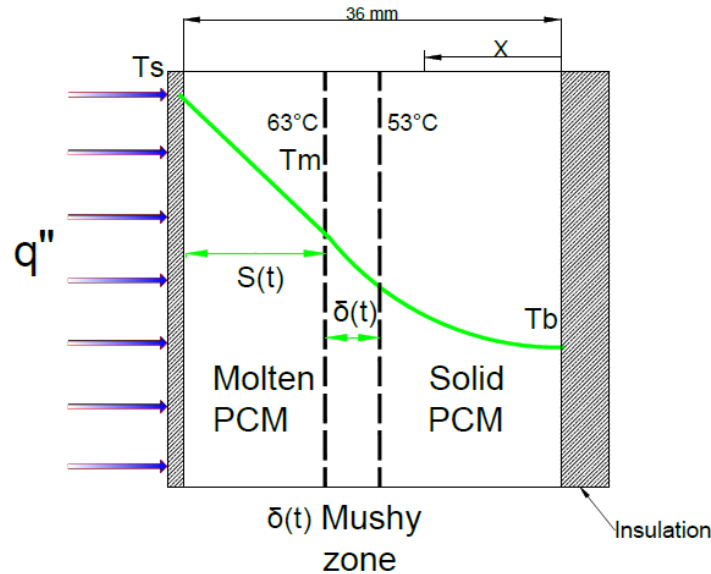


Figure 5.2 Schematic for the temperature distributions inside the PCM

5.1.4. Sensible Energy Stored in the Acrylic and the Copper Sheet

The energy stored in both the acrylic side walls which are enclosing the PCM and the copper sheet is sensible energy. For the acrylic side walls, the same approach for estimating the temperature distribution inside the solid PCM-equation (5.11.) is used to estimate the average temperature of the acrylic sheets. The boundary conditions for the 2nd order polynomial are the temperature of the copper sheet, which resembles the temperature of the top of the acrylic sheet ($x = 36 \text{ mm}$), the temperature at the bottom T_b at ($x = 0 \text{ mm}$) and the zero temperature gradient at the bottom. The solution of the 2nd order polynomial equation subject to these boundary conditions is then:

$$\bar{T}_{acrylic} = T_b + \frac{1}{3} (T_s - T_b) \quad (5.13.)$$

and the sensible energy can then be calculated as before using same procedures for estimating the sensible energy presented in section 5.1.1.

The average temperature readings for the copper sheet by the thermocouple is taken as the average temperature of the copper sheet and due to the very small thickness and high thermal conductivity of the copper.

5.1.5. Sensible Energy Stored in the Thermal Insulation

The sensible energy stored in the thermal insulation was estimated for the top and the side thermal insulation. A thermocouple was attached at the top surface of the top insulation to acquire the temperature. The top insulation temperature distribution was assumed to behave as 2nd order polynomial and the average temperature was calculated as the same way as in Section 5.1.3.

The average temperature at the side insulation was assumed to be the same as that for the acrylic side walls, and from that the sensible energy was computed for the side thermal insulations.

5.1.6. Analytical Model Results

The energy stored inside the system at any given time can be found by calculating each of the 7 components; equation (5.3.) to equation (5.13.). The energy balance is defined by comparing the electric heater energy input to the system by equation (5.1.) and comparing it to the energy stored and energy lost to the surroundings

From equation (5.2.), by calculating the 7 different components of energy stored in the test section and comparing it to the electric heater energy input, the heat losses from the test section to the surroundings can be estimated.

It is assumed that time, $t = 0$ when the surface temperature of the copper sheet was equal to the high melting temperature 63°C . This is achieved approximately after 10 minutes from starting the electric heater, for the 14.2 W case, and at that time the melt thickness was set to zero.

As mentioned before, due to the presence of the riser, the progress of the melt front is not parallel to the surface of the heater everywhere. At the riser region the melt front progresses in two directions, one downwards parallel to the surface and the other laterally towards the sides of the riser. Until the melt front touches the riser, the estimation of the melt thickness at any given time and the temperature distribution inside the liquid PCM will be inaccurate. The calculations are only valid at the time the melt front touches the riser and the melt front progresses uniformly and parallel to the surface of the copper sheet. The time the melt front touches the riser is determined from the thermocouple mounted at the riser. At time $t = 30$ minutes it was observed a steep increase in temperature which indicates the transition from solid to liquid phase.

In Figure 5.3 the energy balance results for the analytical model is presented, where the cumulative energy is shown on the y-axis against time at the x-axis. The cumulative energy is plotted for one hour experiment for 14.2 W electric heater power input. The energy stored in each component of the test section is calculated and the summation of these components is called $Q_{calculated}$ and is plotted with $Q_{I/P}$ (heat input from the

heater). The $Q_{calculated}$ is plotted only after the melt front touches the riser at time $t = 30$ minutes. From Figure 5.3, it is observed that the difference between the $Q_{I/P}$ and $Q_{calculated}$ increases as the time increases. This indicates an increase in the energy losses to the surroundings as the time increase due to the increase of the surface temperature of the copper sheet and the system with time. As the temperature increases, the convective losses to the surroundings increase. At the end of the one hour experiment, the amount of energy stored inside the system is equal to 84.5% of the total energy input to the system. This indicates the amount of heat loss equals to 15.5% of the total energy input to the system.

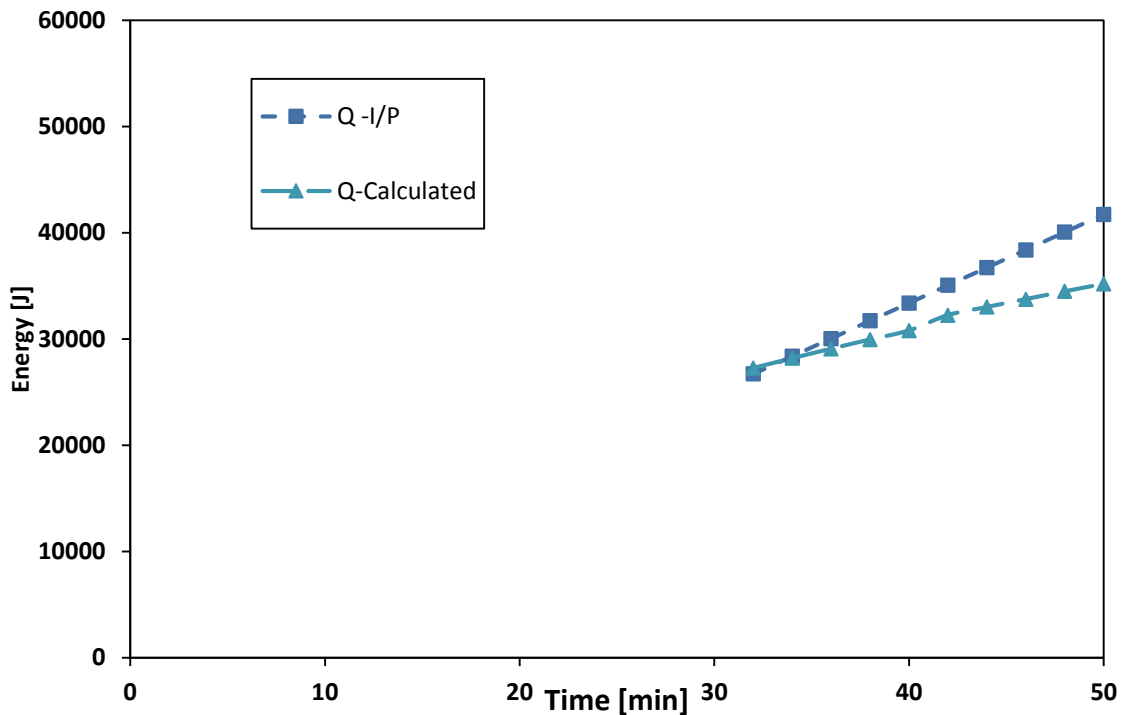


Figure 5.3 Analytical model Energy balance results

5.2. Two Dimensional Numerical Storage Cell Model

A two dimensional CFD numerical model was developed to support the analytical thermal heat balance model and compared with the experimental results for validation. The heat losses from the experimental test section to the surroundings were calculated from the CFD model to assess the accuracy of the results. The commercial CFD software, ANSYS-Fluent, was used to solve a 2D numerical model. The energy, melting/solidification and laminar flow models were used in the simulations. The Boussinesq density approximation for buoyancy driven flows was used in the simulation where natural convection effects could play a role in the melting of the riser area. The transient solver was used with second order upwind in both energy and momentum equations and domain initialization was set to a uniform temperature equal to the ambient temperature of 21°C and an initial zero velocity for all domains.

A schematic of the 2D numerical geometry can be seen in Figure 5.4. The boundaries of the model are set to a convective heat transfer boundary conditions and the values of the heat transfer coefficient are shown in Figure 5.4. The heat transfer coefficients were estimated based on the natural convection correlations from a constant temperature vertical surface [equation (5.14.) - (Vliet, 1969)] and horizontal surface with the hot side facing upwards [equation (5.15.) - (McAdams, 1954)] or downwards [equation (5.16.)- (McAdams, 1954)]. As it is a transient thermal problem, the heat transfer coefficients were based on the average temperature calculated from the experimental data of a 14.2 W case and 0 kV.

The material properties used in the CFD simulation can be found in Table 5.1.

$$Nu = \left\{ 0.825 + \frac{0.387 Ra^{1/6}}{[1 + (0.492/Pr)^{9/16}]^{8/27}} \right\}^2 \quad (5.14.)$$

$$Nu = 0.54 Ra^{1/4} \quad (10^4 \leq Ra \leq 10^7) \quad (5.15.)$$

$$Nu = 0.27 Ra^{1/4} \quad (10^5 \leq Ra \leq 10^{10}) \quad (5.16.)$$

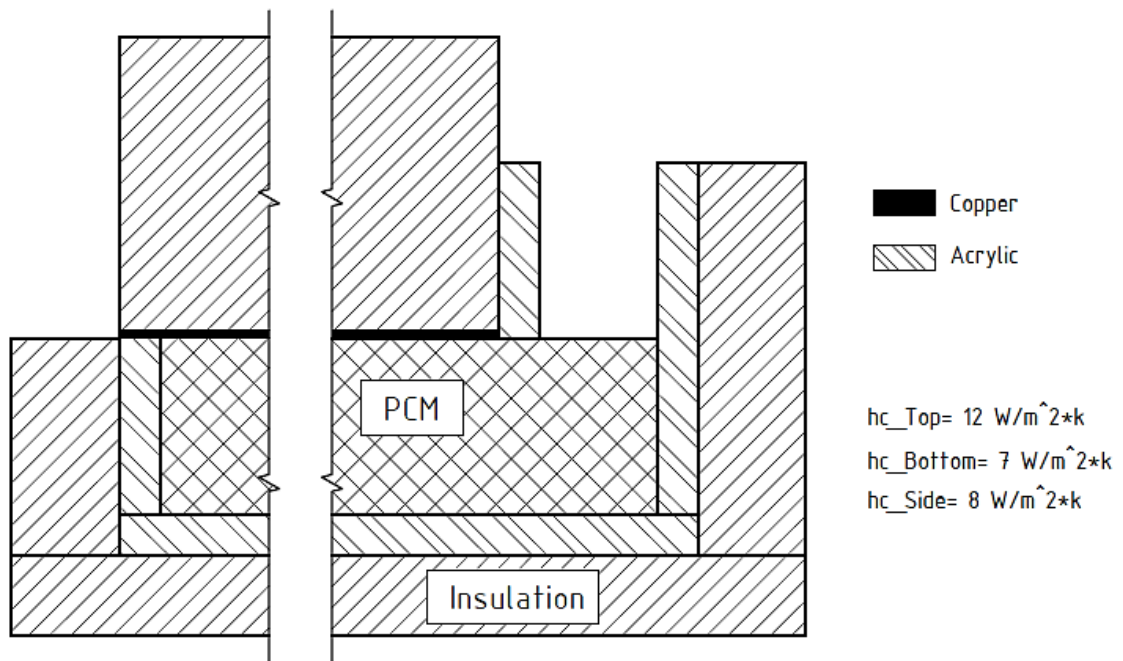


Figure 5.4 Schematic of the two dimensional CFD model

Table 5.1 Material properties for the two dimensional CFD case

Property	Units	Copper	Acrylic	Paraffin Wax	Insulation
Density	$[Kg/m^3]$	8978	1180	946.7	248
Heat capacity	$[J/KgK]$	381	1465.38	2890	920
Thermal conductivity	$[W/mK]$	387.6	0.187	0.232	0.078
Kinematic viscosity	$[Kg/ms]$	N/A	N/A	0.003976	N/A
Latent heat of fusion	$[J/Kg]$	N/A	N/A	192000	N/A
Melting temperature	$[^{\circ}C]$	N/A	N/A	63	N/A
Freezing temperature	$[^{\circ}C]$	N/A	N/A	53	N/A
Volumetric expansion coefficient	$[1/K]$	N/A	N/A	0.00074	N/A

A grid independence study was performed to determine the grid size required in the simulations. The temporal profile of melt front location was used as the parameter for comparing the different results of grid sizes. Three hexahedral meshes with different grid sizes were chosen for comparison where the number of elements for the three meshes from the finest to the coarsest mesh are 79021, 23669 and 9989 elements, respectively. A comparison of the results for the 3 different mesh sizes for 14.2 W case is shown in Figure 5.5. The melt thickness at the end of the one hour duration is almost the same for the three different meshes while for the time frame between 35 and 50 minutes the coarsest mesh diverges away from the other two meshes.

A time step study was performed for the finest mesh case to determine the maximum time step size that can be used without affecting the accuracy of the model. Since this is mainly a heat diffusion problem, even if natural convection effects take place at the riser area, the velocities are expected to be very small due to the uni-directional melting. The time step size was chosen assuming a Courant number equals to 0.5 for the PCM and using the finest grid size to get an accurate estimation for the position of the melt front. Figure 5.6 shows the effect of changing the time step size on the accuracy of the results for the melt front location with time. Three time step sizes of 1 second, 0.5 second and 0.25 second were tested. It is observed that both the 0.25 and 0.5 second time step size were in agreement while the 1 second time step size had a slight discrepancy starting from $t = 30$ min till the end of the simulation time. To ensure a good solution was achieved, the finest grid size with a time step size of 0.5 second was employed for solving the numerical model.

Accuracy of the analytical model assumptions for the temperature distribution in the solid, liquid and mushy zone domains are compared to the numerical results for the temperature distribution. A comparison between the numerical and analytical temperature distribution is shown in Figure 5.7, the results indicate a good agreement within a maximum deviation of 4% between the two models.

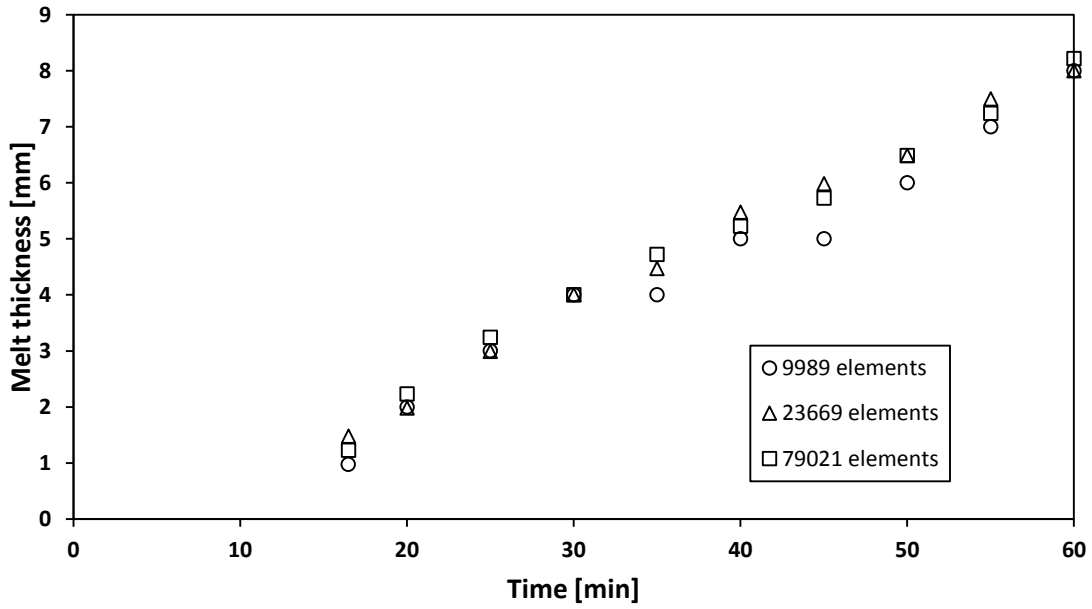


Figure 5.5 CFD grid independence study result- 14.2 W and 0 kV case

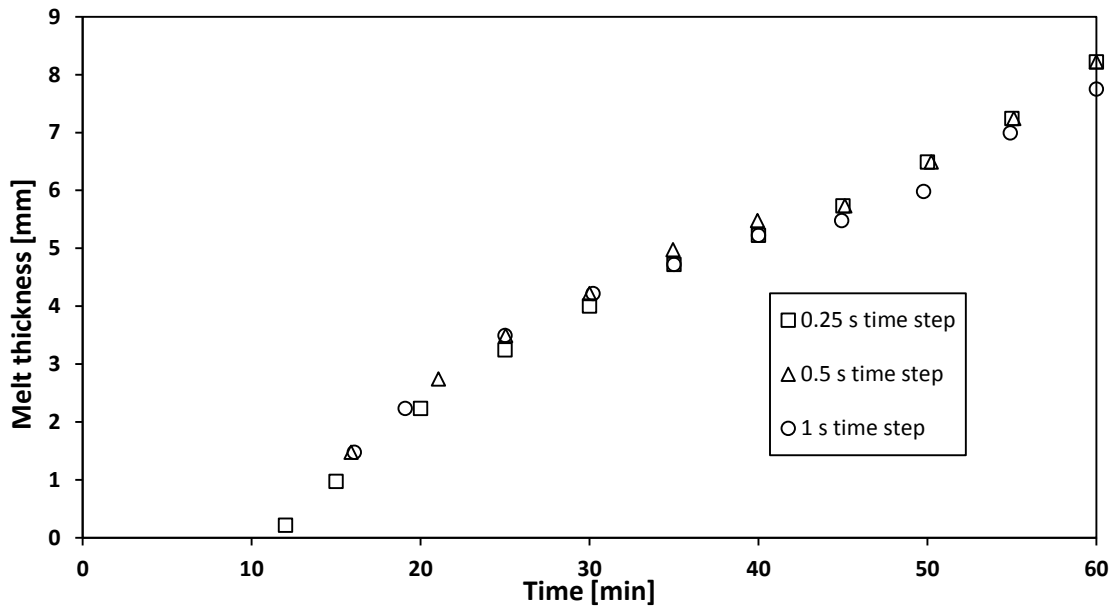


Figure 5.6 CFD time step independence study result-14.2 W and 0 kV case

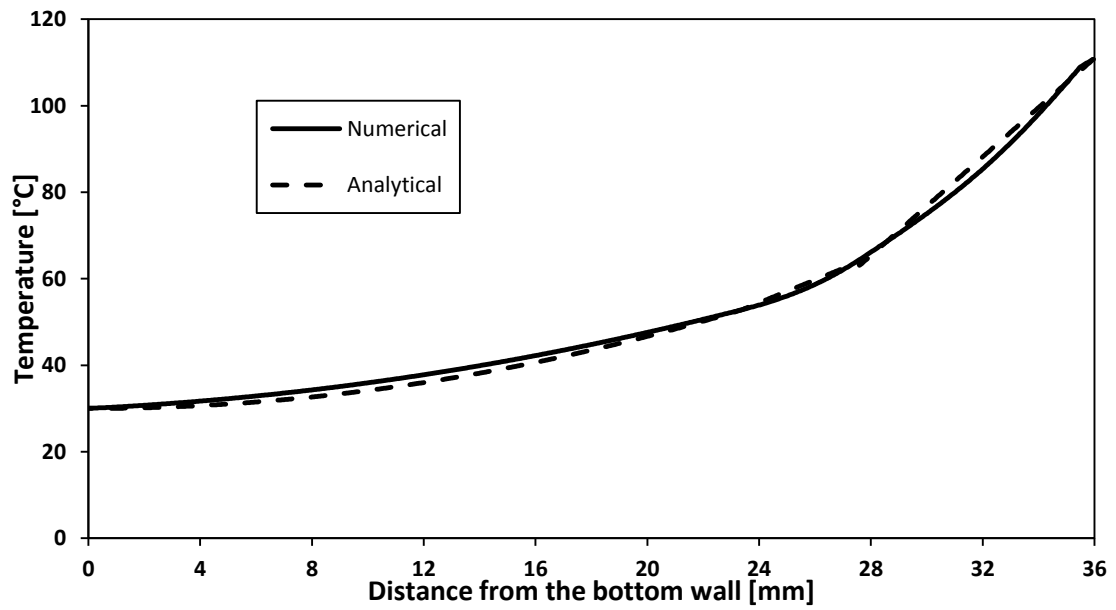


Figure 5.7 Longitudinal temperature distribution for the numerical and analytical model

5.2.1. Validation of the Numerical Model

The comparison between the CFD results and the experimental results for the temporal profile of both the melt front location and the average surface temperature of the heating surface are shown in Figure 5.8 and Figure 5.9 respectively.

The numerical solution agrees well with the experimental data with 4.5 % deviation in the melt front estimation and 9 % deviation for the average surface temperature estimation at the end of one hour duration. There is slight discrepancies between the numerical and experimental results observed in the melt front location between 6 and 7 mm thickness. This can be attributed to the absence of the H.V. electrodes in the numerical model for sake of simplifying the model. The presence of the upper row of electrodes ($S=7$ mm) increase the effective thermal conductivity of the PCM causing a higher melt thickness and lower surface temperature for the experimental results over the numerical model.

Additionally, the numerical model was used to estimate the heat losses from the system to the surroundings. The energy balance for the system was performed by calculating the heat energy stored and the heat losses from the system and comparing it to the heat energy input to the system, by that numerical energy balance and validity of the numerical model was confirmed.

5.2.2. Energy Stored in the System

The average temperature for each of the seven component was calculated for different time instants and the sensible energy was estimated for each.

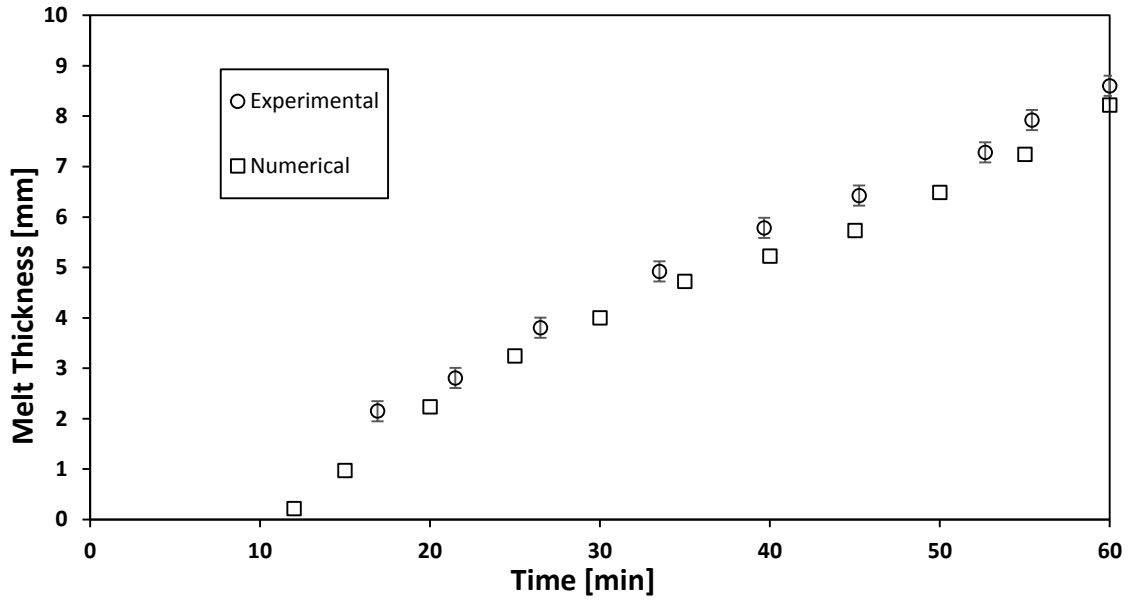


Figure 5.8 Melt front location (measured from the heating surface) against time for $Q = 14.2$ Watts

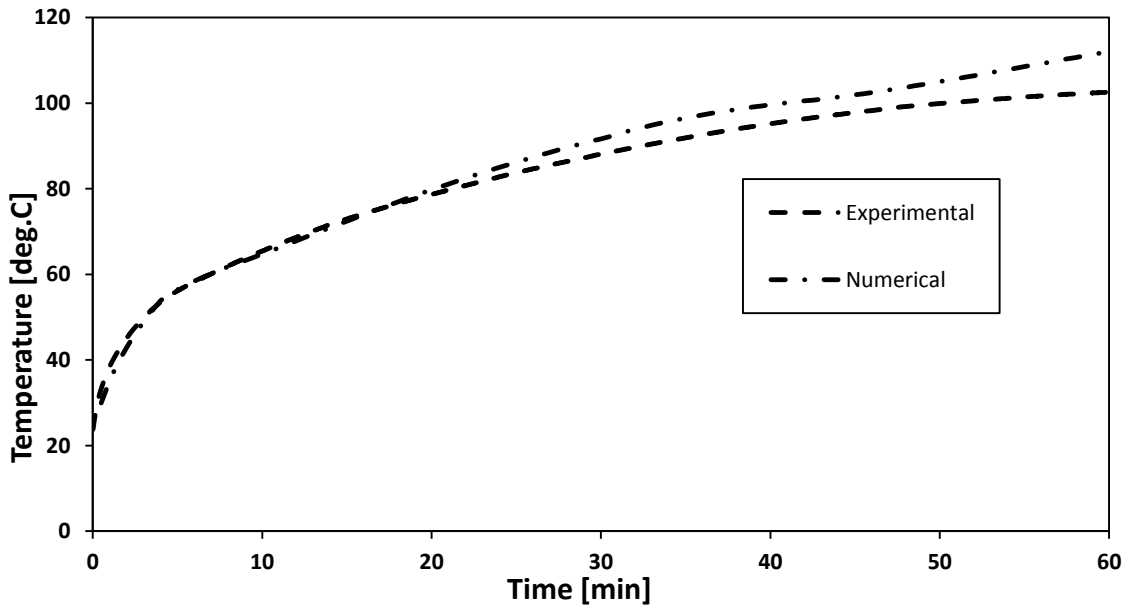


Figure 5.9 heating surface average temperature variation with time for $Q = 14.2$ Watts

The average liquid fraction of the PCM was calculated to estimate the overall latent energy stored in the molten PCM and the mushy region. The sensible energy stored for a body i is given by

$$Q_{sensible_i} = m_i c_p (\bar{T}_i - T_{ambient}) \quad (5.17.)$$

While the latent energy stored in the PCM is given by

$$Q_{latent_i} = \bar{\alpha} m_{PCM} \Delta H_f \quad (5.18.)$$

And the total energy input to the system after certain time t is calculated by

$$Q_{I/P} = Q''' V_h t \quad (5.19.)$$

For the 14.2 Watts heat input case the numerical simulation was performed for one hour duration as the experimental procedure. In Table 5.2 the CFD model results for the energy stored in the different components of the thermal storage system can be found for different instants of time. The energy was calculated based on the two dimensional model and assuming 1 m depth of the storage cell.

The results of the analysis were presented in Figure 5.10, indicating a decrease in the amount of energy stored in the different components of the cell with time. This indicates an increase in the amount of heat losses to the surrounding due to the increase in the system temperature and the increase of the convective losses. At the end of 1 hour the amount of the energy stored inside the thermal storage system is equal to 89.3 % of the total input energy to the system, this means an energy loss to the surrounding equal to 10.7 % of the total input power.

Table 5.2 CFD model results for stored energy analysis results of the thermal system

Time [min]	Insulation [J]	Acrylic [J]	PCM [J]	Copper [J]	ΣQ Stored [J]	Q I/P [J]	% stored
60	64535	46718	591102	25790	728146	815673	89
50	56196	36356	496671	23793	613018	679727	90
40	47671	24397	399575	22250	493895	543782	90
30	38151	17315	296069	19981	371517	407836	91
20	27227	10751	196745	16594	251318	271891	92
10	15579	5538	95383	12323	128825	135945	94

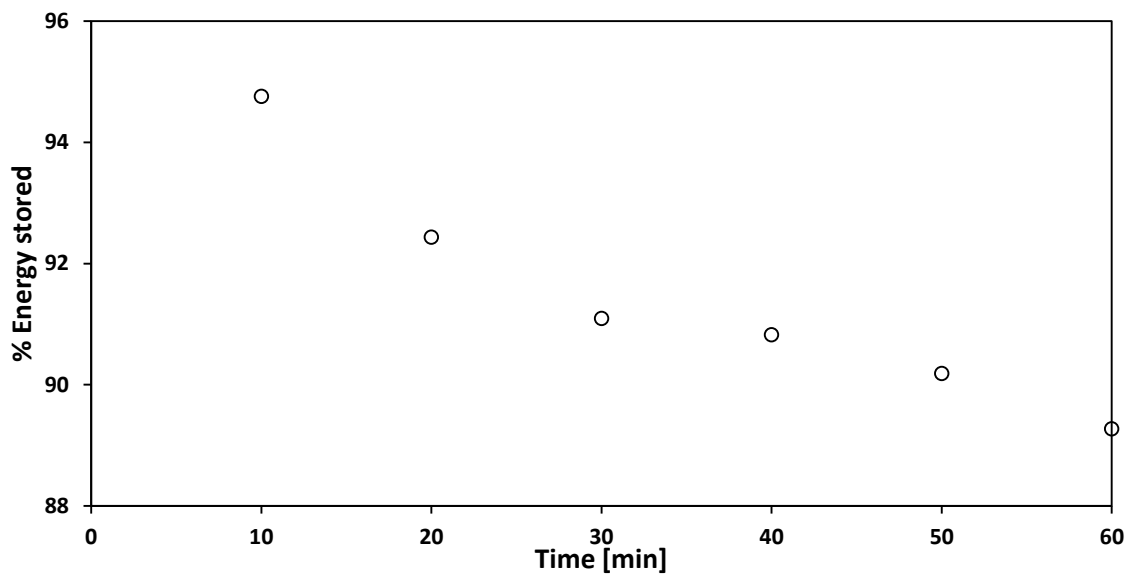


Figure 5.10 CFD stored energy analysis with time

The heat losses to the surroundings were calculated and compared to the amount of stored energy to confirm the accuracy of the CFD model and to estimate the heat losses as a function of the average surface temperature of the copper sheet. The heat losses were calculated every 10 min, same method as stored energy calculation.

However, the heat losses were calculated in terms of power not cumulative energy. The rate of energy losses for a given surface i facing the ambient air is calculated by the given equation

$$\dot{Q}_{losses(i)} = h_c A_i (\bar{T}_i - T_{amb}) \quad [W] \quad (5.20.)$$

The heat transfer coefficients for the natural convection can be found in Figure 5.4 , where the total heat losses from the top, side and bottom surface were calculated and represented in Table 5.3. Similar to thermal energy stored analysis, the calculated numbers are based on a two dimensional CFD model with 1 m depth. However the numbers presented are in terms of power [W] at every given time not in accumulative energy [J] as the energy stored analysis. The results of the CFD analysis and the amount of heat power lost from the cell due to natural convection is presented in Figure 5.11 , where at the end of one hour duration the rate of heat loss was equal to 22.9 % of the rate of heat input to the system. In order to confirm the energy balance of the CFD model, the amount of the energy lost from the system to the surroundings need to be calculated and compared against the amount of energy stored. The total energy lost from the system at any given time (t) can be calculated from the area under the curve for the heat power lost with time by the following relation

$$Q_{losses} = \int_0^t (\sum Q(t)_{loss}) dt \quad [J] \quad (5.21.)$$

Table 5.3 CFD model results for heat loss analysis of the thermal system

Time [min]	Q loss Top [W]	Q loss Side [W]	Q loss bottom [W]	Q loss total [W]	Q I/P [W]	% Loss
60	14	36	2	52	225.2	22.9
50	12	33	1.6	46	225.2	20.6
40	10	23	0.6	33	225.2	14.8
30	8	17	0.2	25	225.2	11.3
20	5	11	0.03	16	225.2	7.3
10	3	5	0	9	225.2	3.8

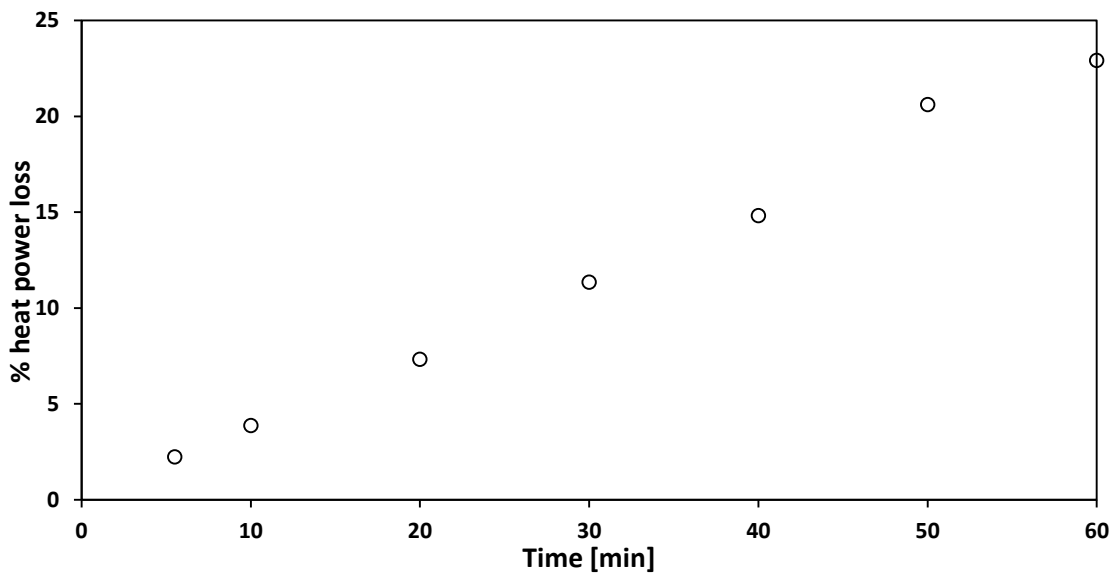


Figure 5.11 CFD heat loss analysis with time (14.2 Watts-0 kV)

From curve fitting the data in Figure 5.11 the total heat lost at any given time can be calculated easily from equation (5.21.). The total energy lost at the end of the one hour duration was calculated by using the previous procedures and was found to be equal to 11.5 % of the total energy input. The value of the heat stored added to the value of heat

lost is equal to 100.8 % of the total heat energy input to the system achieving a good energy balance assuring a reliable CFD model.

The 14.2 W, 0 kV case has the highest temperatures profiles from the experimental data, which indicates the highest heat losses from all the other experiments. The heat loss from any surface is a function in the surface temperature and since the surfaces temperatures are related to the temperature of the heat source, which can be expressed as a function of the average surface temperature of the copper sheet, the heat loss can be expressed directly as a function of the average surface temperature of the copper sheet. The amount of energy lost from the system was plotted against the average temperature of the copper sheet which corresponds to that instant of time. The percentage of heat power loss as a function of the surface temperature for the 14.2 Watts case is presented in Figure 5.12 . This can be used to estimate the heat losses from the different heat input cases by plotting the percentage of heat loss for each heat input case with time and calculating the average heat loss rate. Figure 5.13 to Figure 5.15 the heat loss analysis for the 6 different cases; 3 different heat input values for the 0 kV and - 8 kV cases were presented.

The average heat rate loss which represents also the total energy lost to the surroundings is calculated for each case and can be found in Table 5.4. The maximum percentage for energy lost to the surroundings equals to 18.5 % for the 10.3 W and 0 kV case while the lowest percentage is 8.5 % at the 14.2 W and - 8 kV case.

The percentage difference in the amount of heat lost between the 0 kV and - 8 kV case for each heat input value ranges from 2.5 % to 4 % of the heat input value. The percentage heat loss for - 8 kV case is always smaller than that for the 0 kV case.

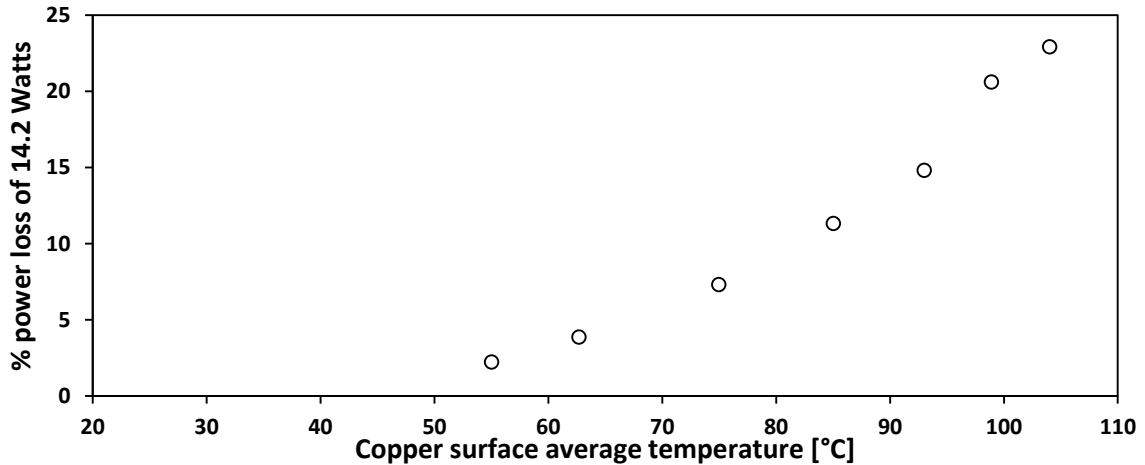


Figure 5.12 CFD heat loss analysis against copper average surface temperature (14.2 Watts)

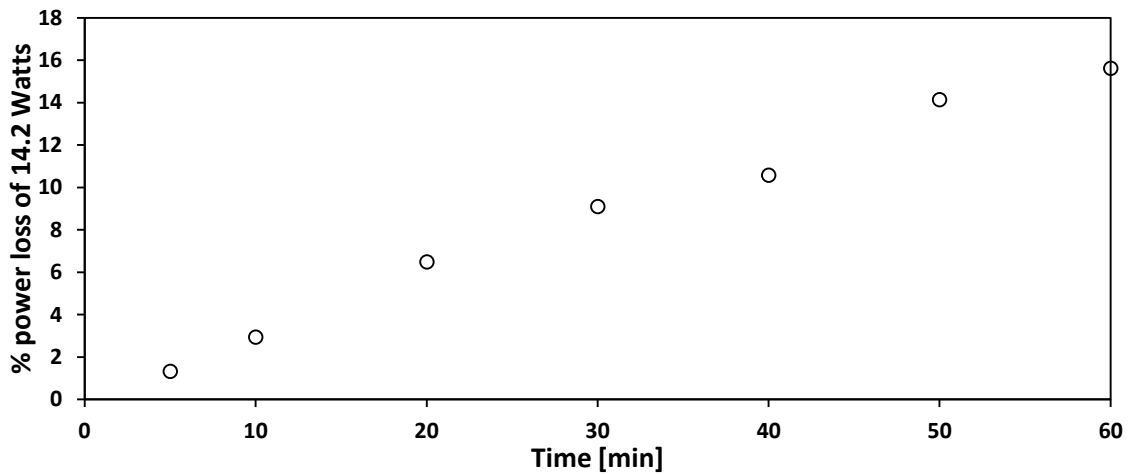


Figure 5.13 CFD heat loss analysis with time (14.2Watts-Neg 8kV case)

However the heat losses from the -8 kV cases could be underestimated as the temperature distribution inside the liquid phase is unknown and it is calculated based on the assumption that it has the same temperature distribution as a 0 kV case with the same surface temperature. The 0 kV assumption implies a stratified molten PCM zone with an almost linear temperature distribution from the surface of the heater till the melt front

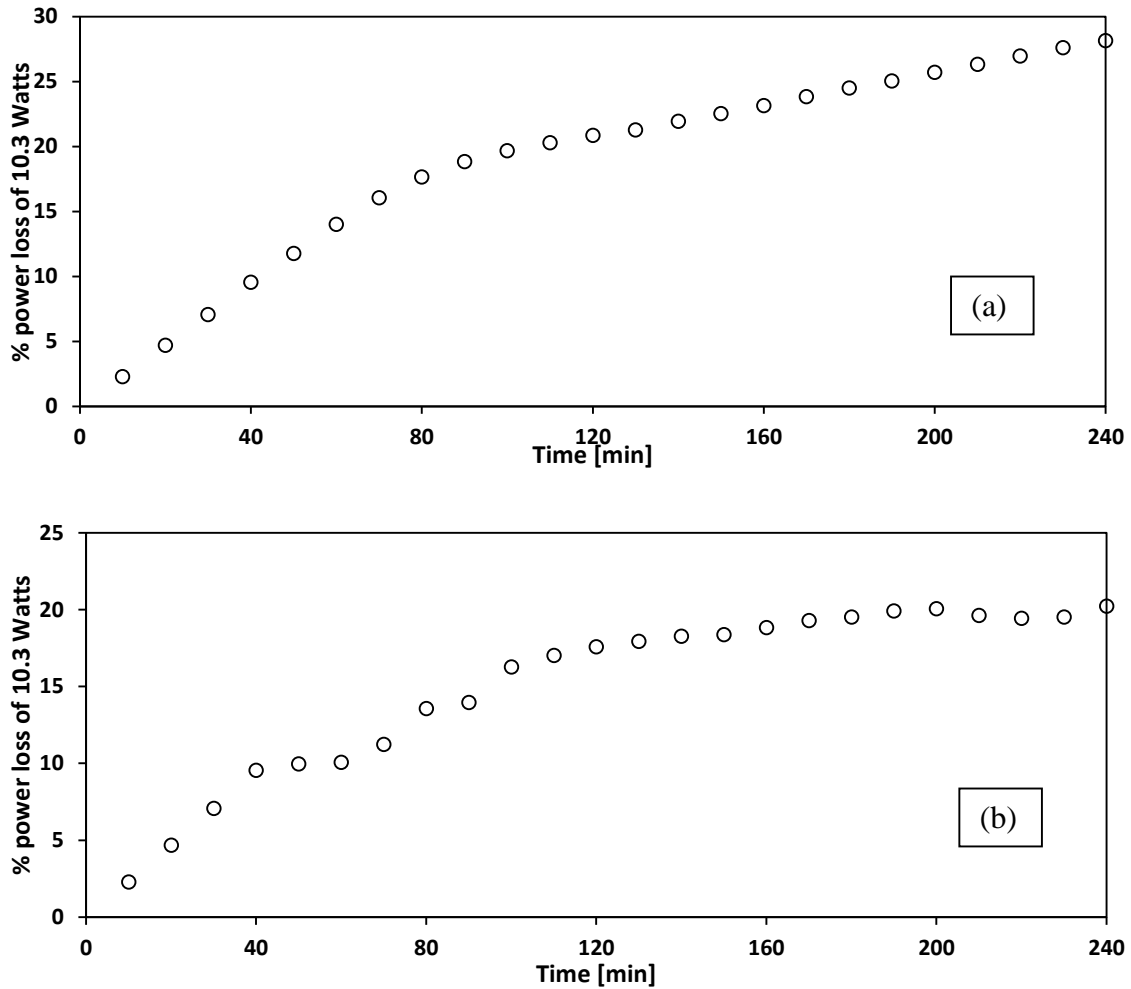


Figure 5.14 CFD heat loss analysis with time for 10.3 Watts (a- 0 kV, b- Neg 8 kV)

location, however it is expected to have a more uniform temperature for the EHD case due to the mixing and solid dendrites extraction that is induced by the EHD forces inside the molten PCM. This will eventually lead to a higher heat rate loss from the sides of the cell than the assumed.

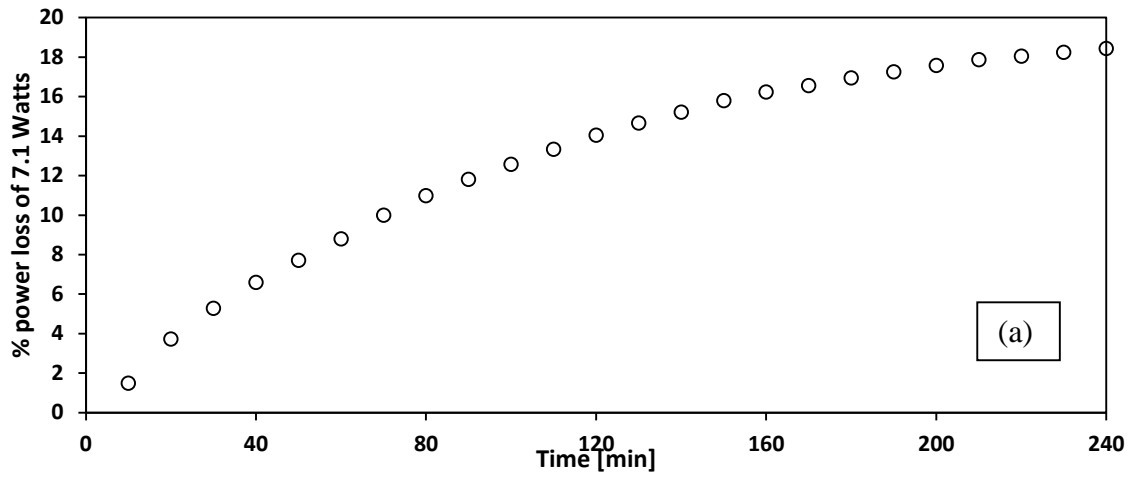


Figure 5.15 CFD heat loss analysis with time for 7.1 Watts (a- 0 kV, b-Neg 8 kV)

Table 5.4 Percentage of total heat loss for the different experimental cases

Heat Input [W]	0 kV	Neg 8 kV
14.2	11.5%	8.5%
10.3	18.6%	14.8%
7.1	12.5%	10%

5.3. Performance Characterization and Uncertainty Analysis

The experimentally measured parameters were used to evaluate the thermal performance for the latent heat thermal storage cell. Lists of the measured parameters can be found in section 4.3 at Table 4.1. The calculated parameters are shown in Table 5.5. The transient thermal trend for the average temperature of the copper sheet along with the temporal melt front progress were used for comparison between melting with and without EHD.

The average surface temperature of the copper sheet can be expressed by

$$\bar{T}_S = \frac{1}{4} \sum_{i=1}^{i=4} T_{S,i} \quad (5.22.)$$

Table 5.5 The calculated parameters

Symbol	Calculated Parameter
\bar{T}_S	Copper sheet average surface temperature
dS/dt	Melt front velocity
EF	EHD enhancement factor
P_{heater}	Electric heater power input
P_{EHD}	EHD power input

Curve fitting is performed for the temporal melt front progress for each of the EHD and no EHD cases. The melt front velocity (dS/dt) is calculated by differentiating the obtained equation from curve fitting.

A new term called EHD enhancement factor (EF), defined by equation (5.23.) is used to quantify the EHD heat transfer enhancement at any given liquid level. The term represents the ratio between the melt front velocity with EHD and without EHD.

$$EF = \frac{\left(\frac{dS}{dt}\right)_{EHD}}{\left(\frac{dS}{dt}\right)_{No\ EHD}} \quad (5.23.)$$

A 95 % confidence band was used to assess the confidence in the calculated parameters from curve fitting which are the melt front velocity and the enhancement factor.

EHD power consumption was calculated by monitoring both the current and voltage readings recorded using an oscilloscope. The instantaneous EHD Power consumption (P_{EHD}) is given by

$$P_{EHD} = V(t)_{EHD} \times I(t)_{EHD} \quad (5.24.)$$

The electric heater power input are calculated in the same way by monitoring both the voltage and the current from the DC power supply. [Equation (5.1)]

• Uncertainty Analysis

The experimental uncertainties are computed in accordance with (Kline, et al., 1953) for the experimental measurements. A summary for the experimental uncertainties can be found in Table 5.6 .

Details for the uncertainty analysis can be found in Appendix C.

Table 5.6 Experimental uncertainties

<u>Measurement</u>	<u>Max. Uncertainty</u>
Temperature	± 0.5 °C
Voltage	± 0.07 %
Current	± 0.35 %
Melt thickness	± 0.15 mm
<u>Calculated parameters</u>	<u>Max. Uncertainty</u>
Power of electric heater	± 0.4 %

5.4. Summary

An analytical model was developed to estimate the energy stored in the different components of the tested latent heat storage cell and to estimate the amount of energy lost to the surroundings in order to quantify the accuracy of the experiment. This analytical model was supported by a numerical model and verified against the experimental results in order to further expand the thermal energy analysis from the 14.2 W case and 0 kV to the all test conditions that were analyzed within the scope of this project.

The numerical thermal model showed a good agreement with the experimental results, indicating an amount of energy lost to the surroundings approximately equals to 12 % of the heat energy input over the course of 1 hour experiment. While for the analytical model this value was estimated to be equal to 16 % of the total energy input. For the analytical model there could be an under estimation for the average temperature distributions inside the solid PCM region due to the 2nd order polynomial temperature assumption which may lead to an overestimation of the energy losses from the system. Additionally, the energy losses to the surroundings, calculated from the numerical model, could be underestimated due to the two dimensional model assumption.

For any 0 kV and - 8kV case there was only a maximum of 4% difference in the amount of heat lost to the surrounding which is more for the 0 kV case compared to the - 8 kV case, however, as mentioned previously, this could be underestimated in the - 8 kV case due to the thermally stratified liquid PCM assumption in the EHD case.

6. Experimental Results and Numerical Methodology

In this chapter, the effect of applying high voltage to establish electrohydrodynamic (EHD) forces inside a latent heat thermal storage cell during melting of the PCM- paraffin wax- was examined. Heat required for PCM melting was supplied by an electric heater which is connected to a power supply. The electric heater power was kept constant through the experimental period which corresponds to constant heat flux boundary condition. A criteria of estimating EHD enhancement effects against the 0 kV base cases was developed and used to establish the amount of sensible vs. latent heat stored under EHD enhancement. Tests were performed under three different electric heater power inputs of 7.1, 10.4 and 14.2 W for an applied voltage of -8 kV and a base case of 0 kV.

The static electric field distributions at different melt front locations were solved numerically. The numerical results were used to evaluate the interfacial forces acting on the solid-liquid interface to help establishing a phenomenological understanding of the mechanisms of EHD enhancement.

6.1. DC Electrohydrodynamic Experimental Results

The EHD effect was studied for the three different heater power input values: 7.1, 10.4 and 14.2 W. Average surface temperature of the copper sheet was calculated using 3 type

T thermocouples soldered across the upper surface of the copper sheet. Temperature readings were recorded by the DAQ with a sample rate 1 reading/second. The melt thickness was measured by taking multiple pictures at different instance in time with a maximum of 10 minutes between each picture. Using Digimizer software for edge detection, the distance between the melt front and the bottom of the copper sheet was established.

A schematic representation for the thermal circuit of a latent heat storage system is presented in Figure 6.1. At constant heat flux boundary condition, the total thermal power input to the PCM after the heat losses can be divided into a sensible component stored in the molten PCM and a latent (Interface) component responsible for melting. The sensible energy component is the capacitive part of the thermal circuit, where at a given instant of time part of the heater power is stored as an increase in the sensible energy of the molten PCM. This can be calculated as

$$Q_{sensible} = C_{liquid\ PCM} \frac{d\bar{T}}{dt} \quad (6.1.)$$

Where, \bar{T} , is the average temperature of the molten PCM and $C_{liquid\ PCM}$ is the equivalent heat capacitance for the molten PCM. The rest of the input power goes through the liquid PCM to the solid-liquid interface as a latent energy for melting the PCM and sensible component for the unmolten PCM. This component of thermal power can be expressed as

$$Q_{Interface} = \frac{\Delta T}{R_{Thermal}} = \frac{T_s - T_m}{R_{Thermal}} \quad (6.2.)$$

The $R_{Thermal}$ is the thermal resistance for heat transfer between the heater and the melt front (solid-liquid interface) where T_s and T_m are the average surface temperature of the

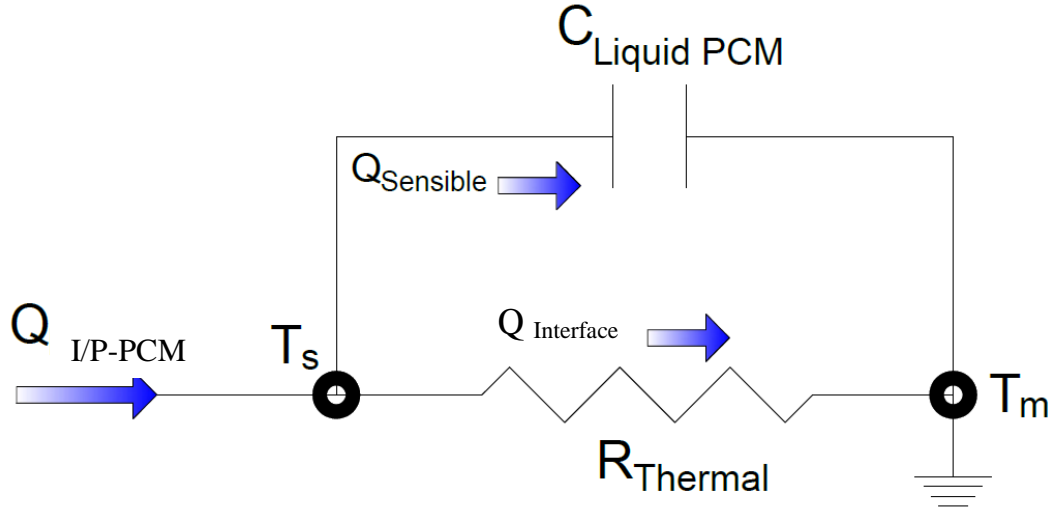


Figure 6.1 A schematic diagram for the thermal circuit.

heater and the melting temperature of the PCM respectively. The total power input can then be calculated as follows

$$Q_{I/P-PCM} = C_{liquid\ PCM} \frac{d\bar{T}}{dt} + \frac{T_s - T_m}{R_{Thermal}} \quad (6.3.)$$

The thermal resistance of the molten PCM is dependent on the dominant mode of heat transfer from the heater to the melt front. Originally the test cell was designed to promote thermal stratification in the molten PCM zone by initiating melting from the top surface in order to minimize any natural convection to study the EHD effect solely in the system. In the 0 kV base case, and in case of horizontal melting from the top surface, the dominant mode of heat transfer will be pure conduction and the thermal resistance will be directly proportional to the amount of melt thickness (S). From equation (6.3.), as the thermal resistance increases, the second term in the right hand side of the equation will decrease but since the amount of heat input (Q_{Heater}) is constant, this means an increase in the sensible component of energy, which will be reflected as an increase in the surface

temperature along with time. Applying a heat transfer enhancement technique will result in decreasing the $R_{Thermal}$ term, leading to a higher rate of heat transfer to the melt front. Decreasing the thermal resistance, means an increase in the second term at the right hand side of equation (6.3.) and therefore a decrease in the sensible component of energy. Figure 6.2 shows the transient thermal profile for the average temperature of the copper sheet (heating surface) for both the 0 kV base case and (-8 kV) at a power heater input value of 7.1 W. It can be seen, in both cases (0 & -8 kV) that the results show a similar trend until time ≈ 90 min indicating that EHD has no effect at the very early stages of melting where the heat conduction thermal resistance is originally small.

After time ≈ 90 min, the rate of temperature rise of the heater surface temperature at (-8 kV) decreases and becomes less than that for the 0 kV base case. After 4 hours, the surface temperature of the copper sheet reached ≈ 80 ° C for the 0 kV case and ≈ 73 ° C for (-8 kV). From equation (6.3.), a decrease in the rate of temperature rise indicates a decrease in the sensible energy component resulting in increase in the latent energy component due to a decrease in thermal resistance. This means EHD forces have contributed in decreasing the thermal resistance between the heater and the melt front and therefore an increase in the amount of melt thickness should be expected. Figure 6.3 illustrates the melt front location (amount of molten paraffin wax) against time for a power heater input value of 7.1 W during a 4 hours experimental period. The melt thickness after 4 hours was 7.3 mm for 0 kV case and 9.3 mm for (-8 kV) case. To quantify the time savings due to heat transfer enhancement, the time taken to melt a 7 mm thickness of the PCM, which corresponds to

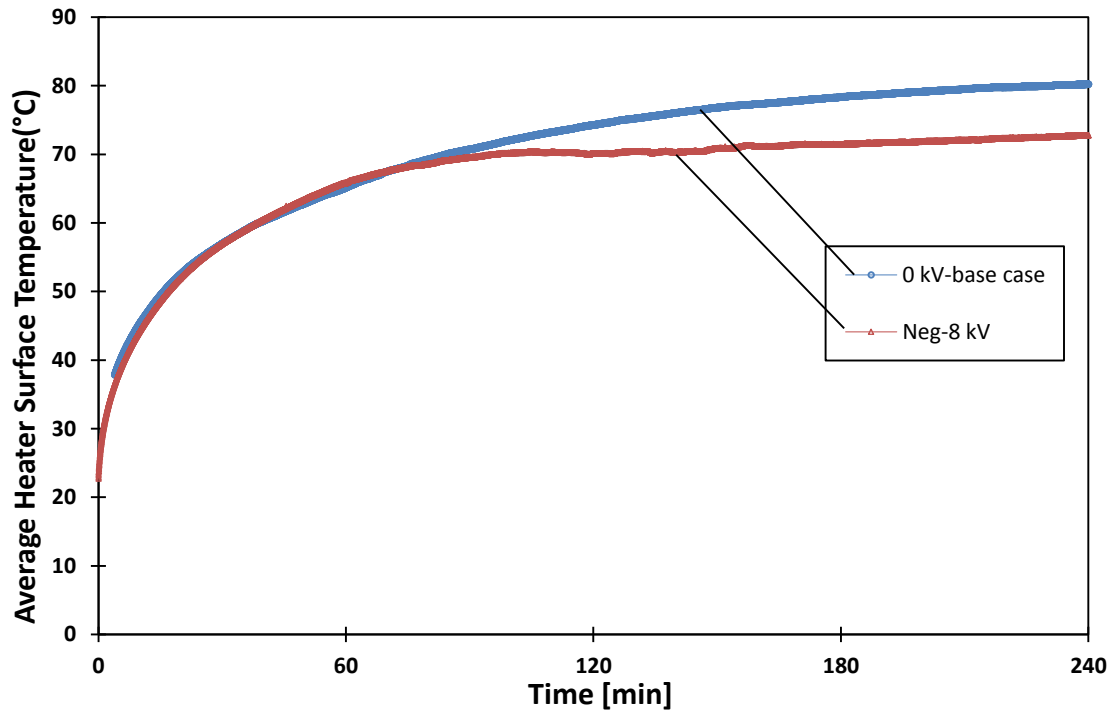


Figure 6.2 Heating surface average temperature variation with time for $Q = 7.1$ W, with and without an applied voltage (-8 kV)

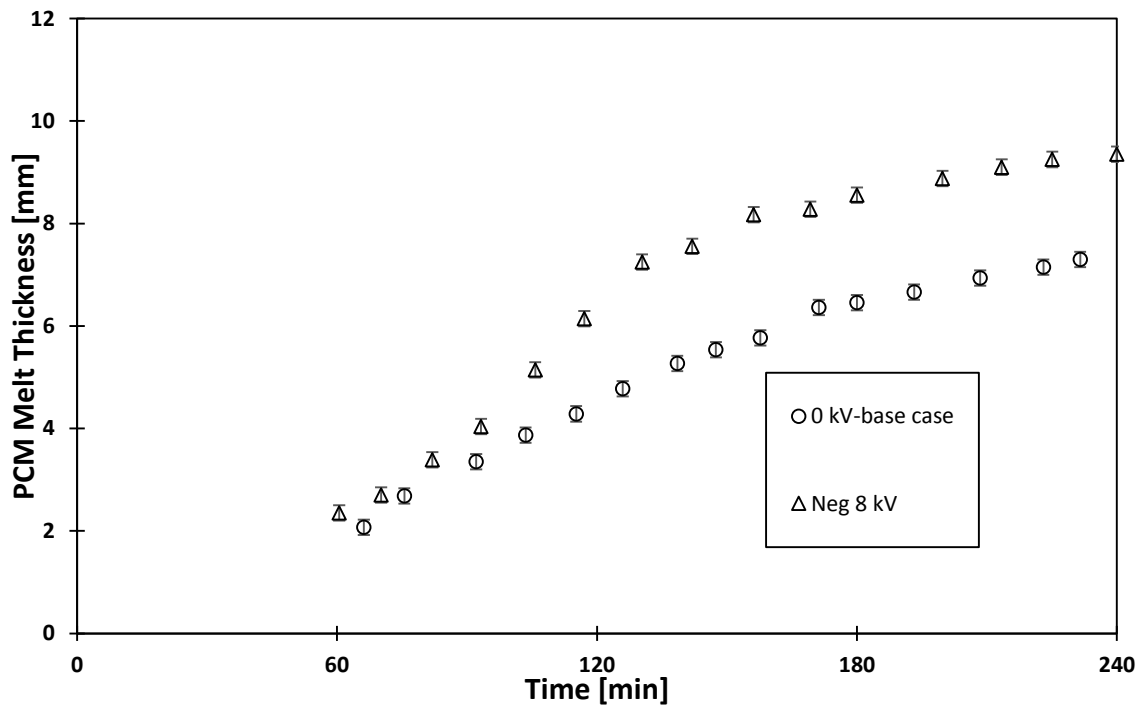


Figure 6.3 Melt front location (measured from the heating surface) with time for $Q = 7.1$ W, with and without applied voltage (-8 kV)

melt front being at the centre line of the first row of electrodes, was used for comparison between the 0kV and (-8 kV) case. The time taken to reach the 7 mm thickness for the 0 kV case was ≈ 210 min, while for the (-8 kV) case it took ≈ 125 min.

Similarly, Figure 6.4 and Figure 6.5 show the transient thermal behavior for the average heater surface temperature and the melt front location respectively for a power heater input = 10.4 W. Similar to the 7.1 W case, both cases (0 kV and - 8 kV) follow a similar trend until time ≈ 40 min. After 40 min, the EHD effect becomes significantly important and the rate of temperature rise for -8 kV case decreases and becomes lower than that for the 0 kV base case indicating a decrease in the thermal resistance due to EHD induced forces inside the molten PCM. The heater surface temperature after 4 hours experimental period reaches ≈ 100 °C for the 0 kV base case and ≈ 91 °C for the - 8 kV case. The melt thickness at the end of the 4 hours was ≈ 12 mm for the 0 kV base case and ≈ 15.5 mm for the - 8 kV case. The time taken to reach the centre line of the first row of electrodes ($S= 7$ mm) was 85 min for 0 kV case and 60 min for (-8 kV) case. It is worth noting, in Figure 6.5, that for the melt thickness range between 10 and 11 mm the melt front velocity (dS/dt) for the (-8 kV) case was at its lowest value, and it seemed that the melt front halted at this range. Figure 6.6 represents the transient thermal profile of the average surface temperature of the heater at a heater power input of 14.2 W. Similar trends were observed until EHD forces become significant and the rate of temperature rise for (-8 kV) case decreases over the 0 kV base case. The 0 kV base case was carried out for only 70 min because the heater surface temperature reached ≈ 110 ° C which is near to Acrylic glass softening temperature.

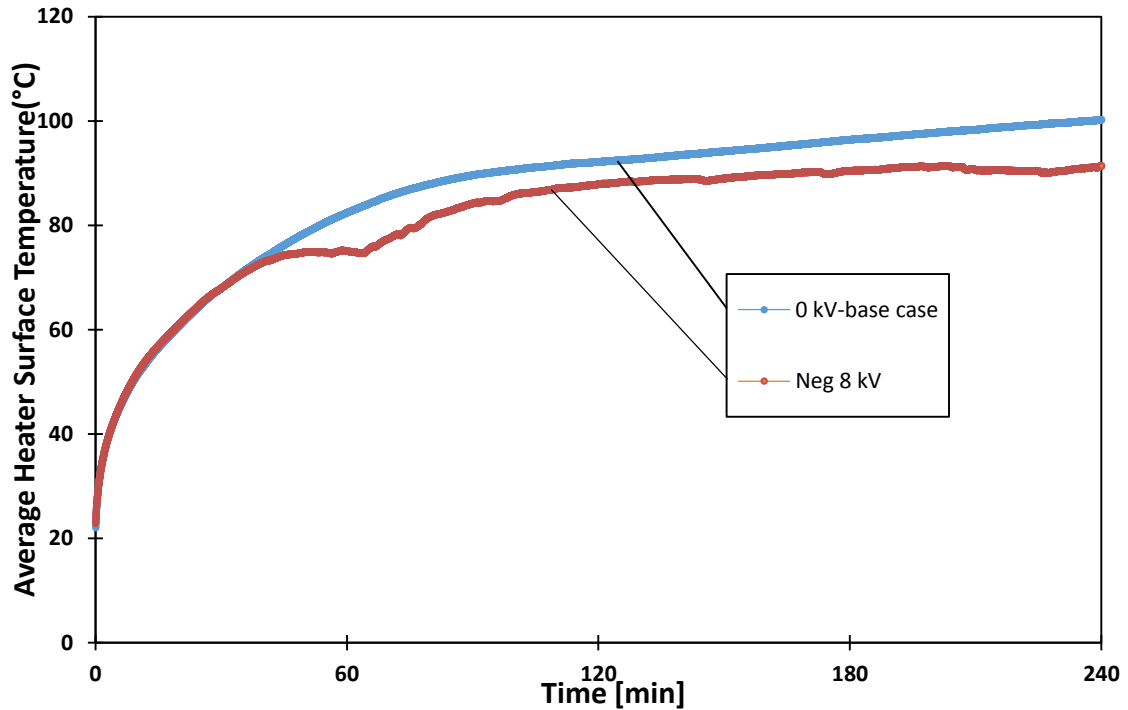


Figure 6.4 Heating surface average temperature variation with time for $Q = 10.4$ W, with and without an applied voltage (-8 kV)

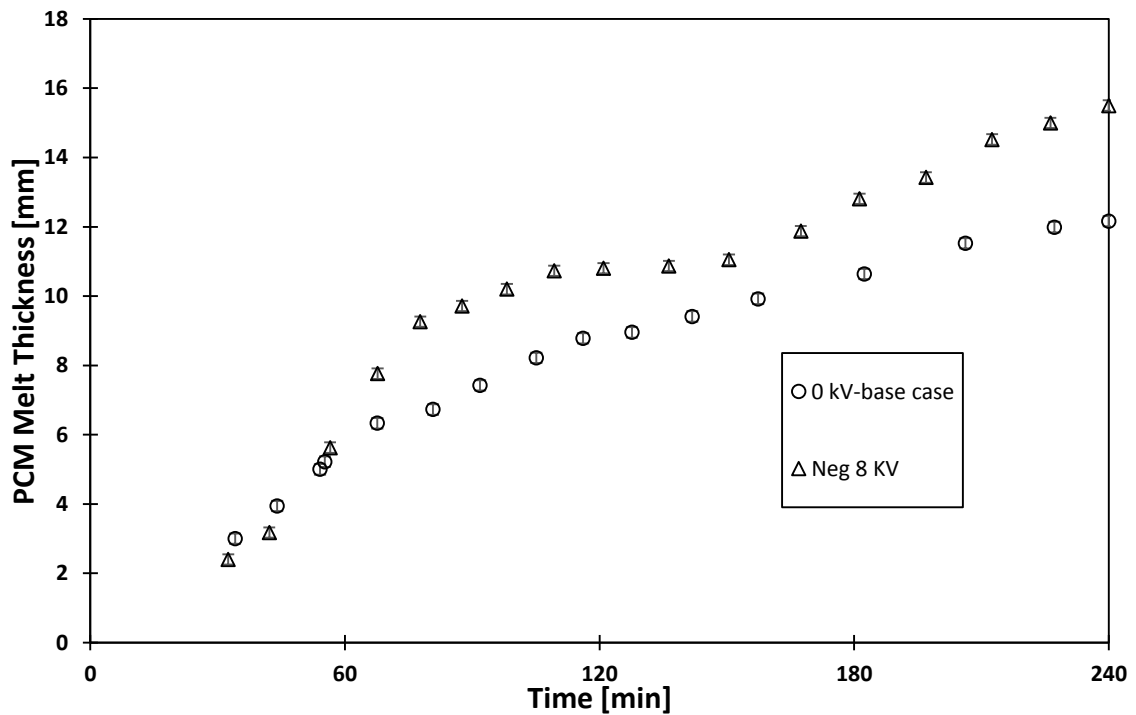


Figure 6.5 Melt front location (measured from the heating surface) with time for $Q = 10.4$ W, with and without an applied voltage (-8 kV)

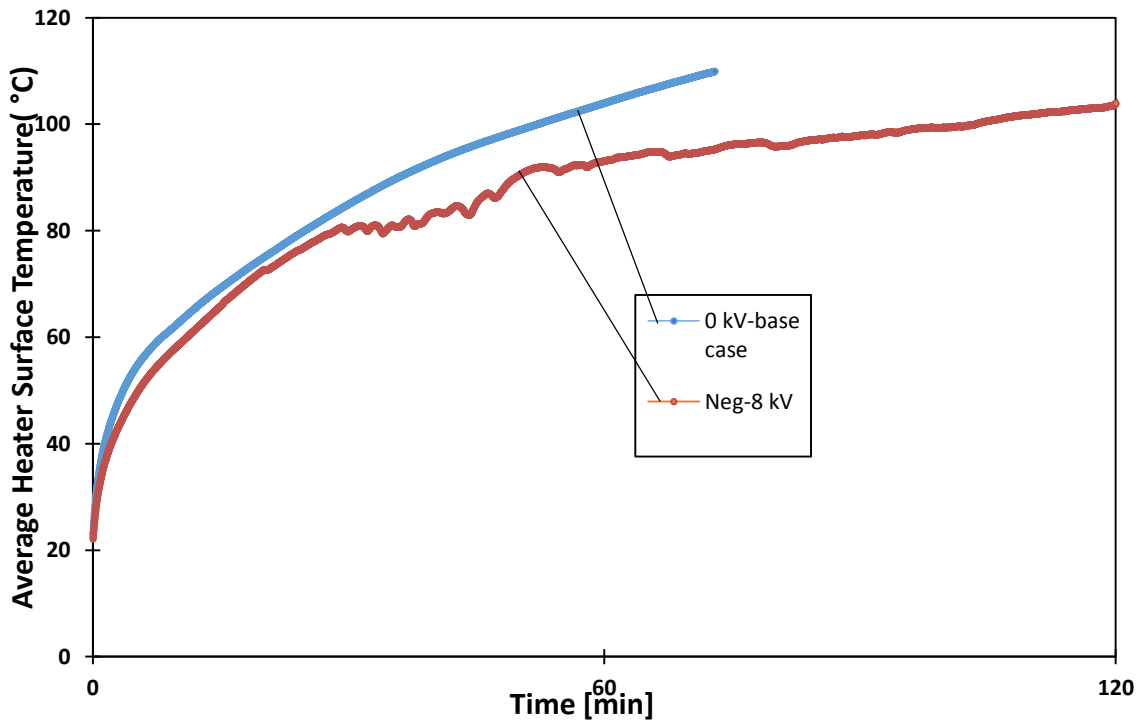


Figure 6.6 Heating surface average temperature variation with time for $Q = 14.2$ W, with and without an applied voltage (-8 kV)

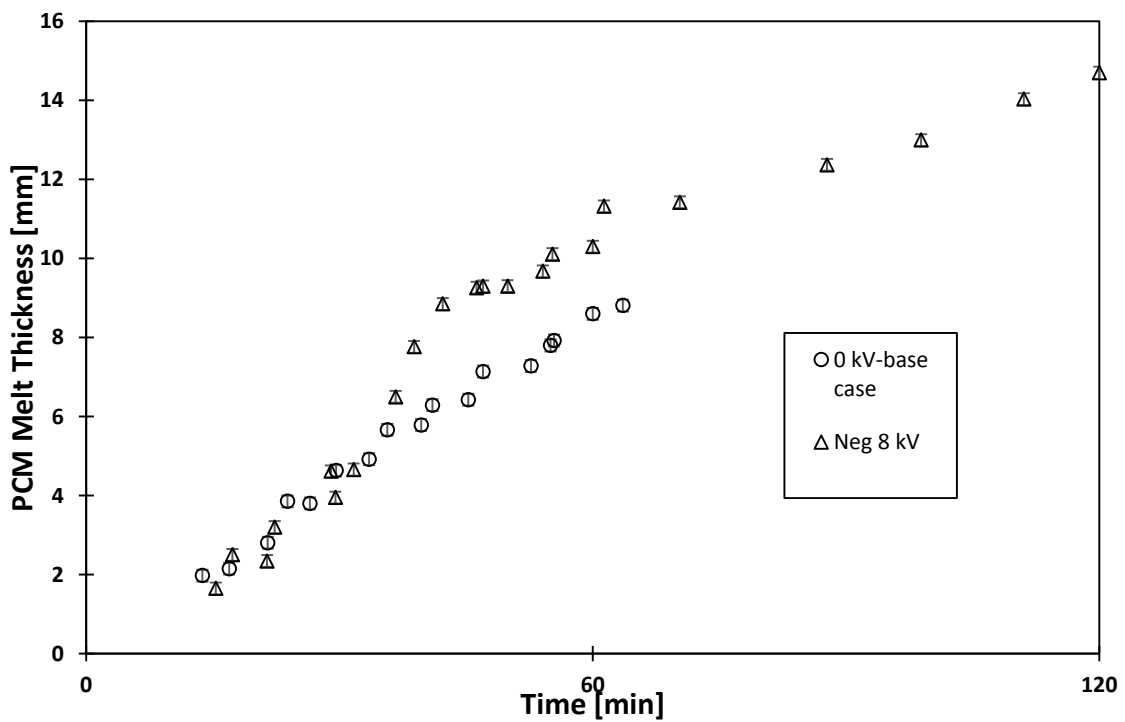


Figure 6.7 Melt front location (measured from the heating surface) with time for $Q = 14.2$ W, with and without an applied voltage (-8 kV)

The temperature of the copper sheet reached 110 ° C after 70 min while the (-8 kV) case reached 94.5 ° C. Figure 6.7 represents the melt front progress of the 14.2 W input heater power case. The results show that after 70 min, the melt thickness was 9.4 mm for the 0 kV base case and 11.2 mm for the (-8 kV) case, while after 2 hours, the melt thickness reached 14.7 mm for the (-8 kV) case. A similar behavior in melt front velocity to the 10.4 W case was observed. The melt front velocity (dS/dt) decreased significantly in the melt thickness range from 10 to 12 mm. The time taken to reach the centre line of the first row of electrodes, for the 0 kV case was ≈ 50 min as compared to ≈ 38 min for the (-8 kV) case. Table 6.1 summarizes the effect of applying (-8 kV) during melting of a paraffin wax on both, the time required to melt 7 mm of the PCM and the amount of molten PCM by the end of the experiment. Applying (-8 kV) can reduce the melting time of 7 mm of the PCM up to 40.5 % for 7.1 W heater input power and the amount of melt can be increased by 27.3 ± 5 %. The previous results from a reduction in melting time when compared to 0 kV base case and the increase in the PCM melt thickness suggest that EHD can be used as a promising active heat transfer enhancement techniques for a latent heat storage cell using a Paraffin wax as the PCM.

Table 6.1 Reduction in melting time and increase in the melt thickness caused by an applied voltage (-8 kV) for different heater power input values

Heater input Power (W)	% reduction in melting time by using EHD compared to 0 kV base case	% Increase in PCM melt thickness by using EHD compared to 0 kV base case
7.1	40.5 %	$27.3 \% \pm 5\%$
10.4	29.5 %	$29 \% \pm 3\%$
14.2	24 %	$19 \% \pm 3\%$

EHD power consumption was calculated by monitoring both the current and voltage readings recorded using an oscilloscope. The instantaneous EHD Power consumption is given by

$$P(t) = V(t) * I(t) \quad (6.4.)$$

The average EHD power consumption can be calculated by

$$P_{avg} = V_{avg} * I_{avg} \quad (6.5.)$$

Since only DC tests were examined through the scope of this project, the average voltage was 8 kV, and the average current was $\approx 22 \mu\text{A}$, this leads to an average EHD power consumption equal to 0.17 W which is equivalent to 1.2 % of the heat input power for the 14.2 W case and 2.4 % for the 7.1 W case.

6.2. Solid Extraction Phenomena

A high speed camera was used to focus on the interface (solid –liquid) and to see the effect of EHD forces on the mushy zone. Videos were captured at different levels for the melt front (above the first row of electrodes, centre line of the first row of electrodes and below the second row of electrodes) and at different lateral locations. A new phenomena was observed, which is Solid Extraction, where the solid dendrites or the equiaxed grains within the mushy zone were pulled from the mushy zone towards the electrodes. This phenomena could be one of the important EHD enhancement mechanisms in the latent heat thermal storage system tested.

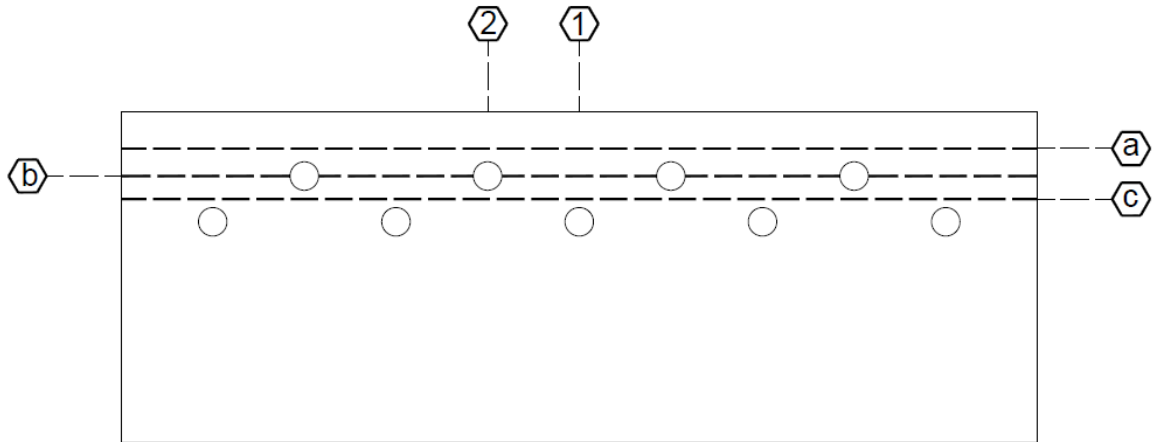


Figure 6.8 Schematic diagram for high speed imaging matrix

Figure 6.8 represents a schematic diagram for locations where the interface was captured. The horizontal dashed lines-labelled a, b and c -represent the different melt front locations and the vertical dashed grid lines-labelled 1 and 2- represent the different lateral locations across the melt front (interface) captured.

Figure 6.9 illustrates high speed imaging pictures taken by a high speed camera at 125 fps for the melt interface at location (a-1), along with illustrative cartoons. The images were taken at conditions corresponding to applying a high voltage of (-8 kV) at the electrodes while grounding the copper sheet. It can be seen from the pictures that the application of EHD led to extraction of the dendrites from the mushy zone upwards towards the molten PCM. While these dendrites were extracted upwards, they were melting due to migration to a higher temperature region (towards the heater). This had an effect of cooling down the molten phase which can be seen in all the comparative graphs between EHD and no EHD for the transient thermal profile of the average heater temperature.

These high speed images were taken for several different locations in order to clarify physics of EHD mechanisms. For location a2 which is a position coincides directly above one of the electrodes of the first row. From the images, it was found that EHD had no significant effect at this position and is similar to a normal melting where no solid extraction can be observed. The possible reasons for that are addressed in the next topic where numerical simulations were done to understand the static electric field distribution for different melt front locations.

Figure 6.10 represents the images captured at location b2, where the melt front level is at the level of the centre line of the first row of electrodes, while the lateral location is at the electrode where a part of the electrode can be seen at the left side of the images. It was observed that the mushy zone or the solid liquid interface is no longer flat around the electrode. This is due to the higher thermal conductivity of the electrodes (stainless steel) compared to the paraffin wax, which leads to a curved solid-liquid interface around the electrode. It was noticed that dendrites in the mushy zone were extracted towards the electrode and were getting smaller in size because of melting in their way. As the dendrites were approaching the electrodes, they slowed down and repelled away from the electrodes. This could be due to an increase in surface charge density caused by the dendrite melting and higher charge accumulation as the dendrite approaches the electrode (regions of higher electric field strength). This in turn leads to an increase of the electrophoretic force over the DEP (dielectrophoretic) force.

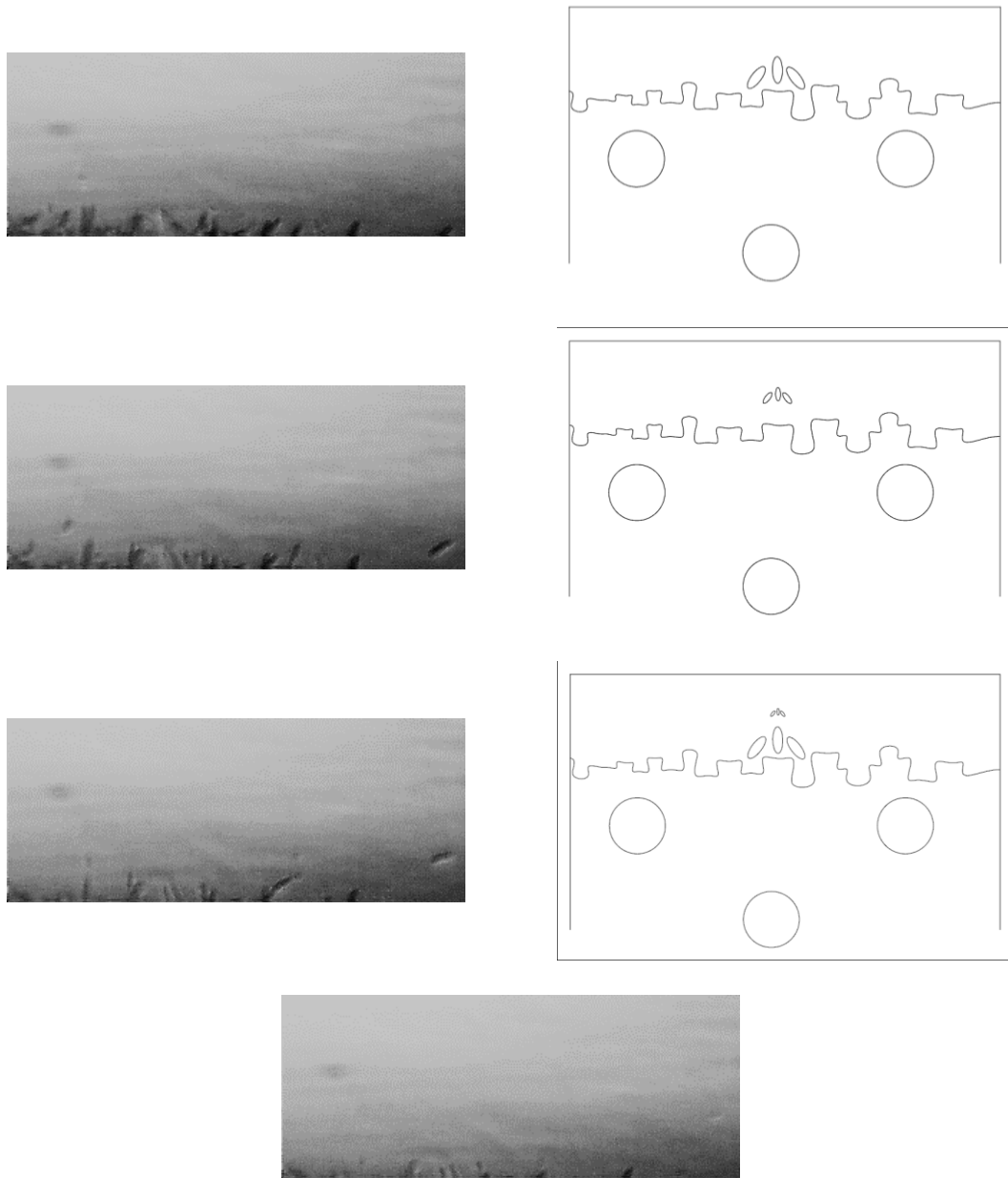


Figure 6.9 Solid - Liquid interface behaviour under an applied voltage of (-8 kV) at location (a1)-
time between frames 0.4 sec

This phenomenon was first reported by (Pohl, 1960) , where he stated that particles of a higher dielectric constant suspended in a lower dielectric medium and in a non-uniform electric field are being attracted by polarizing forces towards the higher electric field regions. The polarizing forces are being overcome gradually by the repulsive forces created by the accumulation of charges due to ionic conduction in the liquid.

For location b1 where the melt front level is at the centre line of the first row of electrodes and lateral position midway between electrodes, it was observed that solid extraction is still happening at this location and the dendrites are pulled up.

For the horizontal level c where the solid – liquid interface level is between the two rows of the electrodes, it was observed that there is almost no EHD effect at this location while applying (-8 kV) at both electrodes and having the copper sheet grounded, where no solid extraction had been observed.

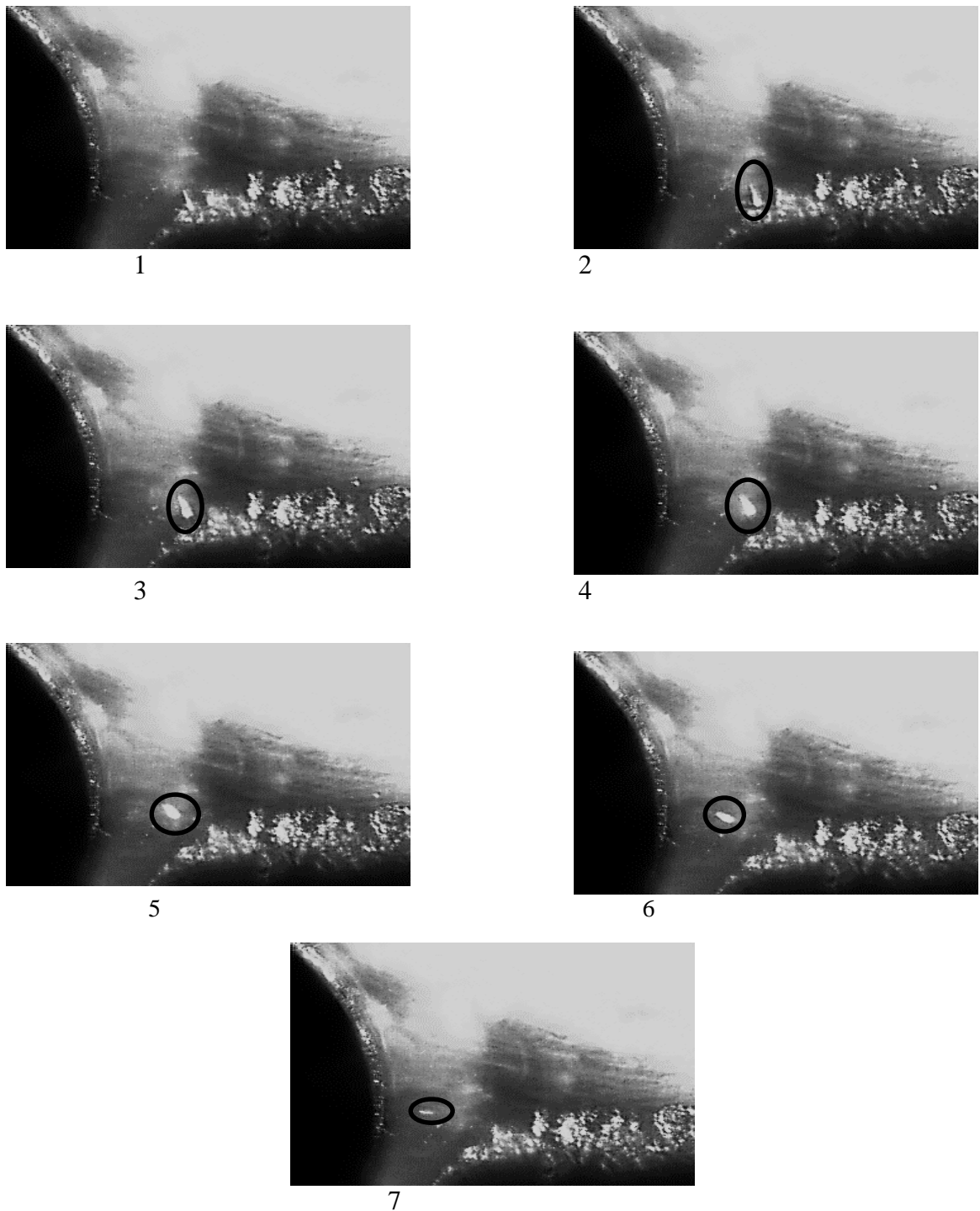


Figure 6.10 Solid - Liquid interface behaviour under an applied voltage of (-8 kV) at location (b2)-time between frames 0.08 sec

6.3. Heat Flux Effect and EHD Enhancement Factor

In this section, the effect of EHD on the melting process of a paraffin wax at different melt levels and different heat fluxes is quantified by using the EHD enhancement factor (EF). (Refer to section 5.3., equation 5.23.)

Within the scope of this thesis, only (-8 kV) is tested for EHD melting. In this case the enhancement factor can be expressed as

$$EF = \frac{\left(\frac{dS}{dt}\right)_{(-8\text{ kV})}}{\left(\frac{dS}{dt}\right)_{0\text{ kV}}} \quad (6.6.)$$

To evaluate the melt front velocity at different melt levels and different heat fluxes, curve fitting is performed for the experimental results of the temporal profile of the melt front location. [Refer to Figure 6.12, Figure 6.15 and Figure 6.18]- (dashed lines represent the 95 % confidence bands in curve fitting).

The melt front velocity is calculated by differentiating the curve fit equation of the melt front temporal profile for both the (-8 kV) case and the 0 kV base case. For the sake of increasing the accuracy of the curve fitting for (-8 kV) case, it is performed only for data points after the onset of EHD enhancement. The onset of EHD enhancement is estimated from the transient thermal profile for the average heating surface temperature, where a deviation between the 0 kV and (-8 kV) is observed. In case of constant heat flux boundary condition, any increase or decrease in the melt front velocity $\left(\frac{dS}{dt}\right)$ value will indicate a corresponding decrease or increase respectively in the thermal resistance corresponding to a given a melt thickness. [Refer to equation (6.2.)]

Figure 6.12 and Figure 6.13 represent the melt front velocity and the EHD enhancement factor for a power input of 7.1 W respectively. For the 0 kV case the only mode of heat transfer is heat conduction because of the directional downwards melting forming a thermally stratified liquid zone which will prevent natural convection effects. The decreasing linear relationship between the melt front velocity and the melt thickness for the 0 kV base case is due to the increase of heat conduction resistance with melt thickness. The melt front velocity for the (-8 kV) case is higher than that for the 0 kV base case and decreases as melt thickness increases. Figure 6.13 represents the EHD enhancement factor (EF) for a heater input power of 7.1 W at different melt thickness. The EF was 6.3 at melt thickness of 5 mm and increased till it reached 12.5 at melt thickness of 8 mm. This high uncertainty level is mainly because of the relatively low melt front velocity at high melt thickness for the 0 kV case [≈ 0.003 mm/min].

Melt front velocity for heater power input of 10.4 W at 0 kV base case and (-8 kV) is shown in Figure 6.15. A similar trend for the melt front velocity to the 7.1 W heat input was observed for the 0 kV base, where the melt front velocity decreases linearly with an increase of the melt thickness. For the (-8 kV) case, the melt front velocity decreases with an increase of the melt thickness until it reaches its minimum at $S \approx 10.5$ mm and then it increases again up to $S \approx 13$ mm and then decreases again. In Figure 6.16, it is shown that the EHD enhancement factor for 10.4 W heater input power is almost constant at value ≈ 6 until $S \approx 8$ mm and then decreases significantly with the increase of melt thickness till it reaches its minimum at $S \approx 10.5$ mm to values lower than 1 indicating a negative EHD effect compared to a 0 kV case.

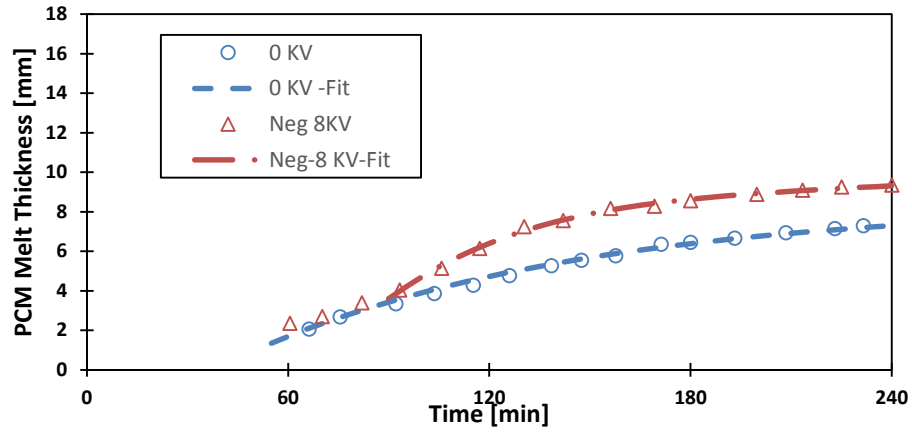


Figure 6.11 Curve fitting for melt front location (measured from the heating surface) with time for $Q = 7.1$ W

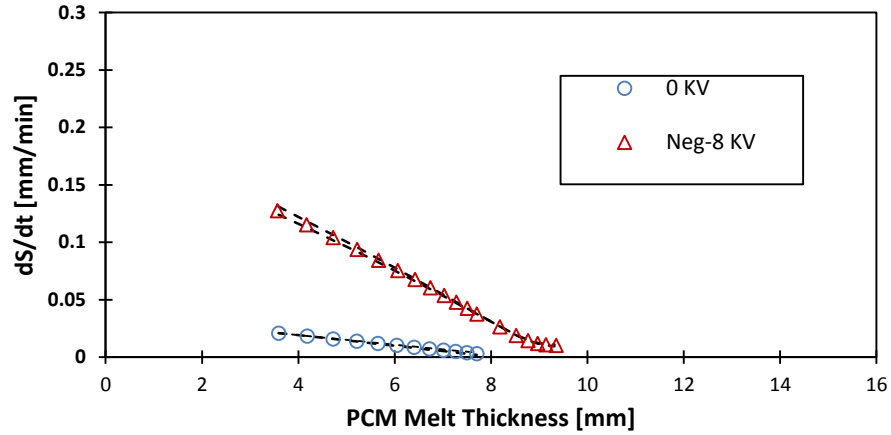


Figure 6.12 Melt front velocity at a given melt thickness for $Q=7.1$ W

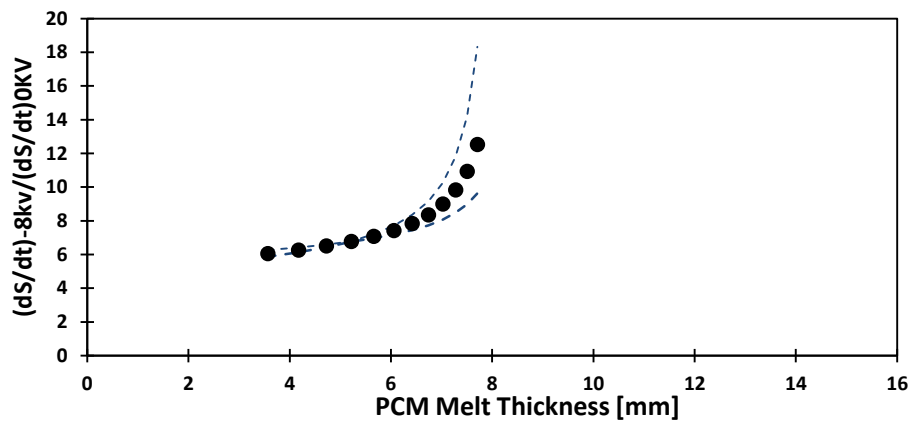


Figure 6.13 EHD enhancement factor (EF) at a given melt thickness for $Q=7.1$ W

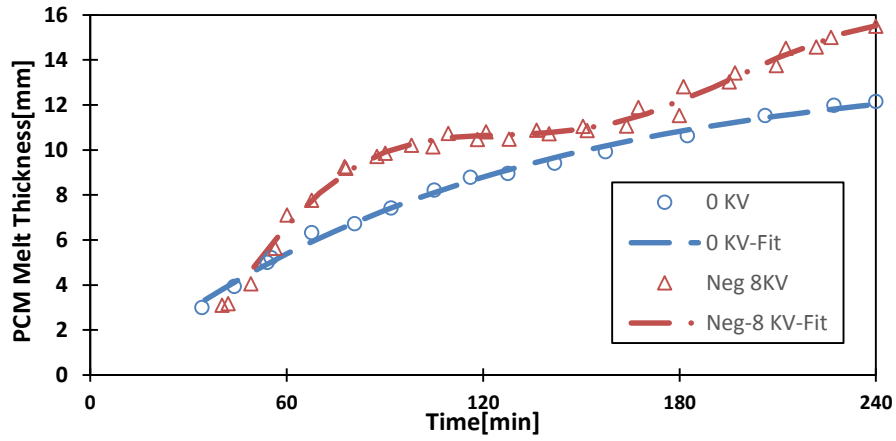


Figure 6.14 Curve fitting for melt front location (measured from the heating surface) with time for $Q = 10.4 \text{ W}$

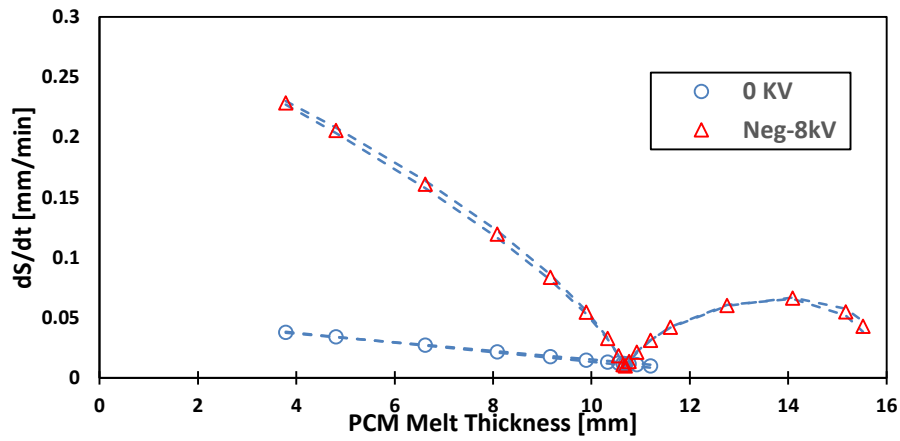


Figure 6.15 Melt front velocity at a given melt thickness for $Q=10.4 \text{ W}$

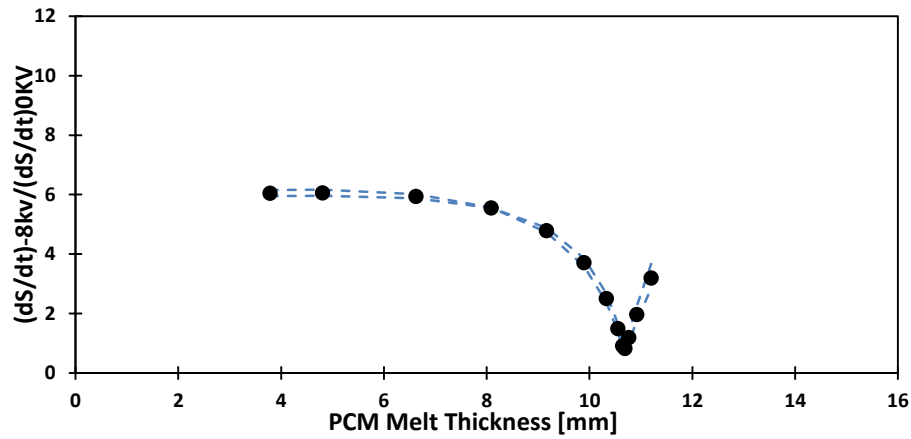


Figure 6.16 EHD enhancement factor (EF) at a given melt thickness for $Q=10.4 \text{ W}$

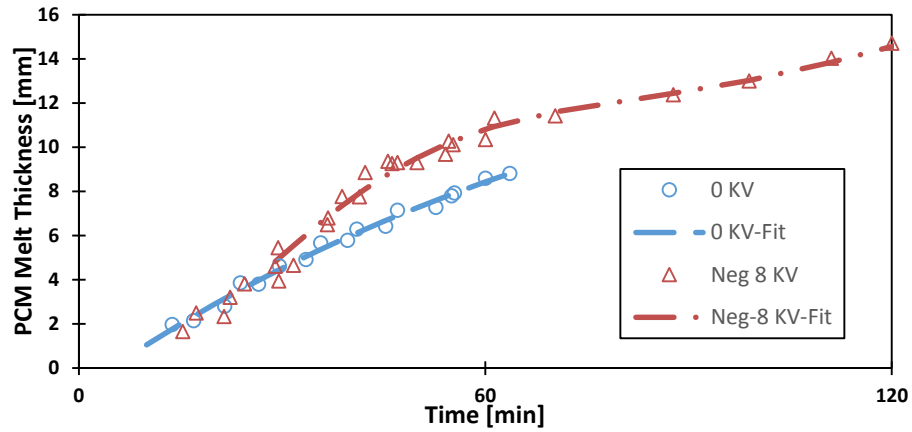


Figure 6.17 Curve fitting for melt front location (measured from the heating surface) with time for $Q = 14.2 \text{ W}$

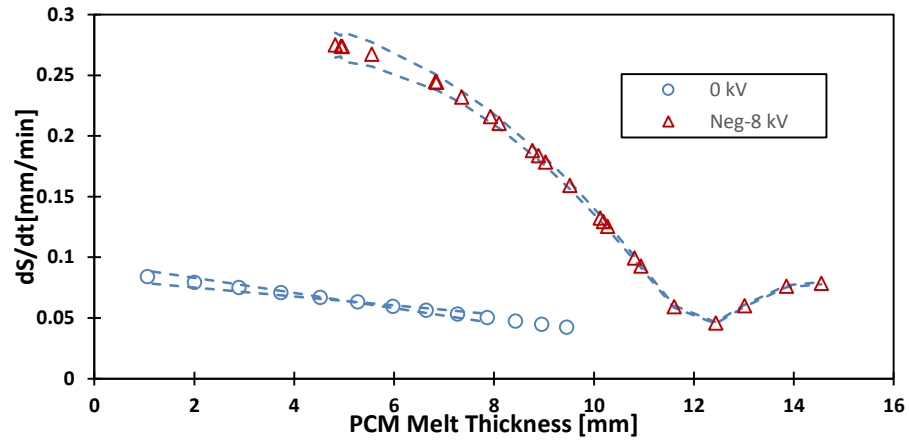


Figure 6.18 Melt front velocity at a given melt thickness for $Q=14.2 \text{ W}$

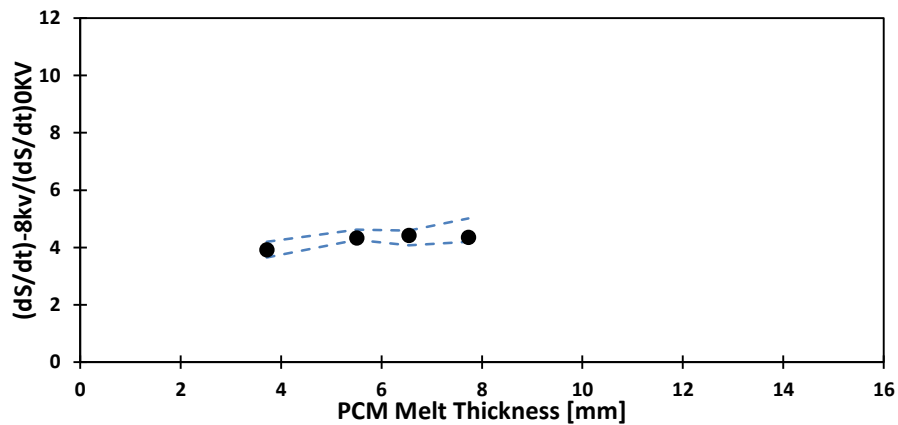


Figure 6.19 EHD enhancement factor (EF) at a given melt thickness for $Q=14.2 \text{ W}$

This is mainly because of the absence of the EHD dendrite extraction at this region leaving heat conduction to become again the dominant mode of heat transfer. However, the heating surface temperature is lower than the 0 kV (refer to Figure 6.4) which decreases the heat conduction driving potential leading to a decrease in the heat reaching the solid-liquid interface.

The results of the 14.2 W heat input melt front velocity and EF against melt thickness are shown in Figure 6.18 and Figure 6.19 respectively. Again the melt front velocity decreases linearly with the increase of the melt thickness for 0 kV case and a non-linear decreasing relationship for the (-8 kV) case reaching its minimum at $S \approx 12$ mm and then increased further again until $S \approx 14$ mm and decreased again after that. For the EF it was calculated up to $S \approx 9.2$ mm because the 0kV had reached a high temperature close to the softening point of acrylic glass and the experiment had to be terminated. The average EF is approximately constant at 4.2 for a heat input of 14.2 W from Figure 6.19 .

The heat flux effect on EHD enhancement factor is summarized in Figure 6.20. The EF decreases with an increase of the input power (heat flux) at any melt thickness. The EF is almost constant until melt thickness $S \approx 8$ mm for the 10.4 and 14.2 W heater power input cases, while for the 7.1 W case the EF showed an increase with the increase of the melt thickness. The decreasing relationship between the EF and the heat flux magnitude could be due to two different reasons. The first reason is that at lower heat fluxes, the melt front velocity becomes lower which gives relatively more time for heat to diffuse in the solid domain leading to a thicker mushy zone. Thicker mushy zones could allow an easier dendrites extraction. The second reason is that lower heat fluxes are associated with lower

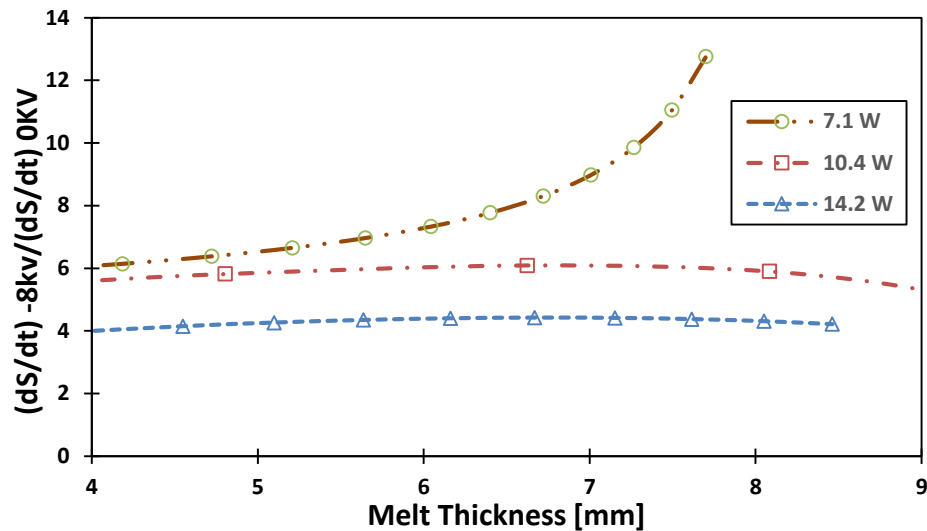


Figure 6.20 Variation of EF with melt thickness for different heat input values

temperatures, which means lower opposing buoyancy force for any induced EHD body forces acting on the liquid bulk.

6.4. Numerical Methodology

A two dimensional numerical model was developed to help provide a physical understanding of EHD effect on heat transfer enhancement in the latent thermal storage system under investigation. The electrostatic field distribution inside the paraffin wax cell was solved numerically using a commercial finite element software COMSOL. The results from the numerical simulations were used to analytically estimate the interfacial forces at the solid-liquid interface for different melt levels. The numerical model was also used to model the body forces on an ellipsoid particle suspended in a non-uniform electric field, to understand the trajectory of the extracted dendrites.

The governing electrostatic equations are given by the following equations, where Gauss's law can be expressed as

$$\nabla \cdot \bar{D} = \rho_e \quad (6.7.)$$

If the dielectric fluid is isotropic, linear and homogenous then the electric field displacement will be given by

$$\bar{D} = \epsilon \bar{E} \quad (6.8.)$$

By substituting in Gauss's law

$$\nabla \cdot \bar{E} = \frac{\rho_e}{\epsilon} \quad (6.9.)$$

Since the electric current is very small, it can be assumed that there is no change in magnetic field, and applying Faraday's law of induction

$$\nabla \times \bar{E} = -\frac{\partial \bar{B}}{\partial t} = 0 \quad (6.10.)$$

And since Faraday's law showed that the curl of the electric field is equal to zero, this means that the electric field can be expressed by a gradient of a scalar quantity, which is the electric potential (Voltage)-V

$$\bar{E} = -\nabla V \quad (6.11.)$$

And by substituting back in Gauss's law

$$\nabla^2 V = -\frac{\rho_e}{\epsilon} \quad (6.12.)$$

For the numerical simulations it was assumed that there is no space and surface charges within the fluid, so it can be simplified to the Laplace equation

$$\nabla^2 V = 0 \quad (6.13.)$$

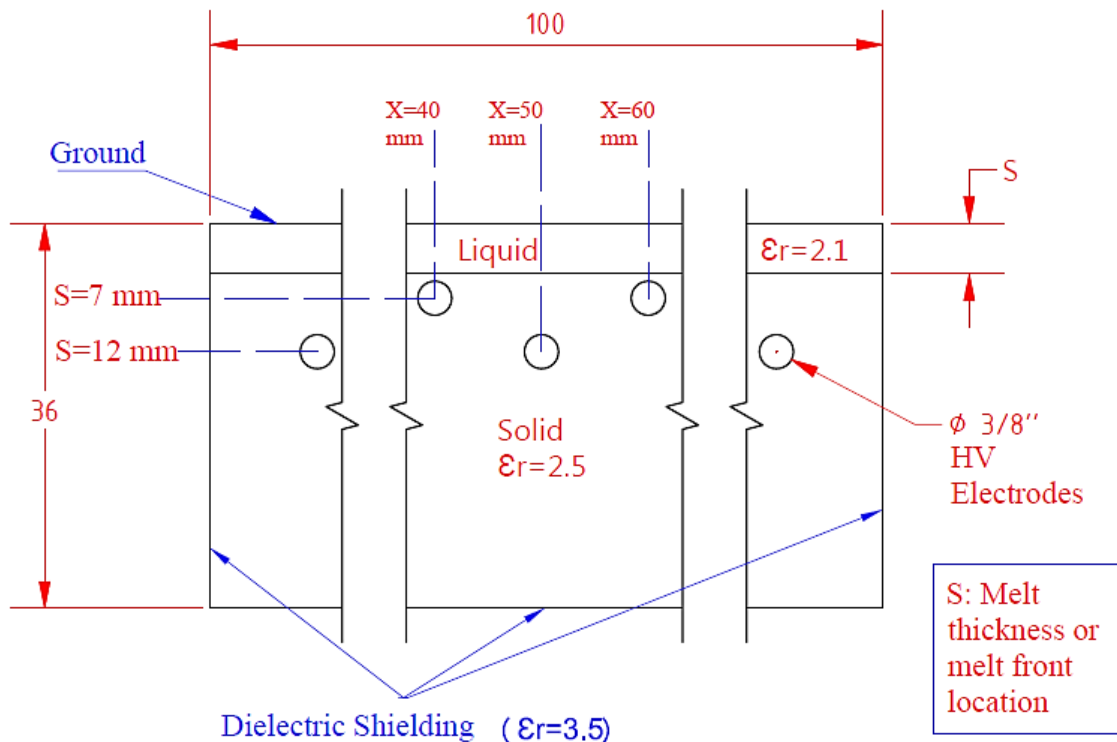


Figure 6.21 Electrode geometry and the solid and liquid domain for the numerical simulation

The numerical simulations were performed for a 2D cross sectional geometry with the same dimensions as the experimental facility. The working fluid is paraffin wax but modeled as 2 different materials with different dielectric constants to represent the solid and the liquid phase, where the dielectric constant for the liquid phase was 2.1 and for the solid was 2.5.

The details of the numerical domain and the applied boundary conditions are shown in Figure 6.21.

The enclosing boundaries for the domain (acrylic) were modeled as a dielectric shielding boundary condition, with a relative dielectric constant equal to 3.5 and a thickness of 6 mm, all the 9 electrodes were given a voltage terminal boundary condition of an applied

voltage of 8000 V, a grounded boundary condition was set for the top copper sheet. The melt front location (s) was measured from the bottom of the copper sheet.

6.4.1. Electric Field Distribution

The electric field distribution diagrams [Figure 6.22] were plotted using the most representative section of the numerical domain, which extends from $X=40$ mm to $X=60$ mm (Refer to Figure 6.21). In Figure 6.22, the electric field distribution was plotted for five different melt front locations (S). In case of $S=4$ mm, where the melt front was above all the electrodes, the lowest electric field in the liquid (molten) phase happened at the solid-liquid interface at a lateral position corresponding to $X=50$ mm. The highest electric field in the liquid phase was just above any of the upper electrodes ($X=40$ and 60 mm). For any lateral location X , the electric field in the liquid phase decreased gradually as it approached the copper sheet. For $S=7$ mm as in Figure 6.22b, where the melt front level is at the centre line for the first row of electrodes, the lowest electric field in the liquid phase is at the centre between the two upper electrodes but it was higher than the value at part (a), the highest electric field is at the upper half of the upper electrodes and gradually decreasing towards the grounded copper sheet. For location (c), where the melt front location level is between the centre line of the two electrodes $S=9.5$ mm, the electric field in the liquid phase still has the highest values at the upper halves of the upper electrodes which is consistent for all cases analyzed. In case (c) at the solid-liquid interface, the electric field intensity is high at regions below the upper electrodes and above the lower ones and relatively lower between

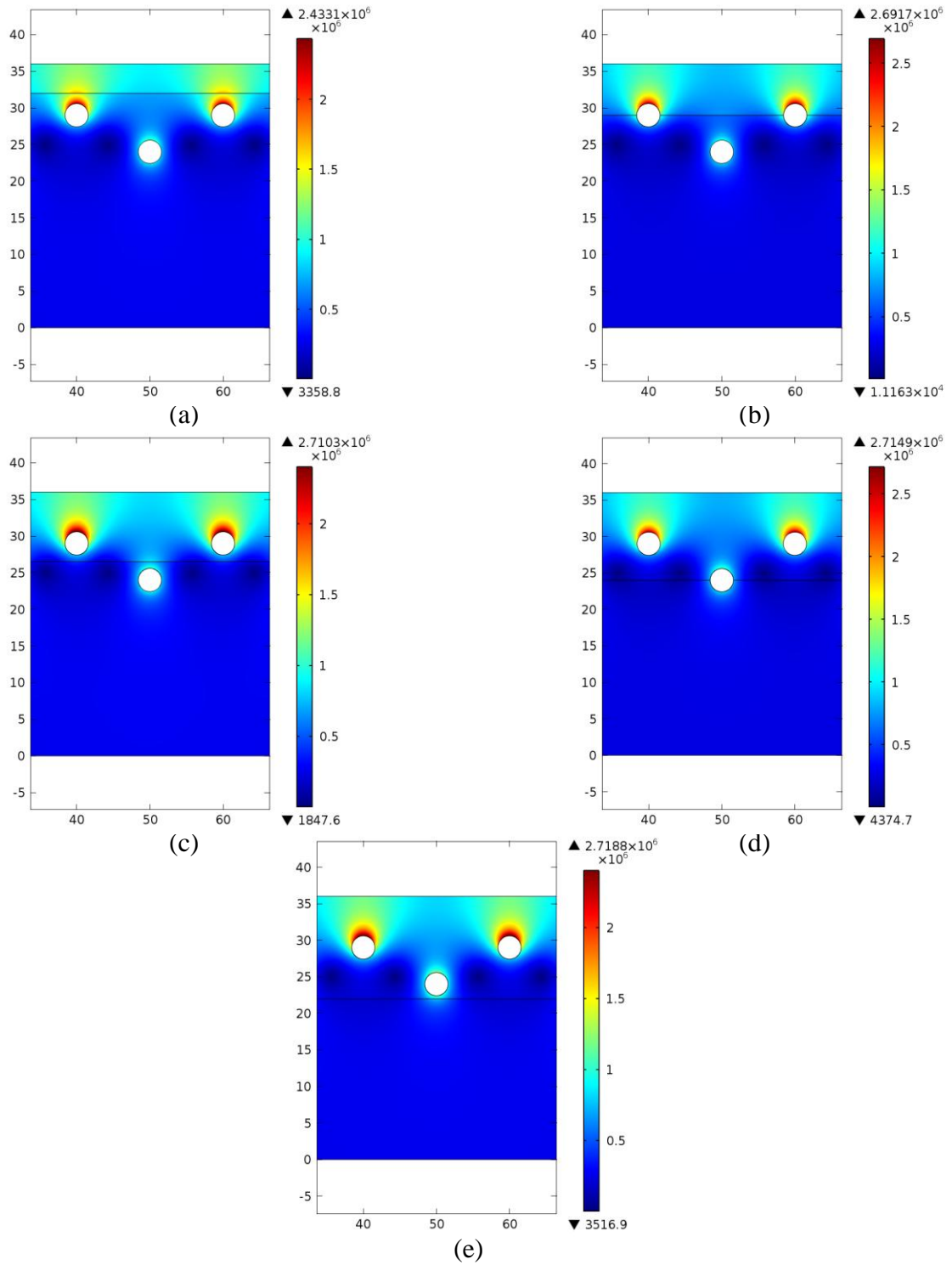


Figure 6.22 Two dimensional electric field distribution at (a) $S=4$ mm and (b) $S=7$ mm (c) $S=9.5$ mm (d) $S=12$ mm (e) $S=14$ mm

every each following upper and lower electrode. The electric field intensity at the solid-liquid interface has its highest value above the lower electrodes. At location (d), where the melt front location was at centre line level for the lower electrode, $S=12$ mm, the highest electric field at the solid –liquid interface is around the lower electrode. A similar trend is observed at location (d) where the highest electric field intensity at the solid-liquid interface is just below the lower electrodes.

6.4.2. Interfacial and Particle Attraction Forces Evaluation

To help understanding the EHD effect and the mechanism of enhancement, the interfacial forces on the solid-liquid interface were evaluated using the interfacial electric field distribution established in the numerical models. The extracted particles (dendrites) were treated as suspended particles of a high dielectric constant in a lower dielectric constant medium, to predict the trajectory of the solid material once extracted from the mushy zone.

6.4.2.1. Interfacial Forces Evaluation- (Extraction Forces)

As a first step for evaluating the interfacial forces acting on the solid-liquid interface, a free of charges interface will be assumed. Free of charge interface, will imply a continuous displacement electric field across it.

$$D_{1N} = D_{2N} \quad (6.14.)$$

$$\varepsilon_1 E_{1N} = \varepsilon_2 E_{2N} \quad (6.15.)$$

The result is that the material with higher dielectric constant will have a lower electric field magnitude than the one with the lower dielectric constant, which means at the interface the electric field intensity at the liquid side will be higher than that at the solid side as shown in the previous section in Figure 6.22 for the electric field distributions. This jump in the electric field magnitude is due to the discontinuity in the dielectric constant which leads to high polarization forces acting on the surface of discontinuity (solid-liquid interface) which is against the gravitational forces in this experimental set up. This interfacial traction forces per unit area in case of free charge interface had been estimated by (Stratton, 1941) and (Scaife, 1989), as

$$t = \frac{\epsilon_0}{6} \left\{ \frac{1}{\epsilon_2} [\epsilon_1^2 \epsilon_2^2 + 4\epsilon_1^2 \epsilon_2 - 6\epsilon_1 \epsilon_2^2 - 3\epsilon_1^2 + 2\epsilon_1 + 2] E_{n1}^2 + [\epsilon_2(\epsilon_2 - 2) - \epsilon_1(\epsilon_1 - 2)] E_{t1}^2 \right\} n_2 \quad (6.16.)$$

Based on equation (6.16.) when $\epsilon_2 < \epsilon_1$ then the maximum traction forces will be when the electric field has only a normal component on the interface and the tangential component is equal to zero. This traction force is always perpendicular to the surface as it had the same direction as $\nabla \epsilon$. (Refer to Figure 6.23)

By substituting in equation (6.16.) by $\epsilon_1 = 2.5$ and $\epsilon_2 = 2.1$ which are the values for the solid and liquid paraffin wax dielectric constants, this gives

$$t = \frac{\epsilon_0}{6} \{1.029762 E_{n1}^2 - 1.04 E_{t1}^2\} n_2 \quad (6.17.)$$

Assuming n_2 is the normal vector to the solid-liquid pointing from the solid zone (1) towards the liquid zone (2), and the normal and tangential electric field component, E_{n1} and E_{t1} , are calculated at the solid side just below the interface.

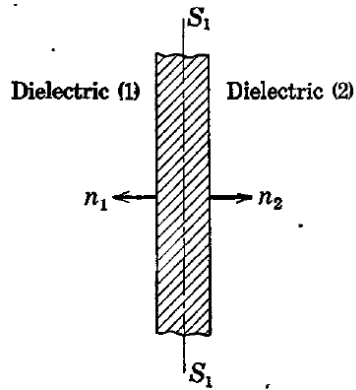


Figure 6.23 Section of a transition layer separating two dielectric media, (Stratton, 1941)

Due to the symmetry in the electric field distribution, the extraction forces were evaluated at a 20 mm section, from $X=40$ to $X=60$ mm [Refer to Figure 6.21]. Figure 6.24 shows the interfacial extraction force for 4 different melt front locations ($S= 2, 4, 5$ and 6 mm). The two vertical dashed black lines represent the boundaries of the two upper electrodes. From the graph, it shows that as long as the solid-liquid interface is above the upper electrodes (S from 0 to 5 mm) the interfacial force is always positive (i.e. extraction), where the lowest value is at the midline (centre line of a lower electrode) and the maximum value at the centre line of an upper electrode. However, as the melt thickness increases the extraction force value at the midline decreases while the extraction force at the region above upper electrode increases. This is due to the increase of the normal component of the electric field strength at the solid-liquid interface as the interface is approaching the upper electrodes. At $S=2$ mm, the extraction force per unit area was equal to 0.902 N/m^2 , for $S=4$ mm was equal to 0.74 N/m^2 and for $S=5$ mm the extraction force per unit area was equal to 0.7 N/m^2 .

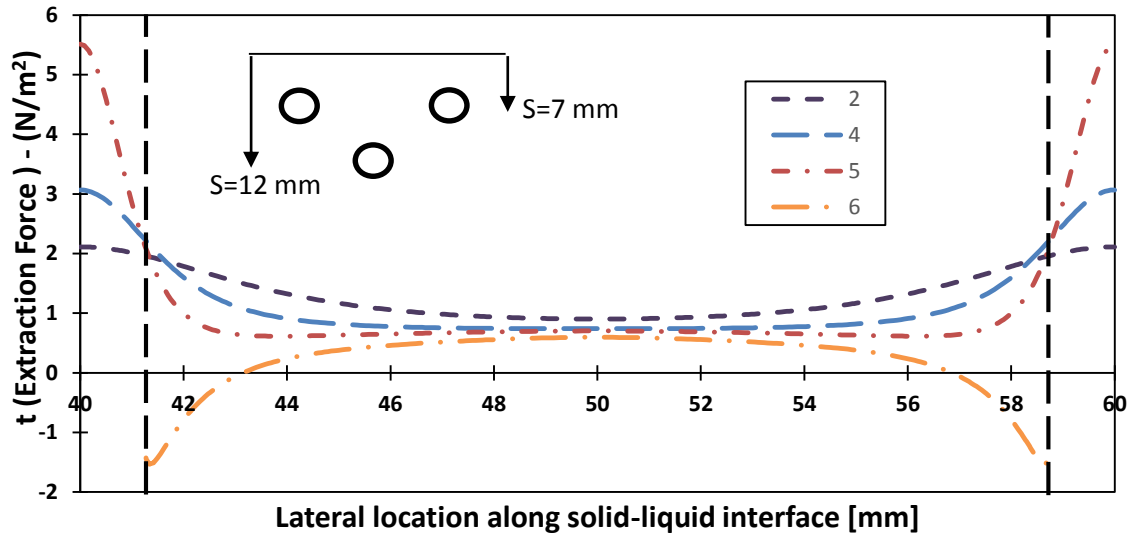


Figure 6.24 Extraction force distribution across the Solid -Liquid interface from X=40 to X=60 mm at different levels measured from the heater (S=2 mm to S=6 mm)

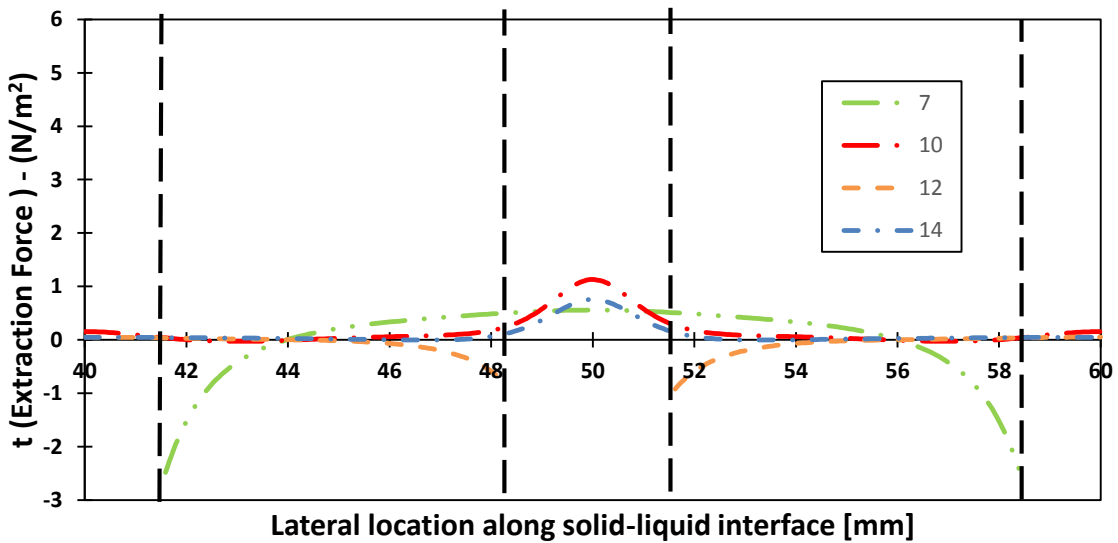


Figure 6.25 Extraction force distribution across the Solid -Liquid interface from X=40 to X=60 mm at different levels measured from the heater (S=7 mm to S=14 mm)

While the values of the extraction force per unit area at $X=40$ (centre line of the upper electrode) vary significantly with the melt front location.

As the melt front reaches the tip of the upper electrodes ($S=5.8$ mm) and further progresses down, the area of the interface that experiences positive extraction force (against gravity) decreases. The positive extraction forces at the solid-liquid interface are then around $x=50$ mm (centre line of lower electrode) and it becomes negative in regions around the upper electrodes for distances up to $1.5 d$. (Refer to Figure 6.24)

Figure 6.25 represents the extraction forces per unit area from $S=7$ mm to $S=14$ mm. As the melt thickness increases and passes the centre of the first row of electrodes ($S=7$ mm). The area of the solid-liquid interface, which experiences a positive extraction decreases and becomes almost zero everywhere except above the lower electrodes ($X=50$ mm) at $S=10$ mm and below the lower electrode for $S=14$ mm. When the melt front reaches the centre of the lower electrode at $S=12$ mm, almost no extraction is likely to occur as the predicted upward force is zero everywhere and a negative value around the lower electrode. This suggests that the polarization component of EHD forces acting on the solid-liquid interface will have a minimum effect between $S=10$ mm and $S=12$ mm and will result in low enhancement in this zone. Figure 6.26 represents a summary for the extraction forces per unit area previously evaluated and represented in Figure 6.24 and Figure 6.25 at different melt front locations for two different lateral positions at the solid - liquid interface. The first location corresponds to $X=40$ mm and the second location corresponds to $X=50$ mm.

For the first location ($X=40$ mm), the extraction force per unit area increases rapidly as the melt front progresses downwards until it touches the upper electrode and then the extraction

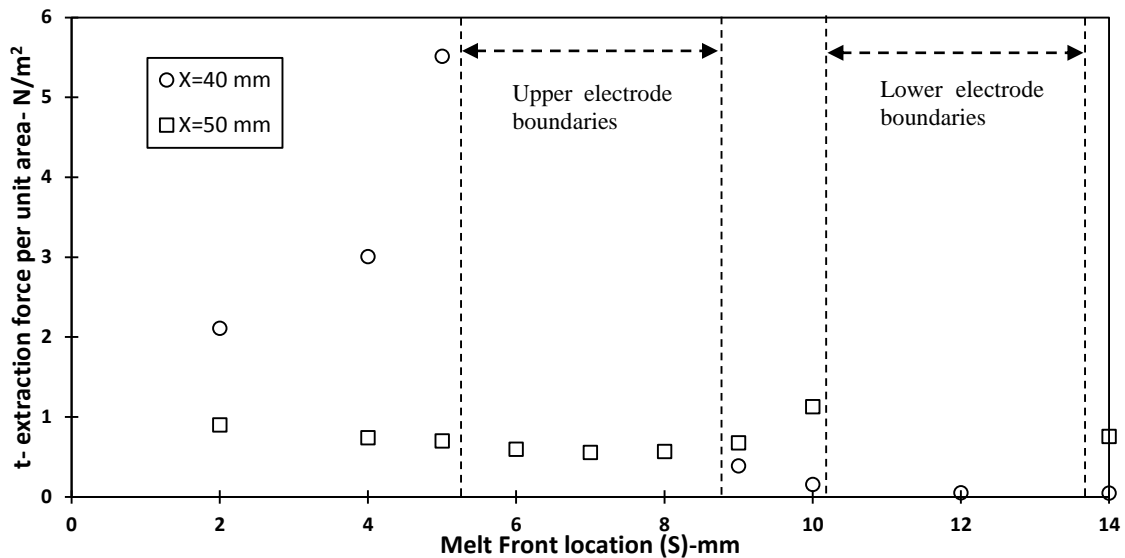


Figure 6.26 Summary of extraction forces per unit area at different melt front locations for two axial locations, $X=40$ mm (centre line of upper electrode) and $X=50$ mm (centre line of lower electrode)

force per unit area decreases after it passes the upper electrode and progresses further down. While for the second location ($X=50$ mm), the extraction force per unit area decreases almost linearly as the melt front progresses downwards. This linear decrease continues till $S \approx 8$ mm and then increases until the melt front touches the lower electrode and after it passes the lower electrode it decreases again. These results show an opposite trends in the behavior of the extraction forces, where at one location it is rapidly increasing as the melt front progresses downwards and in the other location it is decreasing linearly. Comparing the numerical evaluation for the extraction forces at the solid-liquid interface to the experimental results in section 6.3 and correlating it to the

EHD enhancement effect. It was shown in Figure 6.12, Figure 6.15 and Figure 6.18 that the melt front velocity for the (-8 kV) case decreases with the increase of the melt thickness which indicates that EHD enhancement effect is decreasing as the melt front progresses downwards. This trend agrees with the numerical results for the regions above the lower electrode ($X=50$ mm), where the EHD polarization forces that cause dendrites extraction at the interface decreases linearly with increasing the melt thickness. However, this doesn't agree with the numerical results for the regions above the higher electrodes ($X=40$ mm) [Figure 6.26]. Similarly, this mismatch between the experimental results and the numerical force evaluation at regions above the higher electrode ($X=40$ mm) was observed in the high speed imaging taken during the experiments. High speed imaging showed that there was no dendrites extraction happening at this region ($X=40$ mm). However, dendrites extraction was observed in regions above the lower electrode ($X=50$ mm) as shown in Figure 6.9. In the region between the two electrodes at $S=10$ to 12 mm, the numerical model evaluated the extraction forces to be almost zero everywhere at $S=10$ mm except for the region above the lower electrode and to be equal to zero everywhere and had negative values around the lower electrode for $S=12$ mm. The experimental results showed an agreement with that, where the lowest EHD enhancement effect was in this region (Refer to Figure 6.16. and Figure 6.19.). The high speed imaging in this region showed no dendrites extraction taking place, this agrees with the numerical evaluation for the extraction forces in this region except for the region above the lower electrode at $S=10$ mm.

Accordingly the polarization forces acting on the solid-liquid interface alone are not enough to explain the EHD enhancement effect and do not totally correlate with the high speed imaging taken for the PCM cell investigated or the experimental data for the melt front velocity. This means that there are still some effects which were not taken into account that may complete the understanding of the EHD physics happening inside the cell.

6.4.2.2. Particle Attraction Forces (DEP –dielectrophoretic) Evaluation

Another important factor in understanding the physics of the EHD enhancement and its role on the melting process of a paraffin wax LHTSS is what happens to the dendrite (solid particles) after the extraction. In this section an analysis is presented to elucidate whether the extracted dendrites from the mushy zone are encouraged to leave the mushy zone and migrate towards a hotter region increasing the interfacial area to melt faster or the suspended particles are repelled back towards the mushy zone.

The equation of motion of suspended particles relative to the solvent media due to the application of non-uniform electric field had been first derived by (Pohl, 1951) and called the phenomena “dielectrophoresis”. This phenomena has been used in many applications especially molecular biology where it was used for particle separation and discrimination as reviewed by (Gascoyne, et al., 2002).

In case of a perfectly insulating spherical particle of radius (a) and a dielectric constant ϵ_2 suspended in an insulating fluid medium of a dielectric constant ϵ_1 and under a non-homogenous electric field the dielectrophoretic (DEP) force acting on the particle as derived by (Pohl, et al., 1972)

$$F_{DEP} = 2\pi a^3 \frac{\varepsilon_1(\varepsilon_2 - \varepsilon_1)\nabla(E^2)}{\varepsilon_2 + 2\varepsilon_1} \quad (6.18.)$$

Equation (6.18.) implies that for a particle of higher dielectric constant than the surrounding medium, it will experience a positive DEP in the same direction as ∇E^2 meaning that it will be attracted towards the higher electric field regions. (Jones, 2005) evaluated the DEP on a prolate spheroid particle suspended in a fluid medium with its long axis a being positioned parallel to the axis of an axially symmetric non-homogenous electric field by

$$\bar{F}_{DEP} = \frac{2\pi ab^2}{3} \left[\frac{(\varepsilon_2 - \varepsilon_1)}{1 + \left(\frac{\varepsilon_2 - \varepsilon_1}{\varepsilon_1}\right) L_{II}} \right] \nabla E^2 \quad (6.19.)$$

where the parallel depolarization factor L_{II} in terms of $\gamma = a/b$ is given by

$$L_{II} = \left[1 + \frac{3}{5}(1 - \gamma^{-2}) + \frac{3}{7}(1 - \gamma^{-2})^2 + \dots \right] / (3\gamma^{-2}) \quad (6.20.)$$

The electric field gradient was calculated at different melt front locations for tracing the particles of the suspended dendrites in the molten phase. The DEP magnitude was calculated by evaluating the extracted dendrite size from the high speed imaging taken before. The extracted dendrite is approximated as a prolate spheroid with semi-axis a, b & c where $a > b = c$. In the current analysis dendrite dimensions was estimated from the images as approximately $a \cong 70 \mu m$ and $b = c \cong 27 \mu m$. By substituting in equation (6.19.) and equation (6.20.) the values of the axis dimensions and the dielectric constants of the material, then

$$\bar{F}_{DEP} = 2.132 \times 10^{-14} \nabla E^2 \quad (6.21.)$$

This force was computed for different melt thicknesses and at the solid-liquid interface in order to estimate the polarization forces on the suspended dendrites once extracted. In Figure 6.27, the ∇E^2 normalized field vector in the molten liquid wax was plotted for different melt front locations. At $S=4$ mm (Figure 6.27a), the solid-liquid interface is above the upper electrodes and the normalized gradient field arrows shows that at the midline above the lower electrodes ($X=50$ mm) any suspended particle would be encouraged to migrate from the mushy zone and moves upwards towards the nearest upper electrode. However, above the upper electrode regions ($X=40$ and $X=60$ mm) any suspended particle will be forced back to the mushy zone, which had been observed in the high speed imaging at this location where no extraction of the dendrites was observed. At $S=7$ mm (Figure 6.27b), where the solid-liquid interface is at the centre of the upper electrode, it is observed that at the interface all the attraction forces on suspended particles were upwards and towards the nearest upper electrodes. When the interface is between the two levels of electrodes at $S=10$ mm (Figure 6.27c), the particles attraction forces are upwards directly under the upper electrodes, while above the lower electrodes any suspended particles will be forced back to the mushy zone. The high speed imaging showed no extraction anywhere along this location. At $S=12$ mm (Figure 6.27d), the gradient is similar to $S=10$ mm case where there is no upward attraction forces acting on the suspended particles except directly below the upper level electrodes. Finally at a location below all electrodes as $S=14$ mm, the upward attraction would occur only below the lower level electrodes.

As this interpretation is only based on the normalized field vector representation, to truly establish EHD enhancement at each melt front location, the forces acting on the particle must be balanced by 3 acting forces which are: the gravitational forces, the bonding forces of the dendrites to the mushy zone and the EHD interfacial forces, which is beyond the scope of the current study.

The important force component in the particle attraction forces in this case is the vertical-*Y*- component as it is the one responsible for helping the migration of the suspended

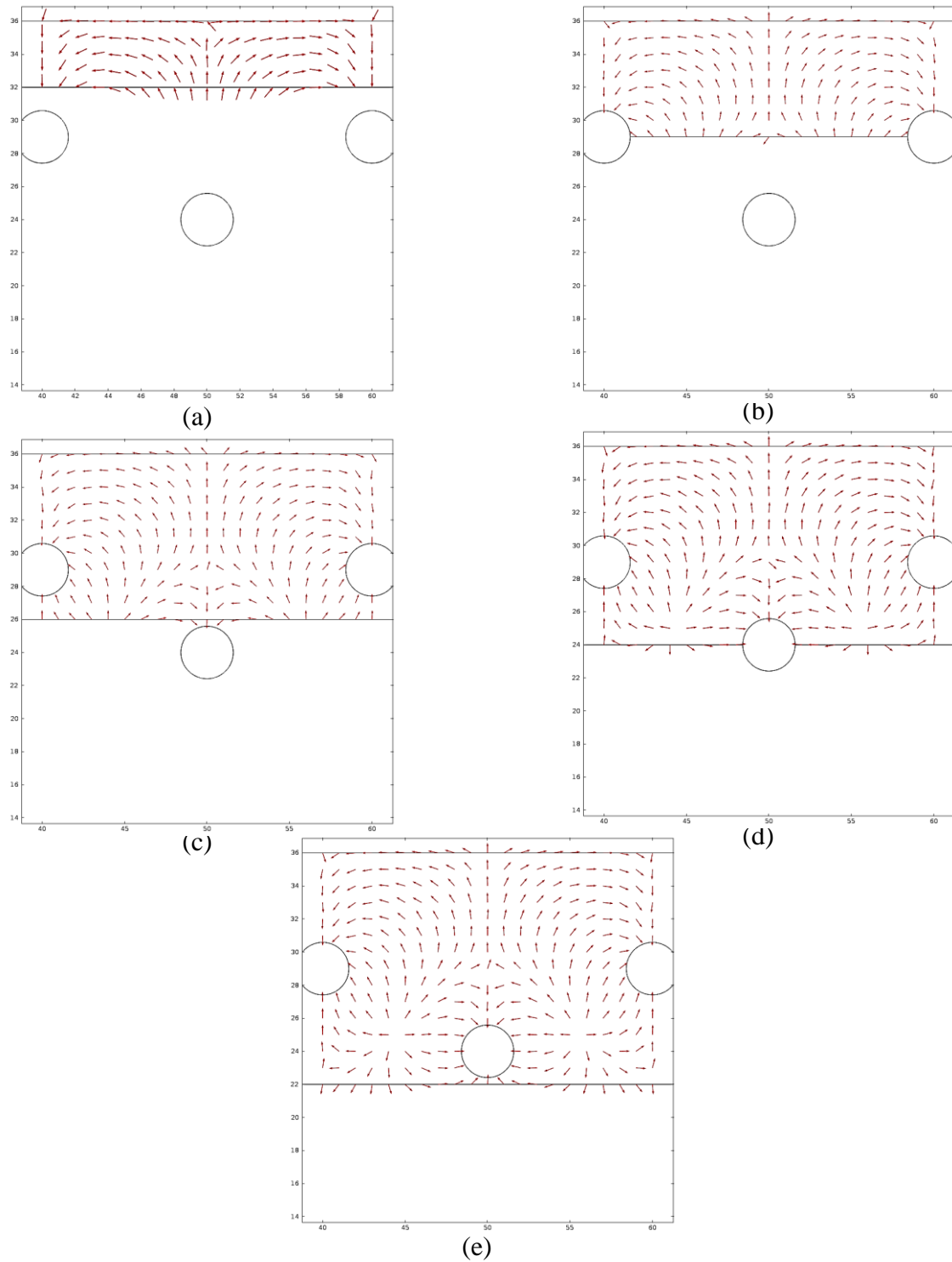


Figure 6.27 Two dimensional numerical representation of ∇E^2 vector field at (a) $S=4$ mm (b) $S=7$ mm (c) $S=10$ mm (d) $S=12$ mm (e) $S=14$ mm

particles away from the mushy zone or limit extraction from the mushy zone wither it is a positive or negative value. In Figure 6.28 the positive Y-component of DEP force was calculated at 4 different melt front locations ($S=2, 4, 5$ and 7 mm). For regions around the centre line of the lower electrode, at $X=50$ mm, the DEP forces acting on extracted particles will increase as the melt front progresses downwards from $S=0$ to 5.4 mm. As the melt front progresses downwards the area of the solid-liquid interface where the suspended particle will experience an upward force increases. Any suspended particle in regions above the upper electrode at $X=40$ and $X=60$ mm experience negative DEP force. This negative DEP will cause any extracted dendrites in this region to be repelled back towards the solid-liquid interface. This may explains the mismatch between the numerical evaluation for the interfacial extraction force in this region and the high speed imaging observing. The numerical evaluation for the extraction forces predicted large extraction forces which increase as the melt front progresses downwards (Refer Figure 6.24) but the high speed imaging in this region showed no extraction happening and the experimental results showed that the EHD effect is decreasing as the melt front progresses downwards (Refer Figure 6.12). This agrees with the predicted particle attraction forces evaluated here for this region, where the DEP force is opposing the interfacial extraction force which makes this region as inactive component for EHD enhancement.

In Figure 6.29 as the melt front progresses downwards and pass the upper electrodes, the DEP force decreases. For $S=10$ mm and at the axis of the lower electrodes ($X=50$ mm) the DEP force had negative values showing that any extracted dendrites in this region will be repelled back towards the solid- liquid interface. This also explains the mismatch

between numerical evaluation for the extraction interfacial forces at this region (Refer Figure 6.25) and what have been observed by the high speed imaging of no extraction happening at this region and the agreement with the experimental results of having the lowest EHD enhancement happening (Refer Figure 6.15). At a melt depth of $S=12$ mm there is almost no positive DEP through the solid-liquid interface and the positive values are around the electrode by a length ≈ 1 mm which agrees with the experimental results of low EHD enhancement region. As the melt proceeds and passes the lower electrodes the only positive values are just below the lower electrodes which agrees with the numerical evaluation for the extraction forces at this region (Refer Figure 6.25) and explains the increase in the EHD enhancement again (Refer Figure 6.15).

A Schematic diagram summarizing the results of the numerical simulation in evaluating the interfacial forces and the particle attraction forces (DEP) is presented in Figure 6.30.

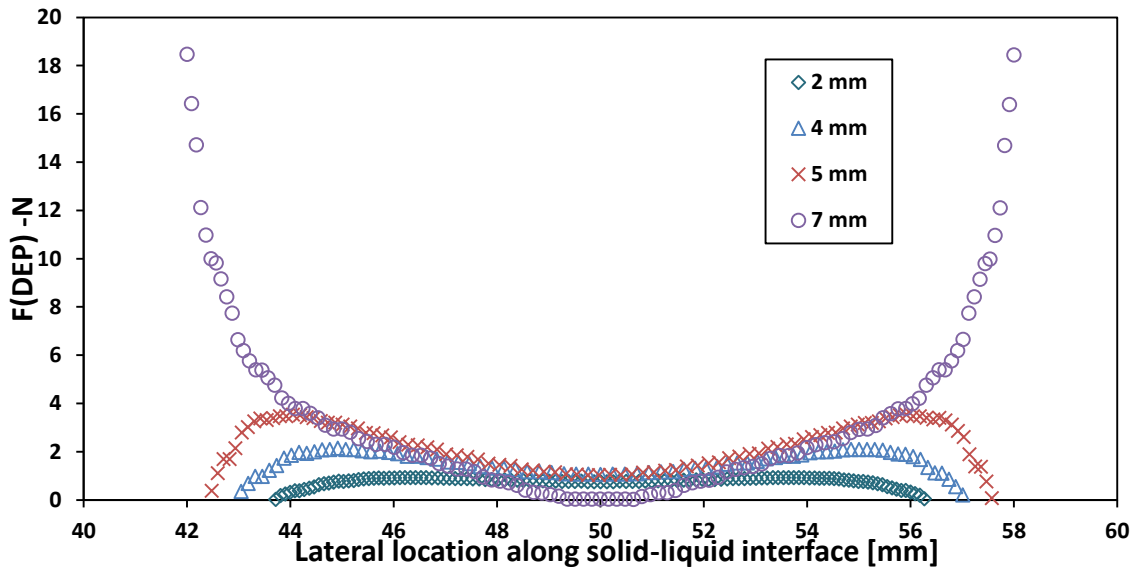


Figure 6.28 Particle attraction force distribution across the Solid -Liquid interface from X=40 to X=60 mm at different melt front locations. (S=2 mm to S=7mm)

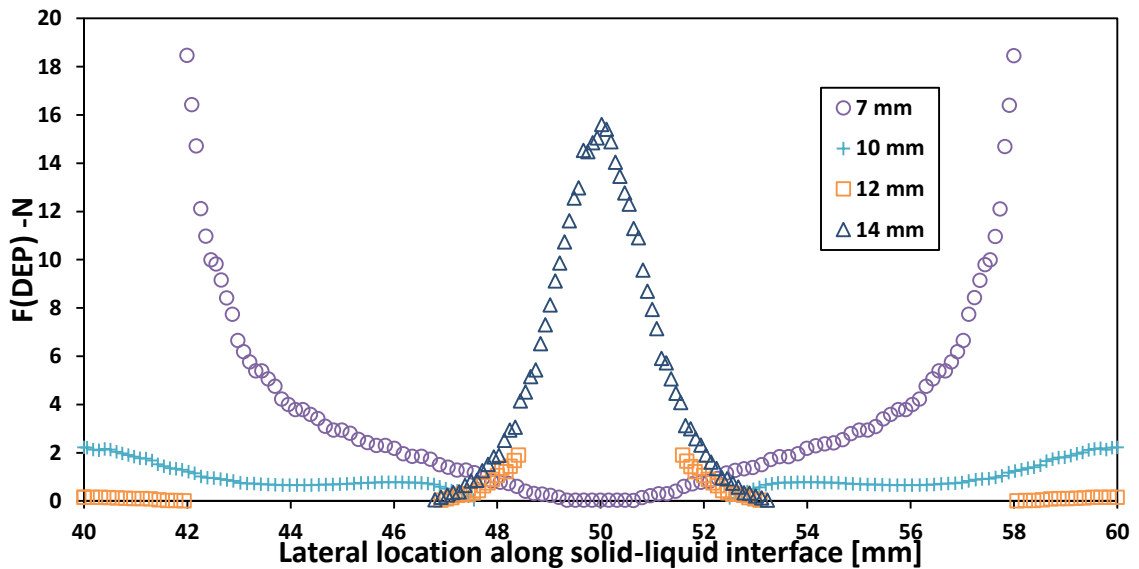


Figure 6.29 Particle attraction force distribution across the Solid -Liquid interface from X=40 to X=60 mm at different melt front locations (S=7 mm to S=14mm)

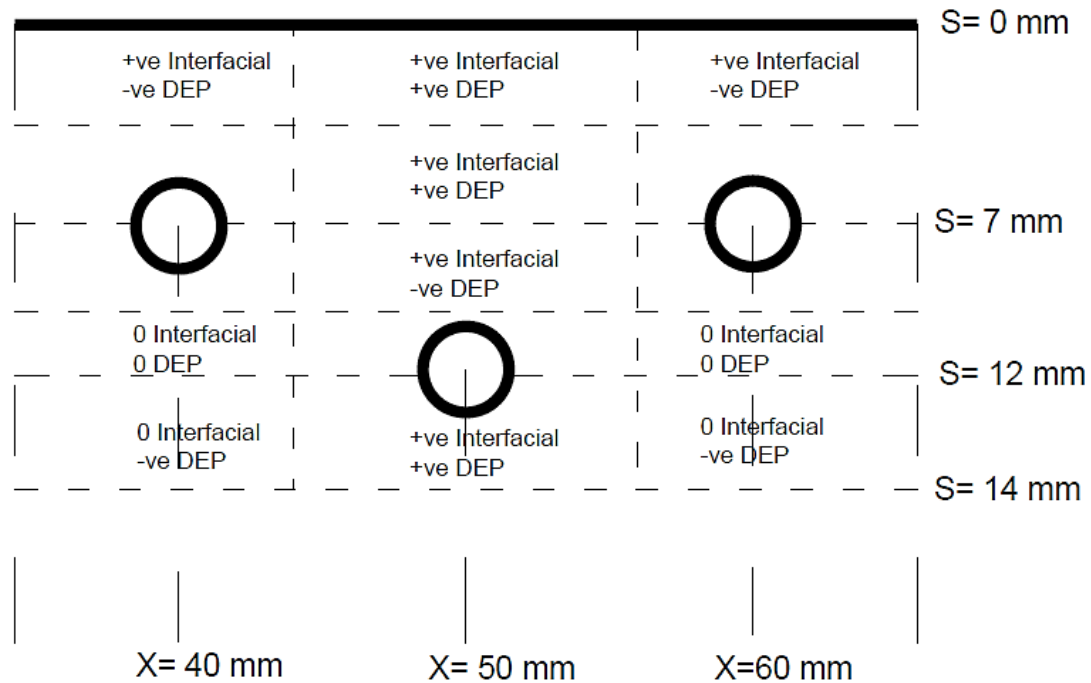


Figure 6.30 Summary for the interfacial and particle attraction forces (DEP) at different melt front locations

6.4.2.3. Summary

From the numerical simulations, it is realized that both the interfacial forces acting on the solid-liquid interface and the DEP forces acting on the suspended extracted dendrite are important in understanding the physics of EHD. This has been supported by the high speed imaging used for visualizing inside the cell. When the melt front is above the upper electrode ($S=0$ to 5.4 mm) the interfacial force (dendrite extraction) decreases as the melt thickness increases which means the amount of dendrites breaking from the mushy zone will tend to decrease. This was supported by the experimental results showing an almost linear decrease in the EHD effect in this range ($S=0$ to $S=7$ mm). The

DEP force is important to understand the contradiction between the numerical evaluation for the interfacial extraction forces and what have been observed in the high speed imaging. Evaluation of the DEP force explained that the regions which is experiencing a positive extraction forces and wasn't observed by high speed imaging, is because this regions are experiencing a negative DEP forces which causes any suspended dendrite to be repelled back to the solid-liquid interface. For melt front location range from $S=10$ mm to 12 mm, it was shown by numerical investigation that this region experiences the lowest extraction forces and that the area which are facing high interfacial attraction forces are in fact experiencing negative DEP which cancels any EHD enhancement effect in this region. That was supported by both the experimental data and the high speed imaging for this region. After the melt front passes the lower electrodes the only active region for extraction and for a positive DEP is beneath the lower electrodes and this explains the increase back of the EHD enhancement. However as the melt front progresses further downwards these values begin to decrease.

7. Conclusions and Recommendations

7.1. Conclusions

Organic materials such as paraffins and fatty acids can be used as a phase change material (PCM) in latent heat thermal storage (LHTS) systems. They are characterized by high latent heat of fusion at relatively low melting temperature ranges which makes them a good candidate in solar and waste heat recovery systems associated with low temperature range thermal applications such as domestic heating. However, they have the disadvantage of low thermal conductivity typically ranging from 0.1 to 0.6 W/m.K. This slows down the heat transfer process and limits the storage capacity for the system over a given charging period.

In this study, the capability of using electrohydrodynamic (EHD) as a heat transfer enhancement technique in LHTS cell was examined. The melting performance of a paraffin wax LHTS cell of melting temperature 63°C was investigated under the application of high voltages to an electrohydrodynamic (EHD) induced flow inside the cell. The cell was designed to maintain a downwards unidirectional melting in order to prevent any natural convection effects from occurring. The purpose was to study the EHD effect with less interfering physics. A constant heat flux boundary condition was

maintained during the experimental period by using a DC electric heater. Electric field was applied inside the cell by using a simple configuration of 9 electrodes of diameter (3.125mm).

Results showed that EHD can be used to enhance the heat transfer process in an originally heat conduction dominated melting process. EHD tests were performed under the application of (-8 kV) inside the cell. It was shown that by using EHD, the melting time for achieving 7 mm melt thickness can be reduced by 40.5 % when compared to 0 kV (no EHD) melting process. Also for a four hour experimental period, the melt thickness achieved can be increased by using EHD in melting by 29 % over the 0 kV case.

EHD is an active heat transfer enhancement technique which requires an additional power to be added to the system in order to achieve a certain enhancement. However, EHD power consumption when compared to other active heat transfer enhancement techniques is relatively low. The EHD power consumption was calculated in this study and it was found to be equal to a maximum of 0.17 W which corresponded to 2.4 % of the heater input power.

A new phenomena was observed due to the application of EHD (non-uniform electric fields), which is Solid Extraction, where the solid dendrites or the equiaxed grains within the mushy zone were pulled from the mushy zone towards the liquid bulk. This phenomena could be one of the important EHD heat transfer enhancement mechanisms in the latent heat thermal storage system tested. The extracted dendrites towards the liquid bulk increase the interfacial area and may have the effect of cooling down regions in the liquid bulk that will lead to induce convection inside the molten PCM. An analogous

phenomena was reported previously by several researchers in liquid-vapour multiphase systems and was called Liquid Extraction.

A criteria of estimating EHD enhancement effects against the 0 kV base cases was developed and used to establish the amount of sensible vs. latent heat stored under EHD enhancement. The melt front velocity at a given melt thickness is taken as this criteria to estimate the EHD effect against the no EHD case. The melt front velocity (dS/dt) is an indication for the storage rate as a latent energy form, which in turn is an indication for the amount of heat transferred from the heating surface to the solid-liquid interface through the molten PCM. The ratio between the melt front velocity at a given thickness for the (-8 kV) case and the 0 kV base case was called the EHD enhancement factor (EF). It was shown that a maximum enhancement factor up to 12.5 can be reached by using EHD for low heater input power (7.1 W) and 6 for higher heater input power (14.2 W). It was found that the EF was not constant over the experimental period but rather there was a range in melt front location level, where EHD showed very low enhancement and sometimes introduced a negative effect on the melt rate. It was found that as the heat flux (power input) increases the EF decreases, this decreasing relationship between the EF and the heat flux magnitude can be due to two different reasons;

The first reason is the thicker mushy zone accompanied with the lower heat flux values, because as the heat flux decreases the melt front velocity decreases giving relatively more time for heat to diffuse in the solid domain leading to a thicker mushy zone. Thicker mushy zones can allow for an easier dendrites extraction.

The second reason is that lower heat fluxes are associated with lower temperatures, which means lower opposing buoyancy force for any induced EHD body forces acting on the liquid bulk.

A two dimensional numerical model was developed to help provide understanding of the physics of EHD enhancement involved in the latent thermal storage system used. The interfacial extraction forces at the solid-liquid interface were evaluated analytically at different melt front locations. In addition, modelling the body forces on an ellipsoid particle suspended in a non-uniform electric field, was performed to understand the trajectory of the extracted dendrites. It was realized that both of the interfacial forces acting on the solid-liquid interface and the DEP forces acting on the suspended extracted dendrite are important in understanding the physics of EHD. The DEP force was important in understanding the contradiction between the numerical evaluation for the interfacial extraction forces and what has been observed in the high speed imaging. Evaluation of the DEP force suggested that the regions which experienced a positive extraction force and was not observed by high speed imaging, is because this regions were experiencing a negative DEP force which causes any suspended dendrite to be repelled back to the solid-liquid interface. For melt front location ranges from $S=10$ mm to 12 mm, it was shown by numerical investigation that this region experiences the lowest extraction forces and that the areas which were facing high interfacial attraction forces were in fact experiencing negative DEP which could cancel the EHD enhancement effect in this region. That was supported by both the experimental data and the high speed imaging for this region.

Overall, it was demonstrated that EHD can be used to enhance the melting rate in a paraffin wax LHTS cell. The power consumption of EHD was very low compared to other active enhancement techniques and equals to 0.1 W.

An analytical full thermal characterization model for the storage cell was developed to estimate the energy stored in each component of the experimental cell. This model was validated by numerical simulations and showed good agreement with the experimental results. The numerical model was used to assess the heat losses from the cell and the maximum heat losses was equal to 18 %.

7.2. Recommendations for future work

- This study showed that EHD can be applied as a heat transfer enhancement technique in a latent heat thermal storage system using paraffin wax as the phase change material. However, this is a new ground for EHD application and will require further studies to facilitate using it in future designs. Recommendations for future work include experimental, numerical and analytical studies to completely understand the physics of EHD enhancement and allow for better future design.
- The electrical properties such as the dielectric constant and the electrical conductivity of different organic PCMs can be evaluated in order to choose the most suitable PCM for each application.
- In this study, the EHD heat transfer enhancement is studied for an originally conduction dominated melting process. Further study is needed to assess the EHD effectiveness in case of a natural convection dominated melting process.

- A real time numerical model needs to be developed to optimize the electrode geometry for future practical implementation in latent heat thermal storage systems.
- EHD effectiveness needs to be studied in other commercially available latent thermal storage configuration systems such as cylindrical shell and tube configuration and spherical capsules configuration.
- In this study, only DC negative polarity is studied and for one voltage only (-8kV). The effect of the polarity and the voltage need to be studied. Also the effect of applying AC voltage and different wave forms need to be studied.
- A study for EHD enhancement for the same configuration in single phase environment will be needed in order to understand the contribution of each EHD body force separately.

Appendix A

Paraffin Wax Thermo-Physical and Electrical Properties

Thermo physical and electrical properties for the paraffin wax used in the experiments are presented in Table C.1. Some properties were given by the wax supplier (IGI-International, Toronto, Ontario, Canada). Other properties were obtained by testing and the rest was obtained from literature

Table A. 1 Thermophysical and electrical properties of paraffin wax

Property	Value	Reference
Density [kg/m ³]	≈ 900	(Agyenim, et al., 2010)
Thermal conductivity [W/m.K]	≈0.2	(Agyenim, et al., 2010)
Specific heat [J/kg.K]	2300	(Agyenim, et al., 2010)
Kinematic viscosity [cSt]	0.42	Supplier
Latent heat of fusion [J/kg]	192000	DSC Test-Appendix B
Melting point [°C]	53-63°C	DSC Test-Appendix B
Dielectric constant	≈ 2.25	(Dellorusso, 1997)
Volumetric expansion coefficient [1/K]	0.00074	(Templin, 1956)

Appendix B

Differential Scanning Calorimetry (DSC) Results

A DSC test was performed by Brockhouse Institute inside McMaster University in order to accurately obtain the melting temperature and the latent heat of fusion for the paraffin wax used in experiments. Results of the DSC are presented in Figure B.1

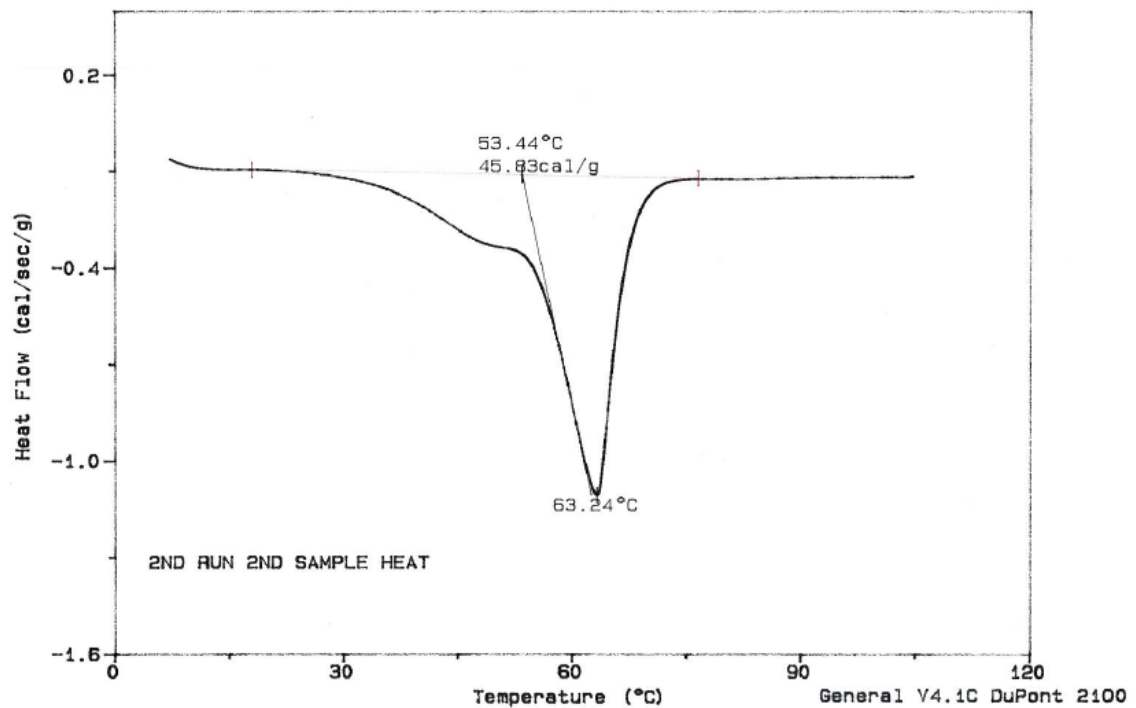


Figure B. 1 DSC test result

Appendix C

Uncertainty Analysis

The uncertainty analysis in this appendix are calculated following the guidelines of Kline and McClintock, 1953.

For any measurement, the overall uncertainty δT associated with a measurement (T) can be determined by

$$\delta T = \sqrt{\sum_{i=1}^n (\delta_i)^2} \quad \text{Equation 3C.1}$$

Where δ_i is the different uncertainties associated with the measurement (T).

This can be further subdivided into a bias error (B) which often quoted by the manufacturer or determined from the calibration and a precision error (P) which is equal to twice the standard deviation for the experimental measurements recorded.

$$\delta_i = \sqrt{(B)^2 + (P)^2} \quad \text{Equation 3C.2}$$

- **Uncertainty in temperature measurements using thermocouples**

Instrument: Type T thermocouples- uncertainty associated δT_{TC}

Bias error:

- Uncertainty of RTD used in calibration $\pm 0.09^\circ\text{C}$
- Uncertainty of TC after calibration with RTD $\pm 0.43^\circ\text{C}$
- Uncertainty of the data acquisition system $\pm 0.02^\circ\text{C}$

Precision error:

The precision error 2 times the maximum standard deviation from the calibrated thermocouples

$$2\sigma = \pm 0.18^\circ\text{C}$$

$$\begin{aligned}\delta T_{TC} &= \sqrt{(0.09)^2 + (0.43)^2 + (0.02)^2 + (0.18)^2} && \text{Equation} \\ &= \pm 0.47^\circ\text{C} && \text{3C.3}\end{aligned}$$

- **Uncertainty in voltage and current measurement for electric heater**

Voltage:

Agilent 6655A DC power supply –digital reading: 0.07 % *reading*

Current:

Agilent 6655A DC power supply –digital reading: 0.35 % *reading*

- **Uncertainty in melt thickness measurement δS**

The uncertainty in melt thickness measurement was identified by taking the maximum error in successful estimating the electrode radius from the images and it was found to be 0.15 mm

$$\delta S = 0.15 \text{ mm}$$

Equation
3C.4

- **Uncertainty in calculated parameters**

The uncertainty for a given parameter that is calculated from a group of measurements can be determined by

$$\delta F = \sqrt{\sum_{i=1}^n \left(\frac{\partial F}{\partial x_i} \delta x_i\right)^2}$$

Equation
3C.5

- **Uncertainty in electric heater power input**

The uncertainty in electric heater power is associated with both the voltage and current measurement, where

$$\begin{aligned} \frac{\delta q}{q} &= \sqrt{\left(\frac{\delta V}{V}\right)^2 + \left(\frac{\delta I}{I}\right)^2} \\ &= \sqrt{(0.07)^2 + (0.35)^2} = 0.36 \% \end{aligned}$$

Equation
3C.6

BIBLIOGRAPHY

- Abhat, A. (1983). LOW TEMPERATURE LATENT HEAT THERMAL ENERGY STORAGE . *HEAT STORAGE*, 10(4), 313–332.
- Agyenim, F., Hewitt, N., Eames, P., & Smyth, M. (2010). A review of materials, heat transfer and phase change problem formulation for latent heat thermal energy storage systems (LHTESS). *Renewable and Sustainable Energy Reviews*, 14(2), 615–628. doi:10.1016/j.rser.2009.10.015
- Akhilesh, R., Narasimhan, A., & Balaji, C. (2005). Method to improve geometry for heat transfer enhancement in PCM composite heat sinks. *International Journal of Heat and Mass Transfer* 48.13 , 2759-2770.
- Allen, P. H., & Karayiannis, T. G. (1995). Electrohydrodynamic enhancement of heat transfer and fluid flow. *Heat Recovery Systems and CHP* 15, no. 5 , 389-423.
- Avsec, D., & Luntz, M. (1937). Electricite et Hydrodynamique. *Compt. Rend* 204 .
- Berber, S., Kwon, Y., & Tomanek, D. (2000). Unusually high thermal conductivity of carbon nanotubes. *Physical review letters*, 84(20), 4613–6.
- Bergles, A. E. (2011). Recent developments in enhanced heat transfer. *Heat and mass transfer* 47, no. 8 , 1001-1008.
- Bryan, J. E., & Seyed-Yagoobi, J. (2001). Influence of Flow Regime, Heat Flux, and Mass Flux on Electrohydrodynamically Enhanced Convective Boiling. *Journal of Heat Transfer*, 123(2).
- Castellon, C., Nogues, M., Roca, J., & Cabeza, L. (2005). Design of a plastic encapsulation for phase change materials (PCM) in buildings. *IEA ECES IA Annex 17.* " In 8th workshop, (pp. 18-20).
- Chang, J.-S., & Watson, A. (1994). Electromagnetic hydrodynamics. *Dielectrics and Electrical Insulation, IEEE Transactions on* 1, no. 5 , 871-895.
- Cheung, K., Ohadi, M. M., & Dessiatoun, S. V. (1999). EHD-assisted external condensation of R-134a on smooth horizontal and vertical tubes. *International journal of heat and mass transfer* 42, no. 10 , 1747-1755.
- Chu, B.-T. (1959). Thermodynamics of Electrically Conducting Fluids. *Physics of Fluids*, 2(5). doi:10.1063/1.1705937
- Colaço, M. J., Dulikravich, G. S., & Martin, T. J. (2004). Optimization of Wall Electrodes for Electro-Hydrodynamic Control of Natural Convection during Solidification. *Materials and Manufacturing Processes*, 19(4), 719–736.

- Cotton, J. (2000). *Mechanisms of Electrohydrodynamic flow and heat transfer in*. PhD Thesis.
- Cotton, J., Robinson, A., Shoukri, M., & Chang, J. (2005). A two-phase flow pattern map for annular channels under a DC applied voltage and the application to electrohydrodynamic convective boiling analysis. *Int. Journal of Heat and Mass Transfer*, 48(25-26), 5563-5579.
- Dellorusso, P. R. (1997). *Electrohydrodynamic Heat Transfer Enhancement for a Latent Heat Storage Heat Exchanger*. Technical University of Nova Scotia, 1997.
- Dionne, G. F., Fitzgerald, J. F., & Aucoin, R. C. (1976). Dielectric constants of paraffin-wax-TiO mixtures.
- Dulikravich, S., G., Ahuja, V., & Lee, S. (1994). Modeling of dielectric fluid solidification with charged particles in electric fields and reduced gravity. *Numerical Heat Transfer, Part B Fundamentals* 25, no. 3 , 357-373.
- Felderhoff, M., Urbanczyk, R., & Peil, S. (2013). Thermochemical Heat Storage for High Temperature Applications—A Review. *Green* 3, no. 2, 113-123.
- Felix Regin, A., Solanki, S. C., & Saini, J. S. (2005). Thermal performance analysis of phase change material capsules. *Solar World Congress 2005: Bringing Water to the World, Including 34th ASES Annual Conference and 30th National Passive Solar Conference*, (pp. 1821-1826).
- Fernández, J., & Poulter, R. (1987). Radial mass flow in electrohydrodynamically-enhanced forced heat transfer in tubes. *International journal of heat and mass transfer* 30, no. 10 , 2125-2136.
- Fujino, T., Yokoyama, Y., & Mori, Y. H. (1989). Augmentation of Laminar Forced-Convective Heat Transfer by the Application of a Transverse Electric Field. *Journal of Heat Transfer*, 111, 345–351.
- Gascoyne, P. R., & Vykoukal, J. (2002). Particle separation by dielectrophoresis. 23(13).
- Gharebaghi, M., & Sezai, I. (2007). Enhancement of Heat Transfer in Latent Heat Storage Modules with Internal Fins. *Numerical Heat Transfer, Part A: Applications*, 53(7), 749–765.
- Gidwani, A., Molki, M., & Ohadi, M. M. (2002). EHD-enhanced condensation of alternative refrigerants in smooth and corrugated tubes. *HVAC&R Research* 8, no. 3 , 219-237.
- Haillot, D., Py, X., Goetz, V., & Benabdelkarim, M. (2008). Storage composites for the optimisation of solar water heating systems. *Chemical Engineering Research and Design*, 86(6), 612-617.
- Henze, R. H., & Humphrey, J. A. (1981). Enhanced heat conduction in phase-change thermal energy storage devices. *International journal of heat and mass transfer* 24, no. 3 , 459-474.
- Jegadheeswaran, S., & Pohekar, S. D. (2009). Performance enhancement in latent heat thermal storage system: A review. *Renewable and Sustainable Energy Reviews*, 13(9), 2225–2244. doi:10.1016/j.rser.2009.06.024
- Jones, T. B. (2005). *Electromechanics of particles*. Cambridge University Press.

- Kasayapanand, N. (2008). Electrohydrodynamic enhancement of heat transfer in vertical fin array using computational fluid dynamics technique . *International Communications in Heat and Mass Transfer*, 35, 762–770.
- Kenisarin, M., & Mahkamov, K. (2007). Solar energy storage using phase change materials. *Renewable and Sustainable Energy Reviews*, 11(9), 1913–1965.
- Kim, S., & Drzal, L. T. (2009). High latent heat storage and high thermal conductive phase change materials using exfoliated graphite nanoplatelets. *Solar Energy Materials and Solar Cells*, 93(1), 136–142.
- Kline, S. J., & McClintock, F. A. (1953). Describing uncertainties in single-sample experiments. *Mechanical engineering*, 3-8.
- Lacroix, M., & Benmadda, M. (1997). Numerical Simulation of Natural Convection-Dominated Melting and Solidification From a Finned Vertical Wall. *Numerical Heat Transfer, Part A: Applications*, 31(1), 71-86.
- Lacroix, M., & Benmadda, M. (1998). Analysis of natural convection melting from a heated wall with vertically oriented fins. *International Journal of Numerical Methods for Heat & Fluid Flow*, 8(4), 465–478.
- Lamberg, P., Lehtiniemi, R., & Henell, A.-M. (2004). Numerical and experimental investigation of melting and freezing processes in phase change material storage. *International Journal of Thermal Sciences*, 43(3), 277–287.
- Lund, H., & Andersen, A. N. (2005). Optimal designs of small CHP plants in a market with fluctuating electricity prices. *Energy Conversion and Management* 46, no. 6 , 893-904.
- Mazman, M., Cabeza, L. F., Mehling, H., Paksoy, H. Ö., & Evliya, H. (2008). Heat transfer enhancement of fatty acids when used as PCMs in thermal energy storage. *International Journal of Energy Research* 32, no. 2, 135-143.
- McAdams, W. (1954). *Heat Transmission*, 3rd Ed. New York, NY: McGraw-Hill.
- Mehling, H., & Cabeza, L. F. (2008). *Heat and Cold Storage with PCM: An Up to Date Introduction Into Basics and Applications*. Springer.
- Melcher, J. R. (1963). *Field-coupled surface waves: a comparative study of surface-coupled electrohydrodynamic and magnetohydrodynamic systems*. Cambridge, Mass.: M.I.T. Press.
- Mesalhy, O., Lafdi, K., Elgafy, A., & Bowman, K. (2005). Numerical study for enhancing the thermal conductivity of phase change material (PCM) storage using high thermal conductivity porous matrix. *Energy Conversion and Management*, 46(6), 847-867.
- Mettawee, E.-B. S., & Assassa, G. M. (2007). Thermal conductivity enhancement in a latent heat storage system. *Solar Energy*, 81(7), 839–845.
- Nakaso, K., Teshima, H., Yoshimura, A., Nogami, S., Hamada, Y., & Fukai, J. (2008). Extension of heat transfer area using carbon fiber cloths in latent heat thermal energy storage tanks. *Chemical Engineering and Processing: Process Intensification*, 47(5), 879–885.
- Nangle Smith, S. (2012). *The Effect of High Voltage Electric Fields on Two Phase Flow Pattern Redistribution & Heat Exchanger Performance*. Hamilton, Ontario: McMaster University.

- Nayak, K. C., Saha, S. K., Srinivasan, K., & Dutta., P. (2006). A numerical model for heat sinks with phase change materials and thermal conductivity enhancers. *International Journal of Heat and Mass Transfer* 49, no. 11 , 1833-1844.
- Ng, K., Ching, C. Y., & Cotton., J. S. (2011). Transient Two-Phase Flow Patterns by Application of a High Voltage Pulse Width Modulated Signal and the Effect on Condensation Heat Transfer. *Journal of heat transfer* 133, no. 9 .
- Norris, C. E., Cotton, J. S., Shoukri, M., Chang, J.-S., & Smith-Pollard, T. (1999). TECHNICAL PAPERS-4248-Electrohydrodynamic Effects on Flow Redistribution and Convective Boiling in Horizontal Concentric Tubes Under High Inlet Quality Conditions. *ASHRAE Transactions-American Society of Heating Refrigerating Airconditioning Engin* 105, no. 1 , 222-236.
- Oh, Y. K., Park, S. H., & Cho., Y. I. (2002). A study of the effect of ultrasonic vibrations on phase-change heat transfer. *International journal of heat and mass transfer* 45, no. 23 , 4631-4641.
- Paschkewitz, J. S., & Pratt, D. M. (2000). The influence of fluid properties on electrohydrodynamic heat transfer enhancement in liquids under viscous and electrically dominated flow conditions. *Experimental Thermal and Fluid Science*,21, 187–197.
- Pohl, H. A. (1951). The motion and precipitation of suspensoids in divergent electric fields. 22(7).
- Pohl, H. A. (1960). Nonuniform field effects in poorly conducting media. 107(5).
- Pohl, H. A., & Crane, J. S. (1972). Dielectrophoretic force. 37(1).
- Py, X., Olives, R., & Mauran, S. (2001). Paraffin/porous-graphite-matrix composite as a high and constant power thermal storage material. *International Journal of heat and mass transfer* 44, no. 14 , 2727-2737.
- Reddy, K. S. (2007). Thermal modeling of PCM-based solar integrated collector storage water heating system. *Journal of solar energy engineering* , 129(4) , 458-464.
- Sadek, H. (2009). *Electrohydrodynamic control of convective condensation heat transfer and pressure drop in a horizontal annular channel*. Hamilton,Ontario: McMaster University.
- Sadek, H., Ching, C. Y., Cotton., J., & d. (2010). The effect of pulsed electric fields on horizontal tube side convective condensation. *International Journal of Heat and Mass Transfer* 53, no. 19, 3721-3732.
- Salehi, M., Ohadi, M., & Dessiatoun, S. (1997). EHD Enhanced Convective Boiling of R134a in Grooved Channels - Application to Subcompact Heat Exchangers. *Journal of Heat Transfer*,, 805-809.
- Sanusi, O., Warzoha, R., & Fleischer, A. S. (2011). Energy storage and solidification of paraffin phase change material embedded with graphite nanofibers. *International Journal of Heat and Mass Transfer*, 54(19-20), 4429–4436. doi:10.1016/j.ijheatmasstransfer.2011.04.046
- Sari, A., & Karaipekli, A. (2007). Thermal conductivity and latent heat thermal energy storage characteristics of paraffin/expanded graphite composite as phase change material. *Applied Thermal Engineering*, 27(8-9), 1271-1277.

- Saville, D. A., & Palusinski, O. A. (1986). Theory of electrophoretic separations. part i: Formulation of a mathematical model. *AIChE Journal* 32, no. 2 , 207-214.
- Scaife, B. K. (1989). *Principles of dielectrics*.
- Sharma, A., Tyagi, V. V., Chen, C. R., & Buddhi, D. (2009). Review on thermal energy storage with phase change materials and applications. *Renewable and Sustainable Energy Reviews*, 13(2), 318–345.
- Shatikian, V., Ziskind, G., Letan, R., & d. (2005). Numerical investigation of a PCM-based heat sink with internal fins. *International Journal of Heat and Mass Transfer*, 48(17), 3689–3706.
- Singh, A. O. (1995). Electrohydrodynamic (EHD) enhancement of in-tube condensation heat transfer of alternative refrigerants R-134a in smooth and microfin tubes. *ASHARE Trans*, 103(1), 813-823.
- Singh, A., Dessiatoun, S., Ohadi, M. M., & Chu, W. (1994). In-tube boiling heat transfer enhancement of R-123 using the EHD technique. *100(2)*, 818-825.
- Stark, P. (1990). PCM-impregnated polymer microcomposites for thermal energy storage. *In SAE, 20th Intersociety Conference on Environmental Systems, vol. 1*.
- Stratton, J. A. (1941). *Electromagnetic theory*. McGraw-Hill Book Co. New york, 508.
- Stritih, U. (2004). An experimental study of enhanced heat transfer in rectangular PCM thermal storage. *International Journal of Heat and Mass Transfer*, 47(12-13), 2841–2847. doi:10.1016/j.ijheatmasstransfer.2004.02.001
- Tian, Y., & Zhao, C.-Y. (2009). Heat transfer analysis for phase change materials (PCMs). *Effstock Conference ,no.28*. Richard Stockton College of New Jersey.
- Tian, Y., & Zhao, C.-Y. (2011). A numerical investigation of heat transfer in phase change materials (PCMs) embedded in porous metals. *Energy* 36, no. 9, 5539-5546.
- Veilleux, D. L., Faghri, M., Asako, Y., & Charmchi, M. (2007). Convection Enhancement in Melting by Electromagnetic Fields in a Low-Gravity Environment: Side Wall Heating. *51(2)*, 129-158.
- Veilleux, D. L., Faghri, M., Asako, Y., & Charmchi, M. (2007). Convection Enhancement in Melting by Electromagnetic Fields in a Low-Gravity Environment: Side Wall Heating. *Numerical Heat Transfer, Part A: Applications*, 51(2), 129-158.
- Velraj, R., Seeniraj, R. V., Hafner, B., Faber, C., & Schwarzer, K. (1999). Heat Transfer Enhancement in a Latent Heat Storage System. *Solar Energy*, 65(3), 171–180.
- Vliet, G. C. (1969). Natural convection local heat transfer on constant-heat-flux inclined surfaces. *ASME J. Heat Transfer*, Vol. 91, 511-516.
- Webb, L., R., & Kim, N.-H. (1994). *Principles of Enhanced Heat Transfer*.
- Yabe, A. M. (1987a). Heat transfer enhancement techniques utilizing. *Heat Transfer in High Technology and Power Engineering.*, 394-405.
- Yabe, A. T., Taketani, T., Maki, H., Takahashi, K., & Nakadai, Y. (1992). Experimental study of electrohydrodynamically(EHD) enhanced evaporator for nonazeotropic mixtures. *In ASHRAE Winter Meeting, Anaheim, CA, USA*, 455-460.

- Zalba, B., Marín, J. M., Cabeza, L. F., & Mehling, H. (2003). Review on thermal energy storage with phase change: materials, heat transfer analysis and applications. *Applied Thermal Engineering* (23), 251–283.
- Zhang, Y., & Faghri, A. (1996). Heat Transfer Enhancement in Latent Heat Thermal Energy Storage System by Using an External Radial Finned Tube. *Journal of enhanced Heat Transfer*, 3(2), 119–127.
- Zhang, Y., & Faghri, a. (1996). Heat transfer enhancement in latent heat thermal energy storage system by using the internally finned tube. *International Journal of Heat and Mass Transfer*, 39(15), 3165–3173.
- Zhao, Chang-Ying, Lu, W., & Tian, Y. (2010). Heat transfer enhancement for thermal energy storage using metal foams embedded within phase change materials (PCMs). *Solar Energy* 84, no. 8 , 1402-1412.
- Zhou, D., & Zhao, C.-Y. (2011). Experimental investigations on heat transfer in phase change materials (PCMs) embedded in porous materials. *Applied Thermal Engineering* 31, no. 5 , 970-977.